AN INVESTIGATION IN STRUCTURAL SHAPE MORPHING BY MODULUS VARIATION

by

Seyed Amin Mohaghegh Motlagh

B.S. in Mechanical Engineering, Isfahan University of Technology, Iran, 2003

M.S. in Mechanical Engineering, University of Toledo, OH, 2008

Submitted to the Graduate Faculty of

the Swanson School of Engineering in partial fulfillment

of the requirements for the degree of

Doctor of Philosophy in Mechanical Engineering

University of Pittsburgh

2013

UNIVERSITY OF PITTSBURGH

SWANSON SCHOOL OF ENGINEERING

This dissertation was presented

by

Seyed Amin Mohaghegh Motlagh

It was defended on

October 31, 2013

and approved by

Daniel G. Cole, Ph.D., Associate Professor
Department of Mechanical Engineering and Materials Science

Jeffrey S. Vipperman, Ph.D., Associate Professor
Department of Mechanical Engineering and Materials Science

John C. Brigham, Ph.D., Assistant Professor
Department of Civil and Environmental Engineering

Dissertation Director: William W. Clark, Ph.D., Professor
Department of Mechanical Engineering and Materials Science

AN INVESTIGATION IN STRUCTURAL SHAPE MORPHING BY MODULUS VARIATION

Seyed Amin Mohaghegh Motlagh, Ph.D.

University of Pittsburgh, 2013

This work addresses structural shape morphing, defined as change of shape due to modulus manipulation. The goal is to incorporate variable-modulus materials into a structure, and utilize the controllable modulus change to enhance the ability to morph the structure with *limited* actuator numbers, locations, and force levels to desired shapes that could not be achieved in the native structure. A significant portion of the work is to demonstrate the capability of the proposed strategy to broaden the space of achievable shapes within the elastic range. In order to quantify the morphed shapes, a specific planar structure with defined boundary condition is used as the model. The focus of this study is not the temporal change of the material's phase or the structure's shape, but rather the resulting shape of the structure due to modulus change and applied force.

The problem of *inverse morphing* is thoroughly investigated; that is, finding the spatial distribution of elastic modulus values and the actuation forces that produce a desired shape and minimize the shape error cost function. Genetic algorithm is used to solve this inverse problem.

Finally, a numerical algorithm to solve the morphing of an arbitrary structure is proposed. In this algorithm, computational and numerical programs are interchangeably used to build the structure's model and to solve the shape morphing problem. As a case study, a practical device is selected, drawn from a hydrokinetic energy harvesting application, and a 2D model is created.

The structure's shape change due to modulus manipulation is numerically investigated. At the end, path-dependency in sequential shape morphing has been explored in a mass-spring model as well as in the example structure.

TABLE OF CONTENTS

LIST OF TABLES

LIST OF FIGURES

ACKNOWLEDEGMENT

In the completion of this work, I am obliged to many kind people. My sincere gratitude to my dissertation advisor, Dr. William (Buddy) Clark for his support and guidance throughout all the stages of this work. His time and consideration is greatly appreciated. Also, I am grateful to my committee for their time and constructive recommendations on this work. I am truly thankful for Dr. John Brigham and his Ph.D. student, Shuang Wang for their help on Abaqus. Many thanks to Dr. Dan Cole for his insights on hydrokinetic device performance.

I would like to recognize our lab members, Minmin Zeng , Mike Whiston and Danielle Miller Bond. I will always remember our friendship with its good memories.

Last, but not the least, I express my gratitude to my parents whom I have much missed and to my lovely wife, Flora, who passionately supported me in this journey. Her patience and companionship in every single moment was so motivating to me.

1.0 INTRODUCTION

Among numerous engineering and scientific applications, there are conditions where a structure is required to deform from its defined shape to another shape in order to accommodate new geometry or stress requirements. For example, in the biomedical field, coronary stents are inserted into a narrow vascular passage and then expanded to prevent localized flow constriction (Cwikiel et al., 1993). This change of shape is often intended as a means to expand the performance capabilities of the system.

The concept of *shape change* generally implies transforming the spatial orientation of a structure from its natural shape to one or several desired shapes. Based on our comprehensive review, we divided the previous works on structural shape change into two major categories which are shown in Figure 1-1: 1) conventional methods (also referred to as *shape control*) in which the desired shape is obtained either from elastic or plastic deformation of the structure using actuating forces, or by moving rigid body linkages using underlying mechanisms; and 2) *shape morphing* which uses forces *and* modulus change. This work falls into the latter category. Beneath shape morphing, one could categorize a subset for the "shape memory effect", where the structure, formed by a memory material morphs to another memorized shape upon a stimulus. However, the memory effect is distinct from this work in that one cannot independently change modulus without imparting inherent forces. In other words, in memory materials, dimension, modulus and force changes are interrelated by the constitutive equations. In this

study, no particular material is considered; rather it is assumed that variation of the modulus is correlated with a stimulus while independent of force or geometry.

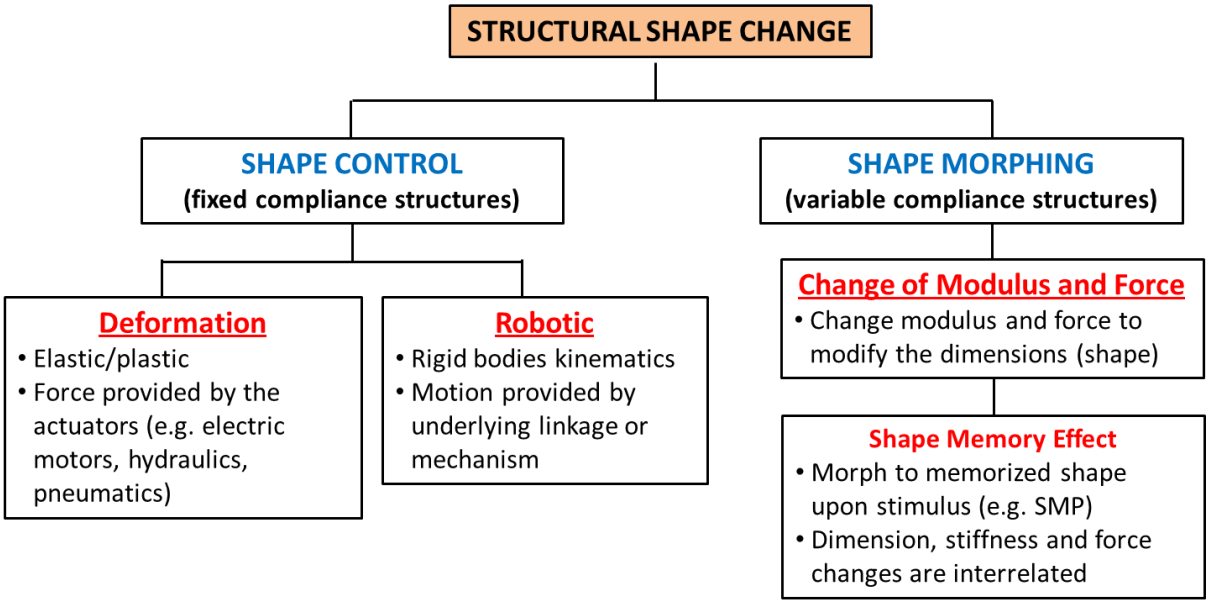

Figure 1-1: Different categories of the existing and current work on structural shape change

In the first part of this chapter, a thorough literature review of the existing works on different shape change methods and their advantages and shortcomings is presented. Application of common shape memory materials is explored. This work specifically falls into the "shape morphing" section which uses force plus modulus change. Later, significance of this work is clearly highlighted and distinguished from the current literature.

1.1 A REVIEW ON SHAPE CONTROL METHODS

1.1.1 Conventional mechanisms

Traditional *shape control* methods have long been applied to a diverse range of structural materials, such as plastics, ceramics, metals, polymers and composites whose mechanical properties are *constant*. Numerous works have been performed on wings that undergo large changes in geometry. Neal (Neal, 2006) proposed a wing with changing area such that its configuration is optimized for a wide range of changing flight conditions (e.g. loiter, dash and high-speed maneuverability).

Figure 1-2: Changing the wing to three configurations (from left: loiter, dash and asymmetric maneuvering) (Neal, 2006)

Reed (Reed et al., 2005) developed a wing structure with capability of change in chord and wing's planform area, resulting in optimizing flight efficiency. Another group (Flangan et al., 2007) worked on the development of Morphing Flight-vehicle Experimental (MFX-1), with a shape-changing wing, in an effort to demonstrate in-flight shape change.

Others used telescopic (Blondeau et al., 2003) and inflatable wings (Jacob et al., 2005) for shape control. Figure 1-3 shows an inflatable wing concept. The authors characterized the wing deformation and developed a numerical model to predict the deformation.

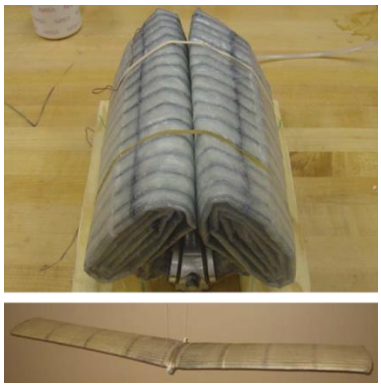

Figure 1-3: Non-inflated wing (top) and inflated wings (bottom) (Jacob et al., 2005)

Shape control has also been integrated in the realm of automotive industries. Design of a vehicle system involves satisfying competing objectives for various attributes, such as noise, vibration and harshness (NVH), durability, safety, vehicle dynamics, and ergonomic comfort. To achieve the optimal design, dedicated CAE tools have been used to evaluate the functional performance and quantify trade-offs in design variants which can be effectively altered with shape change methods (Brughmans et al., 2003).

1.1.2 Adaptive materials as fixed actuators

Actuation can be executed by mechanical linkage or by adaptive materials which actively respond (force or displacement) to an external stimulation as demanded. When integrated as actuators into a fixed-compliance structure, these materials can enhance the flexibility or performance of the system.

Shape Memory Alloys (SMAs)

SMA is lightweight and has large force and displacement capabilities as well as low power consumption which makes it a suitable actuator for bending control (Falcioni, 1992). SMA has

been used for changing the shape of chevrons on the trailing edge of a jet engine in order to optimize the acoustics and performance (Calkins et al., 2006). Following this work, the proposed SMA actuator system was developed by integrating the Variable Geometry Chevrons (VGC) into the thrust reverser and performing the analysis and testing that was required to gain approval (Mabe et al., 2007). Another work (Chaudhry and Rogers, 1991) investigated shape control of beams in bending with induced SMA strain actuators. In their first configuration (Figure 1-4a), the outside actuator provides enhanced bending due to the buckling actuation load. The beam displacement is much greater than that of the embedded or surface bonded actuators. In the second design (Figure 1-4b), the actuator's offset distance causes an increased tip moment with a minimal increase in the flexural stiffness.

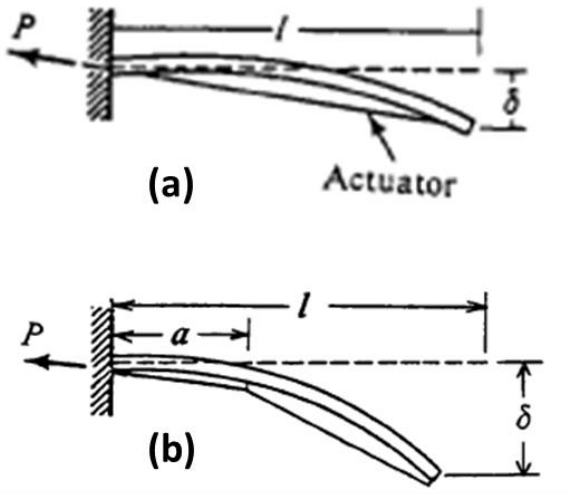

Figure 1-4: Bending control of a beam using SMA actuators (Chaudhry and Rogers, 1991)

Moreover, the two-way shape memory effect in a laminated composite plate and beam has been investigated (Cho and Kim, 2005). The structure returned to its initial shape by increasing or decreasing temperature under an initially given residual stress.

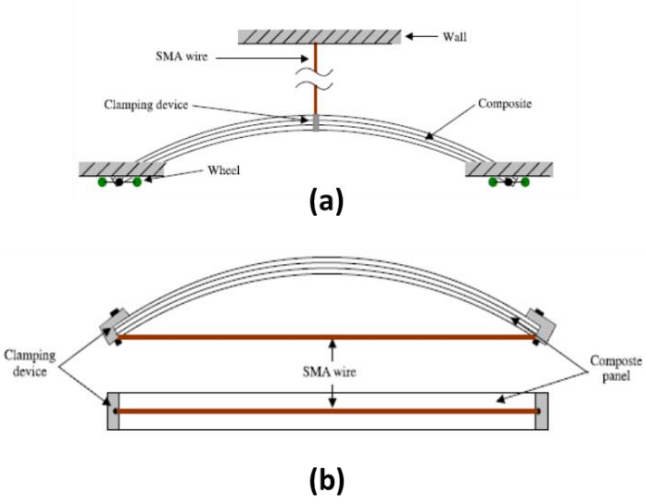

Figure 1-5: Schematic of actuator device for morphing of a laminated beam (Cho and Kim, 2005)

Piezoelectric actuators (PZTs)

The piezoelectric effect is the linear electromechanical interaction between the mechanical and the electrical state in crystalline materials (Gautschi, 2002). The piezoelectric effect is a reversible process which makes these materials good candidate for shape control.

Many works have been accomplished on shape control of structures using piezoelectric materials. (Donthireddy and Chandrashekhara, 1996) developed a model for laminated composite beams with piezoelectric actuators. (Chandrashekhara and Varadarajan, 1997) also studied the adaptive shape control of laminated composite beams with integrated piezoelectric actuators. An optimization algorithm was implemented to calculate the optimal open loop actuator voltages which minimize the error function. A closed loop feedback system was developed to maintain the desired shape even in the presence of varying unknown loads. (Ameri et al., 2008) developed a small-scale flying wing with active winglets via a distribution of piezo or thermo strain actuators.

The shape (spatial distribution) of the piezo-actuated structure remains fixed in its lifetime. If a dynamic shape control is intended, using multiple independent layers or patches within the structure can achieve a variation of the shape of piezoelectric actuation (Gautschi, 2002). Some of the suggested shape control strategies using piezoelectric actuation have found practical applications in industry, such as aerospace, precision engineering and mechatronics. However, low efficiency of the piezoelectric ceramics is still a major drawback for large-scale utilization. Lazarus et al. (1991) showed that for a given application shape memory alloy actuators, due to their large actuation strain capability and high elastic modulus, outperformed piezoceramic actuators for static shape control.

1.1.3 Optimal actuator placement

All of the reviewed works accomplished a change in a structure's shape by continuously varying the magnitude of actuation forces over the spatial domain to finally transfer the system to the required geometry. Another strategy to change the shape in fixed-compliance structures is by finding the optimal actuators' locations. Considerable works have been done on optimizing the actuators' placement, most of which focused on large flexible space structures and with the aim of static deformation correction in order to maintain the exact shape of the structure. (Haftka and Adelman, 1985) investigated the selection of actuator locations for static shape control of large space structures by heuristic integer programing. In another work by Haftka (1984), optimum placement of controls for static deformations of space antennas was studied. (Furuya and Haftka, 1995) developed a procedure to estimate the effectiveness of the actuators in various locations and discard ineffective ones. His method could reduce the cost of the optimization. (Agrawal and Treanor, 1999) investigated the optimum piezoceramic actuator locations (and

voltage) to minimize the error between the desired and achieved shape of a beam based on an Euler-Bernoulli model (Figure 1-6). The authors have presented analytical and experimental results on optimal placement of PZT actuators for shape control within a linear region of piezeceramic behavior.

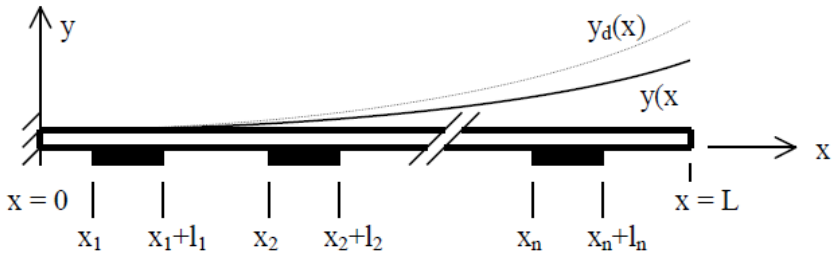

Figure 1-6: Cantilever beam with attached piezeceramic actuators (Agrawal and Treanor, 1999)

In all of these applications, a common thread is that the underlying structural material has fixed mechanical properties and the actuator is the sole contributor to the shape change. Due to fixed material properties, the expected controlled shapes are significantly limited to the actuators' force and location as well as the material's range of stability.

1.2 A REVIEW ON SHAPE MORPHING METHODS

An alternative new way of shape control, which is the core of this work, is applicable to the structure that is fully or partially made up of a variable stiffness material and can be locally or fully softened to accommodate the desired shape change. This implies, with fixed actuator positions, one could manipulate the force magnitudes as well as the structural stiffness in local regions to accommodate the desired shape change. This change of shape due to modulus manipulation is referred to as *shape morphing*.

Memory materials may be used as the forming material of the structure. In this case, shape morphing may either be due to exertion of an external driving force/moment and meanwhile exciting the structure to change its mechanical properties or, for a particular class of memory materials, deform it into a memorized fixed shape once excited with external stimulus. The desired shape in the latter case is programmed into the material's memory once it is heated above certain transition temperature. Some of the most common smart materials in morphing applications have been explored in the following.

Shape Memory Polymers (SMPs): SMPs are a class of intelligent materials that have the ability to change from a fixed, temporary shape to a pre-determined permanent shape upon the application of stimuli such as heat or light irradiation (Otsuka and Wayman, 1999; Monkman, 2000; Lendlein and Kelch, 2002). SMPs have been utilized as a suitable structural material for morphing applications. Because of the relatively low modulus of SMP compared to SMAs, in some applications its modulus change is a more dominant effect than its shape recovery property, particularly when external forces are larger than the recovery forces that can be generated in the material. In such scenarios, it can be beneficial to use the material for its modulus change and to ignore its inherent, but small, shape recovery. Moreover, large elastic stiffness change (from several GPa to several tens of MPa) makes SMP a viable option for variable stiffness material (McKnight and Henry, 2005).

Previous works have addressed shape change by modulus variation; however much of their focus has been on morphing skin technology on aircrafts. For example, (Keihl et al., 2005) investigated shape memory polymer (SMP) as a skin material for aircraft morphing applications. Experiments suggested that multiple state abilities of SMP facilitate a shape change and resist large loads as they are cooled. (Perkins et al., April 2004) fabricated a chord morphing wing

using various advanced technologies such as SMP, dynamic modulus composites (DMC) and dynamic modulus foams (DMF). (Pastor et al., 2006) employed topology optimization to tailor the distribution of material properties of a morphing skin to minimize out-of-plane displacement. Rauscher and Clark (Rauscher, 2008a) designed and fabricated a fiber-reinforced composite SMP skin tile for a wing (Figure 1-7). As the wing spreads, each single tile experiences a change in surface area, resulting in a total morph of 45° shear angle that conventional passive material could hardly handle.

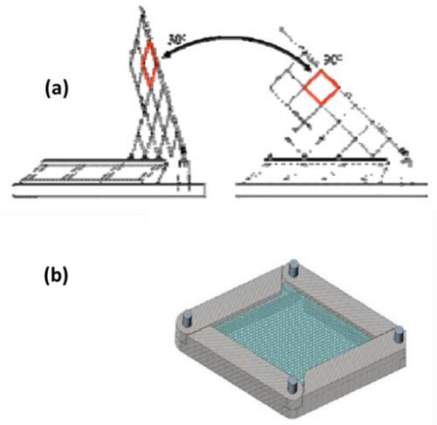

Figure 1-7: Shape change of a morphing wing with interlocking tiles.
A single tile with SMP skin and wire fibers is also shown (Rauscher, 2008b)

There is some precedent for exploiting the hard-soft-hard transition of SMP. Boyerinas and Clark (2009) developed a locking "smart" link mechanism for a folding wing by embedding SMA and SMP (Figure 1-8). The designated morphing wing consists of folding ribs and is covered with a foldable skin. Each rib can be folded into the fuselage to effectively decrease the wing surface area. The wing motion is caused by external electromagnetic actuators. The SMP layer served as the unlocking mechanism, whereas the SMA acted as an elastic support layer to provide structural integrity.

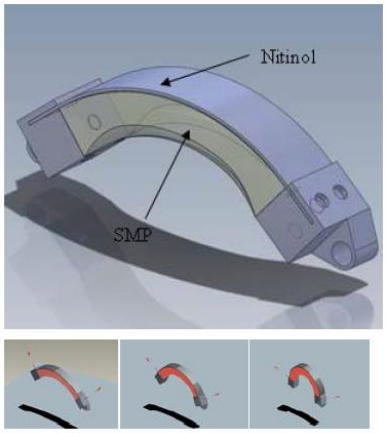

Figure 1-8: Schematic of composite locking link
(top) and sequence of link configurations in a morphing application (bottom) (Boyerinas et al., 2009)

Morphing techniques have also been implemented in biomedical field. In an expandable child's bone implant (Figure 1-6) titanium is wrapped in a memory polymer. Electromagnetic field is used to stretch the implant in situ as the body grows.

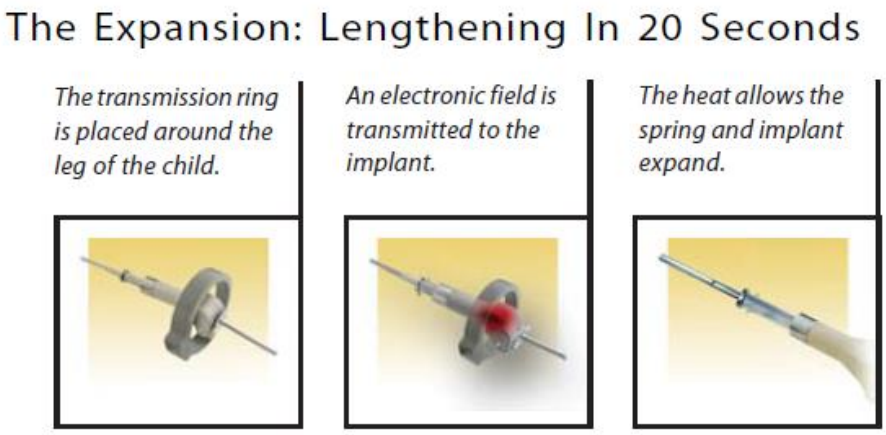

Figure 1-9: Expandable bone implant
(Wright Medical Technology, Inc.)

SMAs and Piezoceramics: due to their larger actuation force compared to shape recovery strains (Otsuka and Wayman, 1999; Lendlein and Kelch, 2002), SMAs have been mostly utilized as actuators (rather than forming material) in shape control applications. However, SMA is also utilized for medical coronary stents (Morgan, 2004; Vinograd et al., 1994), which undergo a one-

time shape morphing after insertion into blocked arteries (Figure 1-10). Recently, a new material known as meta-magnetic shape memory alloy (MMSMA) foam has been developed as a potential morphing tissue scaffold for biomedical applications (Monroe et al., 2012).

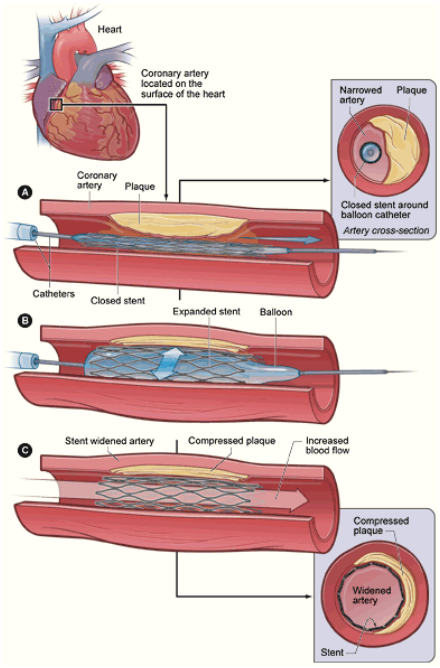

Figure 1-10: SMA stent shape change to accommodate the required condition (Morgan, 2004)

Likewise, in most of the previous works, the piezo materials were used as actuators to cause the shape change. There are some applications where piezo is used for stiffness control by switching between their open- and closed-circuit states (Corr and Clark, 2002; Clark, 2000); however because of its high stiffness the shape changes are extremely small in these examples.

Electroplastic hydrogels: While conventional intelligent materials are to date very advantageous for morphing applications, they still demonstrate some shortcomings, some of which were previously discussed. New materials are emerging to overcome the drawbacks of the current materials and meet more morphing requirements. One of the most state-of-the-art smart

materials are the Electroplastic elastomer hydrogels (EPEHs) that can reversibly switch between hard and soft states with the application of an electrical potential (Calvo-Marzal et al., 2011).

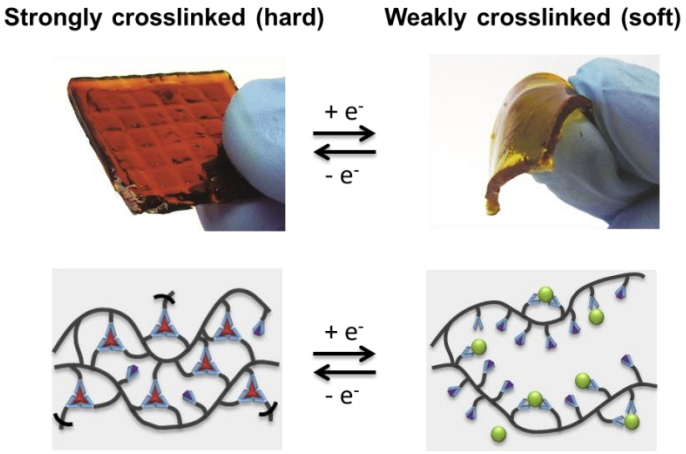

Figure 1-11: Switching between hard and soft states for iron-based electroplastic elastomer. Reversible electrochemical conversion of stiff (oxidized) Fe3+-crosslinked hydrogel (left) to softer (reduced) Fe2+ hydrogel (right) (Calvo-Marzal et al., 2011)

Reduction-Oxidaztion (Redox) transition between Fe^{2+}/Fe^{3+} controls the degree of crosslinking in a polymer. Given the known correlation between crosslink density and the stiffness of polymeric materials, the mechanical properties of the bulk material should be reversibly controlled by the interconversion of Fe^{2+} and Fe^{3+}. EPEHs display a unique and valuable property and that is *reversible* changes in mechanical stiffness using only electrical input (Calvo-Marzal et al., 2011). Moreover, electrically stimulated, these materials no longer exhibit the issue of time response, heat- transfer induced phase transformation and heat energy dissipation. In addition, the focus of their response is only on modulus change, and not force application or shape change, so they are ideally suited for the type of morphing that is the focus of this work.

1.3 SIGNIFICANCE OF THE WORK

The goal in all the previous shape change works has aligned with one of the following categories: *(a)* to characterize the elastomechanical behavior of a particular adaptive material/structure to accommodate shape change; *(b)* to optimize the actuators' placement to achieve the exact structural shape; or *(c)* to optimize the shape of the structure to satisfy design variables. To the best of our knowledge, with the exception of morphing skins mentioned above, no former study has looked into the structural stiffness change as an effective means of spatial shape change while the actuators are limited and fixed. Very little attention has been given to the concept of explicitly combining modulus change with applied forces to enhance shape changing flexibility.

The focus on this study is primarily to demonstrate the expansion of the spatial domain of a deformed structure due to modulus change, while the actuators are limited and fixed.

To elucidate, consider the cantilever beam shown in Figure 1-12a. The beam is formed by a smart material and is subjected to a constant transverse force F_0 applied on a particular location of the structure. When the magnitude of the force and the modulus of elasticity are fixed, certain tip deformation Δ occurs due to the mechanics of the beam (Figure 1-12b). If a larger tip displacement (Δ_d) is desired, the traditional approach is to either increase the force magnitude or move the force to the location closer to the tip to induce larger bending moment; however, an alternative strategy to achieve the desired tip displacement is to soften the beam by reducing the modulus in a portion or over the entirety of its length (Figure 1-12c).

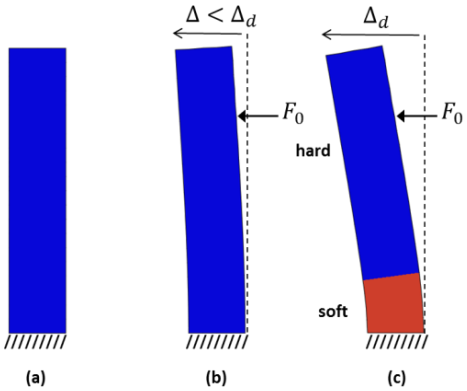

Figure 1-12: Morphing the tip to the desired displacement by local softening.
(a) undeformed column; (b) deformed column in hard phase; (c) deformed column softened locally.

Now, let the objective be to reduce the required actuating force rather than increase tip deformation. As another advantage, local softening allows the tip to displace to the same amount (Δ_1) using a lower magnitude actuation force (Figure 1-13).

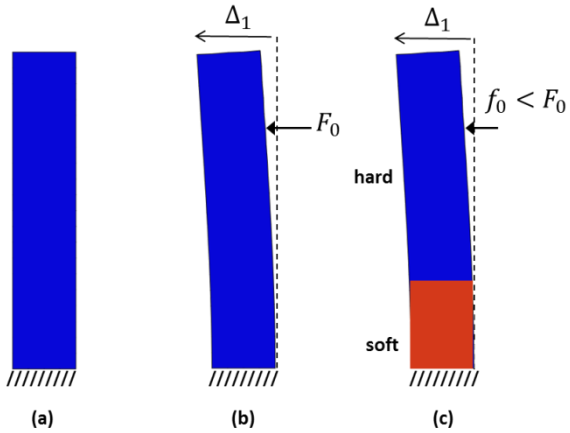

Figure 1-13: Same desired tip deformation with local softening and lower force

In these examples, with local softening, one can greatly increase the *morph space* (i.e. the set of deformations that can be achieved), with a given set of actuation force and location. Many morphing applications are limited by actuation force, so structural softening is a way to get the same or even greater morph space with lower forces and limited force locations.

In the context of shape morphing, there are two primary concepts: (a) *forward morphing*: that is, to determine the achievable shapes with different local softening strategies with a given set of force level and location (Figure 1-14a,b,c); and (b) *inverse morphing*: that is, to determine the optimal softening strategy and actuation condition which drives the structure to a given target shape as accurately as possible (Figure 1-14d).

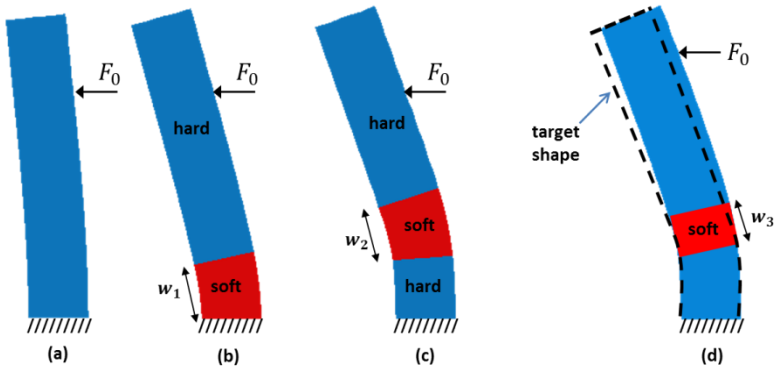

Figure 1-14: (a-c): Forward morphing; (d) inverse morphing with a given force magnitude and location

This work addresses the structural shape morphing from this new perspective. The goal is to incorporate morphing materials into a structure, and utilize the material's controllable modulus change to enhance the ability to morph the structure with *limited* actuator numbers, locations, and force levels to desired shapes that could not be achieved in the native structure.

A significant portion of the work is to demonstrate the capability of the proposed strategy to broaden the morph space within the elastic range. In order to quantify the morphed shapes, a specific planar structure with defined boundary condition, i.e. a simply supported beam, is selected as the model.

The focus of this study is not the temporal change of the material's phase or the structural shape, but rather on the spatial distribution of the structure due to modulus change. In this work no particular morphing material is considered, but rather it has been assumed that variation of

modulus is correlated with stimulus values. In fact, the focus of this work is mainly on the process used to morph a given structure, and could be used for any morphing material by incorporating the material properties into the algorithm. As will be shown, this work is distinguished from optimal actuator placement in that modulus is also an optimization variable in addition to actuators' position and magnitude.

1.4 SCOPE OF THE WORK

The focus on this study is on the spatial variation of the structure due to modulus change. Chapter 2 explores the concept of forward morphing. In this chapter, shape variation due to a single load will be studied. It reveals how controlled change of the modulus will result in significantly extended morphing space while the loading (location and magnitude) and boundary conditions remains fixed. The extent of the morph space is quantified in terms of loading and geometrical parameters. This chapter lays the groundwork for the inverse morphing problem. The problem of inverse morphing is thoroughly investigated in chapter 3, that is, to find the set of softening regions and actuation forces that produce a desired shape. It is likely that target shapes can be most readily represented as geometric B-splines or curves that are initially created in a computer aided drawing (CAD) program. Algorithms to extract the explicit coordinates from CAD curves are developed. Obviously, using a proper optimization algorithm is essential in an inverse problem. In this work a Genetic Algorithm (GA) is used. As the work progresses, the actuation and softening constraints are relaxed. This implies, given only the discrete finite location of actuation points, what optimal softening conditions (i.e. soft segment centers and lengths) and loading magnitudes could navigate the beam to the desired shape while the elastic

stability is not violated. Chapter 4 explores the inverse morph with multiple actuations when more complex beam shapes are expected. A new approach to find the actuators' bound is presented. Also, an expanded performance index which includes modulus change and external work is introduced. Chapter 5 is specifically dedicated to shape morphing of arbitrary structures. A numerical algorithm is developed and used to analyze a real practical morph problem. After validating the approach, the problem of sequential morph for multi-step shape change is explored.

1.5 CHALLENGES OF THE WORK

A challenging step of the work has been to quantify the enhanced morph space in terms of softened region, forcing and geometrical parameters. To address this, shape equations were formulated and versatile morphing schemes were explored. Ensuring the elastic stability of the morphed shapes comprised another crucial part of this work.

The inverse shape morphing problem constitutes a main portion of the study. The major challenge was to determine a *unique* set of forces and soft modulus regions under which the structure morphs to the desired shape. Developing the B-spline conversion algorithms was a major step. Moreover, several subroutines were written to automate the optimization process. For a comprehensive performance index, a challenging part was to incorporate force and modulus variation and determine the appropriate weights.

For numerical simulation of the morph, we faced more challenges. Subroutines had to be expanded to address the new algorithm and structure. Also, the previous error computation

approach was found to have shortcomings in dealing with converted spline points and had to be modified.

The sequential morph study required considerable effort. A major portion of the work involved adapting the optimization routine to the way the FE program deals with sequential loading cases. For this purpose, various approaches using a simple mass-spring model were investigated to present the approach in simple terms.. Furthermore, developing the subroutines to accomplish the task was as well challenging.

2.0 FORWARD SHAPE MORPHING

In this chapter, the concept of shape morphing of a structure with variable stiffness has been more extensively explored. To illustrate the morph locus which is used throughout the study, a variable-stiffness spring model is chosen in the beginning and furthermore a simply supported beam model has been employed.

2.1 VARIABLE-STIFFNESS SPRINGS

Consider a spring, subjected to a constant force P, whose stiffness can be tuned to a lower (k_L), an intermediate (k_M) and a higher value (k_H) (Figure 2-1). While the spring softens under the action of a constant applied force, the tip morphs along a path (here a line), which is known as *morph locus*. The morph locus could be quantified in terms of the spring constant and specifies the spatial orientation of the spring at each stiffness value.

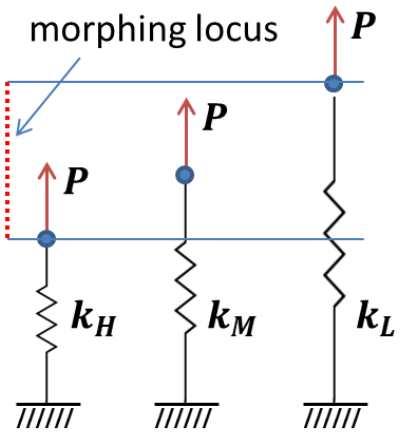

Figure 2-1: Morph locus for the tip of a variable-stiffness spring

Now, consider the rigid rod shown in Figure 2-2a, that is connected to the ground via four parallel springs and a constant force is applied in the center (point c). Each spring can have two different stiffness values, i.e. soft (k_s) and hard (k_h). With equal spring stiffnesses, the rod is in the horizontal orientation at some arbitrary deflection. Softening individual springs causes the rod to take on a nonzero slope. One can describe the rod's orientation by the height (h_c) and the angle of the center point (θ_c).

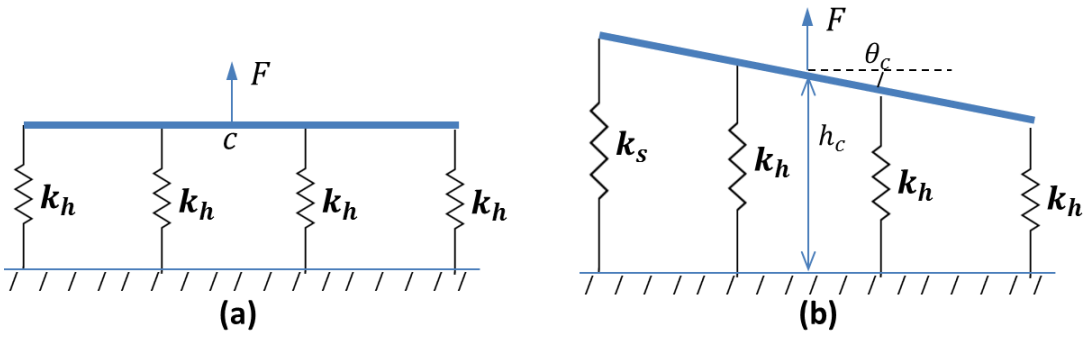

Figure 2-2: Orienting a rod using stiffness manipulation.
(a) Horizontal rod with equal spring stiffness; (b) Inclined rod with one softened spring

A *morphing scheme* is defined based on the arrangement of soft springs. Let us consider a particular scheme in which, with fixed magnitude and location of the force, the stiffness starts

decreasing from the left spring and softening consecutively continues to the right side while the left springs remain soft. At every step, a normalized discrete variable r specifies the configuration of softened elements (Eq. 2.1). Figure 2-3 shows two consecutive arrangements.

$$r = \frac{\text{number of softened springs}}{\text{number of total springs}} \tag{2.1}$$

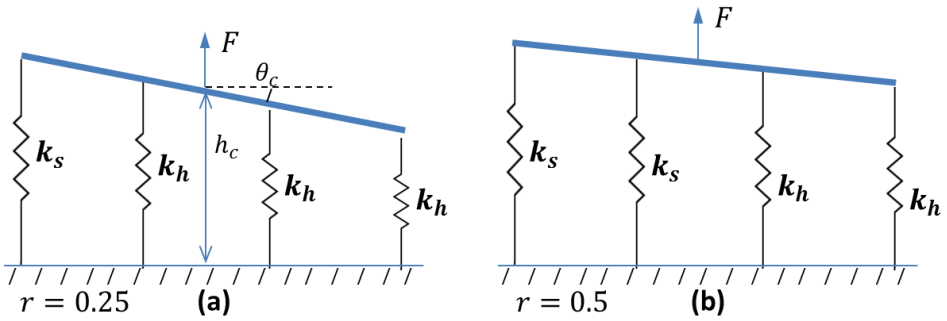

Figure 2-3: Rod orientations in two consecutive softened conditions

The morphing loci of the center point are shown in Figure 2-4 for the two measures of deflection (h_c and θ_c). These plots represent the orientation of the rod in morphing with various spring constants. The discrete angle and height parameters can be determined from the governing equilibrium equations.

Note that softening the springs enables two key expanded features of the possible bar positions and orientations. First, most of the orientations shown in Fig. 2-4 cannot be obtained without softening when the force location is fixed in the center of the rod. Second, the rod deflected height can be greater when the springs are softened than when in their hard state (or equal deflection can be achieved with lower required force magnitude). Various other rod orientations could be obtained by implementing different morphing schemes (i.e. springs'

softening sequence). The total set of rod deflections and orientations that can be achieved with such morphing schemes is the morphing space.

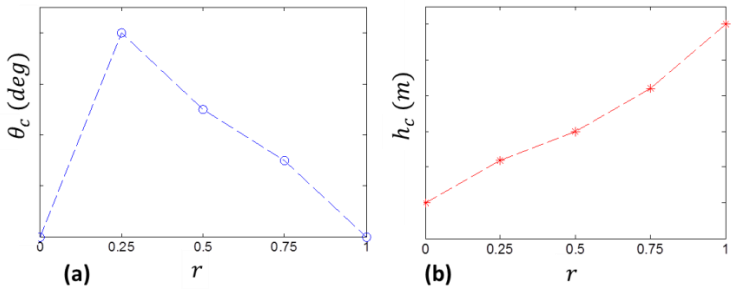

Figure 2-4: Morphing loci of the rod center point: (a) angle; (b) height

To better illustrate the morph space in this example, we will plot the height (h_c) versus angle of the center point (θ_c), as shown in Figure 2-5. Depending on the variability of the force and spring stiffness, four possible cases are defined (Table 2-1). If one plots the height (h_c) versus angle of the center point (θ_c), Figure 2-5 is resulted. With fixed force and high stiffness, the rod can orient in only one particular configuration (i.e. point morph space). As the force changes, yet the springs are equally stiff, the morph space changes to a vertical line. When the force remains constant but the springs soften, a two-dimensional morph space is achieved (an example morph space is shown in Figure 2-5. Largest morph space is obtained in case 4 when both force and stiffness are allowed to change. While the actuation location and capacity is limited, stiffness variation is a sound strategy to morph the rod to a more expanded space.

Table 2-1: Cases with force and spring stiffness variation

Case	F	k
1	C	C
2	V	C
3	C	V
4	V	V

*** C**: Constant , **V**: Variable

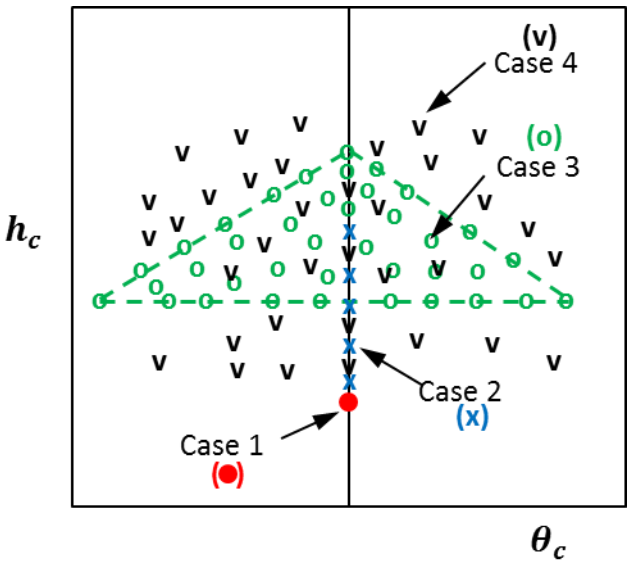

Figure 2-5: Morph space variation in different cases

The two examples shown above illustrate the basic concept of morphing to be explored in this dissertation. By adjusting structural stiffness one can use a single force to obtain a locus of structural shapes, with degrees of freedom greater than the number of forces applied (as illustrated by the changing position and angle in the second example). The remainder of the work will explore using this concept in more complex structures in which the forward and inverse relationships between applied forces, spatial stiffness parameters, and final shape are not trivial. A simply-supported beam will be used to formulate the methods used. With known governing equations, one can analytically quantify the morphed shapes in this structure. Meanwhile, the two-dimensional geometry is not too complex for shape characterization.

2.2 A SIMPLY SUPPORTED BEAM: SHAPE EQUATIONS

This section explores the shape morphing of a simply supported beam. The beam is subjected to a single transverse load and the governing elasticity equations for the shape of the elastic beam are derived. The feasible achievable morph locus has been respectively quantified in terms of the loading, geometry and mechanical properties.

Figure 2-6 shows a simply supported two-dimensional beam. Let P is a transverse point load, applied at a distance a from the left support and L is the length of the beam. The modulus of elasticity is represented by E.

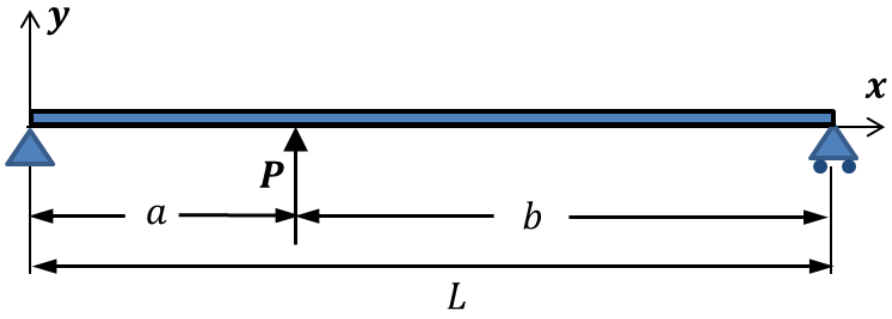

Figure 2-6: Simply supported beam with concentrated load

Assuming no warping and out-of-plane deformation, the governing equations for the elastic deformation of the beam can be represented by Eq. (2.2):

$$M(x) = EI\frac{d^2y}{dx^2} \tag{2.2}$$

Where $M(x)$ is the bending moment due to the force P measured at the distance x from the left support. From the balance of moments, one can rephrase the bending moment using Eq. (2.3).

$$M(x) = -\frac{Pb}{L}x + P < x - a > \tag{2.3}$$

where <> is the *singular function operator* which, for any function $f(x)$ is defined as:

$$< f(x) >= \begin{cases} f(x) & f(x) \geq 0 \\ 0 & f(x) < 0 \end{cases} \tag{2.4}$$

Integrating Eq. (2.3) twice results the displacement:

$$y(x) = \frac{1}{EI}\left(-\frac{Pb}{6L}x^3 + \frac{1}{6}P < x - a >^3 + c_1 x + c_2\right) \tag{2.5}$$

The boundary conditions for the simply supported beam are specified as:

$$\begin{aligned} y(x)|_{x=0} &= 0 \\ y(x)|_{x=L} &= 0 \end{aligned} \tag{2.6}$$

Replacing the latter boundary conditions into Eq. (2.6) and solving for constants c_1 and c_2 results in:

$$c_1 = \frac{1}{6}Pb\left(L - \frac{b^2}{L}\right),\ c_2 = 0 \tag{2.7}$$

From Eq. (2.5), one can derive the governing equation for the shape of the elastic beam:

$$y(x) = \frac{1}{6EI}(-Pbx^3 + PL < x - a >^3 + Pb(L^2 - b^2)\,x) \tag{2.8}$$

As a simplified case, let $a = b = L/2$; In this case, Eq. (2.8) turns into:

$$y(x) = \frac{1}{6EI}\left(-\frac{PL}{2}x^3 + PL < x - \frac{L}{2} >^3 + \frac{3}{8}PL^3\,x\right) \tag{2.9}$$

2.3 BEAM WITH VARIABLE MODULUS

Assume that the described beam is formed by a smart material and the modulus of elasticity can change selectively via a stimulus in part/entire of the beam. This section explores the governing beam shape equations.

2.3.1 Single soft segment

Figure 2-7 displays the single actuated supported beam with one soft segment. For the sake of simplicity, let the distribution of the modulus be described by a piecewise function, i.e. the modulus at any location along the beam switches between two discrete values, E_h the hard state modulus and E_s the soft state modulus (see Eq. 2.10).

$$E(x) = \begin{cases} E_h & 0 \le x \le x_1 \\ E_s & x_1 \le x \le x_2 \\ E_h & x_2 \le x \le L \end{cases} \tag{2.10}$$

As a convention for the rest of this work, *soft segment* is the term used to describe the region with lower modulus (E_s). Each segment (indicated by circled number) has been distinguished by a change in stiffness at locations x_1 and x_2.

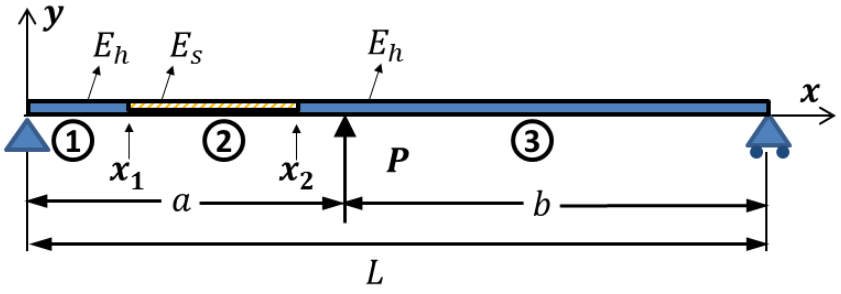

Figure 2-7: Loaded supported beam with variable modulus of elasticity

For this structure, the governing elastomechanical equations can now be redefined as:

$$M(x) = E(x)I\frac{d^2y}{dx^2} = -\frac{Pb}{L}x + P < x - a > \tag{2.11}$$

Followed by

$$\frac{dy}{dx} = \theta(x) = \frac{1}{E(x)I}\left(-\frac{Pb}{2L}x^2 + \frac{1}{2}P < x - a >^2 + c_1\right) \tag{2.12}$$

And the elastic shape equation can be represented by:

$$y(x) = \frac{1}{E(x)I}\left(-\frac{Pb}{6L}x^3 + \frac{1}{6}P < x - a >^3 + c_1x + c_2\right) \tag{2.13}$$

Let y_1, y_2 and y_3 represent the displacement in three segments respectively. In addition to two previous boundary conditions (i.e. zero deformation at the ends), there are two more shape continuity constraints, i.e. function and slope values, for each section. This is described in the following three sets of equations:

$$\begin{aligned} y_1(x)|_{x=0} &= 0 \\ y_3(x)|_{x=L} &= 0 \end{aligned} \tag{2.14}$$

$$\begin{aligned} y_1(x)|_{x1} &= y_2(x)\,|_{x1} \\ y_2(x)|_{x2} &= y_3(x)\,|_{x2} \end{aligned} \tag{2.15}$$

$$\begin{aligned} \left.\frac{dy_1}{dx}\right|_{x1} &= \left.\frac{dy_2}{dx}\right|_{x1} \\ \left.\frac{dy_2}{dx}\right|_{x2} &= \left.\frac{dy_3}{dx}\right|_{x2} \end{aligned} \tag{2.16}$$

Eqs. (2.14-16) can be summarized in the following form:

$$\begin{cases} \frac{1}{E_s}c_1^2 - \frac{1}{E_h}c_1^1 = (\frac{1}{E_h} - \frac{1}{E_s})\, f(x_1) \\ \frac{1}{E_s}c_1^2 - \frac{1}{E_h}c_1^3 = (\frac{1}{E_h} - \frac{1}{E_s})\, f(x_2) \\ \frac{-1}{E_h}x_1c_1^1 + \frac{1}{E_s}x_1c_1^2 - \frac{1}{E_h}c_2^1 + \frac{1}{E_s}c_2^2 = (\frac{1}{E_h} - \frac{1}{E_s})\, g(x_1) \\ \frac{1}{E_s}x_1c_1^2 - \frac{1}{E_h}x_2c_1^3 + \frac{1}{E_s}c_2^2 - \frac{1}{E_h}c_2^3 = \left(\frac{1}{E_h} - \frac{1}{E_s}\right)\, g(x_2) \\ c_2^1 = 0 \\ Lc_1^3 + c_2^3 = g(x_1) \end{cases} \tag{2.17}$$

where c_1^i and c_2^i are the constants for to the i^{th} section and $f(x)$ and g(x) defined as:

$$f(x) = -\frac{Pb}{2L}x^2 + \frac{1}{2}P < x - a >^2 \tag{2.18}$$

$$g(x) = -\frac{Pb}{6L}x^3 + \frac{1}{6}P < x - a >^3 \tag{2.19}$$

Rearranging Eq. (2.17) in closed-form yields:

$$\begin{bmatrix} -E_h^{-1} & E_s^{-1} & 0 & 0 & 0 & 0 \\ 0 & E_s^{-1} & -E_h^{-1} & 0 & 0 & 0 \\ 0 & 0 & 0 & 1 & 0 & 0 \\ -x_1E_h^{-1} & x_1E_s^{-1} & 0 & -E_h^{-1} & E_s^{-1} & 0 \\ 0 & x_2E_s^{-1} & -x_2E_h^{-1} & 0 & E_s^{-1} & -E_h^{-1} \\ 0 & 0 & L & 0 & 0 & 1 \end{bmatrix} \begin{bmatrix} c_1^1 \\ c_1^2 \\ c_1^3 \\ c_2^1 \\ c_2^2 \\ c_2^3 \end{bmatrix} = A \begin{Bmatrix} f(x_1) \\ f(x_2) \\ 0 \\ g(x_1) \\ g(x_2) \\ -A^{-1}g(L) \end{Bmatrix} \tag{2.20}$$

where $A = E_h^{-1} - E_s^{-1}$. The left matrix in the above equation solely consists of the material and geometrical properties and can be determined in the initial stages of the solution. The vector on the right hand side only includes the actuation conditions (magnitude and location) and is thus known. Therefore Eq. (2.20) can be solved for constants c_1 and c_2 in each segment. The elastic shape of the beam is obtained by summation of the piecewise displacement functions:

$$y(x) = H_1 y_1(x) + H_2 y_2(x) + H_3 y_3(x) \tag{2.21}$$

where $H(x)$ is the *Heaviside* function defined by:

$$H(x) = \begin{cases} 1 & within\ boundaries \\ 0 & outside\ boundaries \\ 1/2 & on\ the\ boundaries \end{cases} \tag{2.22}$$

In particular cases, the soft segment begins from one of the supports (Figure 2-8).

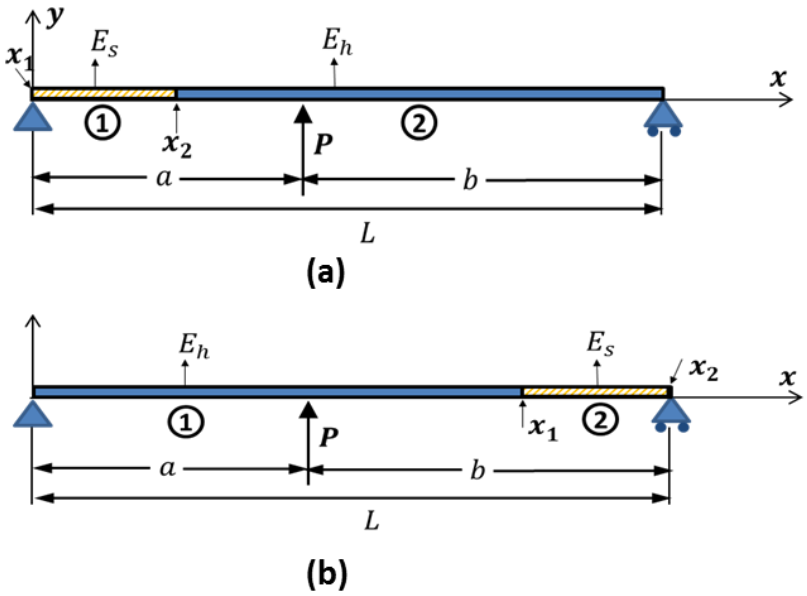

Figure 2-8: Soft segment falls on one of the supports

The closed-form governing equations are simplified to the following forms for cases a and b in Figure 2-8, respectively:

$$\begin{bmatrix} E_s^{-1} & -E_h^{-1} & 0 & 0 \\ x_2E_s^{-1} & -x_2E_h^{-1} & E_s^{-1} & -E_h^{-1} \\ 0 & 0 & 1 & 0 \\ 0 & L & 0 & 1 \end{bmatrix} \begin{bmatrix} \boldsymbol{c_1^1} \\ \boldsymbol{c_1^2} \\ \boldsymbol{c_2^1} \\ \boldsymbol{c_2^2} \end{bmatrix} = \begin{Bmatrix} Af(x_2) \\ Ag(x_2) \\ 0 \\ -g(L) \end{Bmatrix} \tag{2.23}$$

$$\begin{bmatrix} -E_h^{-1} & E_s^{-1} & 0 & 0 \\ -x_1E_h^{-1} & x_1E_s^{-1} & -E_h^{-1} & E_s^{-1} \\ 0 & 0 & 1 & 0 \\ 0 & L & 0 & 1 \end{bmatrix} \begin{bmatrix} \boldsymbol{c_1^1} \\ \boldsymbol{c_1^2} \\ \boldsymbol{c_2^1} \\ \boldsymbol{c_2^2} \end{bmatrix} = \begin{Bmatrix} Af(x_1) \\ Ag(x_1) \\ 0 \\ -g(L) \end{Bmatrix} \tag{2.24}$$

The edges of the segment (x_1, x_2) can then be readily determined by knowing the center and length of each segment (x_s, w_s).

2.3.2 Multiple soft segments

To generalize the modulus variation within the domain, consider the beam shown in Figure 2-9 with soft and hard segments designated by E_s and E_h respectively.

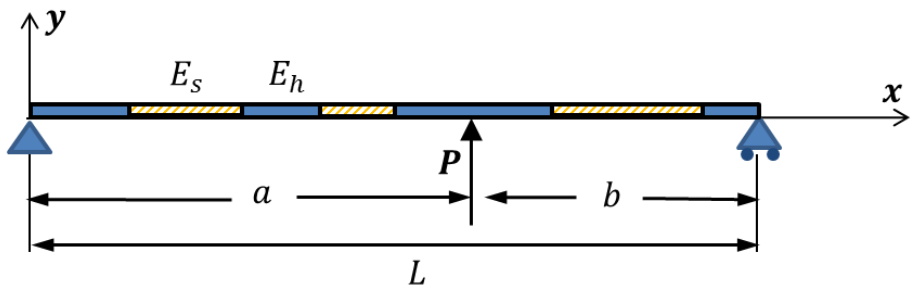

Figure 2-9: Single actuated beam with multiple soft segments

Let N be the total number of segments and N_s is the number of soft segments. The i-th segment is represented by its start and end points, x^i and x^{i+1} (Figure 2-10a). The k-th *soft*

segment is characterized by its two points (x_1^k and x_2^k) which are dependent on x_s^k , the center point, and w_s^k, the segment length (Figure 2-10b).

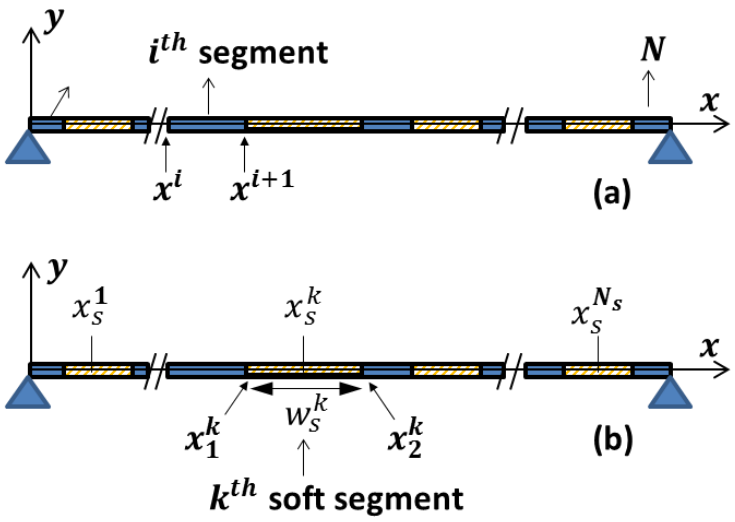

Figure 2-10: Segment definition using geometry points
(a) i-th segment is described by start/end points; (b) Each soft segment is represented by its center point x_s and length w_s

Depending on the configuration of the soft segments, the total number of segments may differ. For example, Figure 2-11 shows four various arrangements of three low modulus regions.

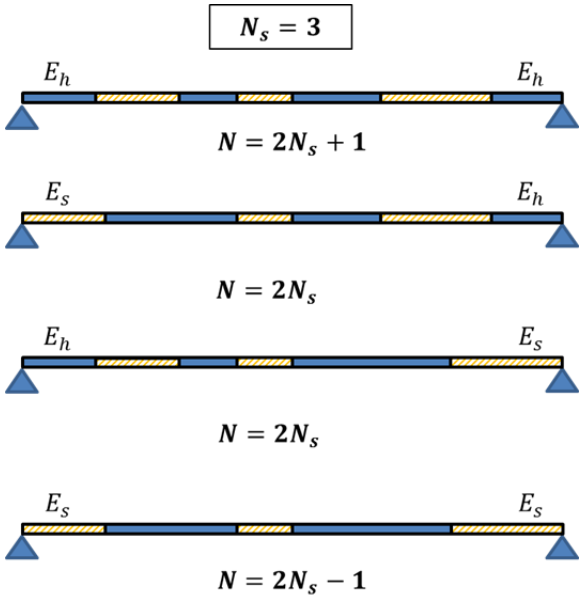

Figure 2-11: Different soft segments arrangement affects the total number of segments

In general, one could obtain the total number of segments from Eq. (2.25):

$$N = 2N_s + 1 - h_1 - h_2 \tag{2.25}$$

where h_1 and h_2 are either 1 or 0 and their values are determined based on the position of the outermost left and right segments respectively (Eq. 2.26).

$$h_1 = \begin{cases} 1 & x_1^1 = 0 \\ 0 & otherwise \end{cases}$$

$$h_2 = \begin{cases} 1 & x_2^{N_s} = L \\ 0 & otherwise \end{cases} \tag{2.26}$$

Similar to the previous section, two boundary conditions at each segment intersection need to be satisfied. For the i-th section shown in Figure 2-10a, let E_i and E_{i-1} be the moduli of the current and previous sections. The slope and deflection continuity at point x^i can be presented by Eqs. (2.27-28).

$$\frac{1}{E_{i-1}}\boldsymbol{c_1^{i-1}} - \frac{1}{E_i}\boldsymbol{c_1^i} = (\frac{1}{E_{i-1}} - \frac{1}{E_i})\, f(x^i) \tag{2.27}$$

$$\frac{-1}{E_{i-1}}x^i\boldsymbol{c_1^{i-1}} + \frac{1}{E_i}x^i\boldsymbol{c_1^i} - \frac{1}{E_{i-1}}\boldsymbol{c_2^{i-1}} + \frac{1}{E_i}\boldsymbol{c_2^i} = (\frac{1}{E_{i-1}} - \frac{1}{E_i})g(x^i) \tag{2.28}$$

where $f(x)$ and g(x) are force-related functions described by Eqs. (2.18-19). $\boldsymbol{c_1}$ and $\boldsymbol{c_2}$ are segment constants. At the supports, these constants should satisfy the following conditions:

$$\boldsymbol{c_2^1} = 0$$
$$L\boldsymbol{c_1^{N_s}} + \boldsymbol{c_2^{N_s}} = -g(L) \tag{2.29}$$

Following the same procedure as was taken for a single soft segment, one can consolidate the continuity equations for all the segments into the following closed-form representation:

$$\begin{bmatrix} \cdots & & i-1 & i & \cdots & \cdots & & i+N_s-1 & i+N_s & \cdots & \\ \vdots & & & & & & & & & & \\ i-1 & & -E_{i-1}^{-1} & E_i^{-1} & & & & & & & \\ \vdots & & & & & & & & & & \\ i+N_s-2 & & -x^i E_{i-1}^{-1} & x^i E_i^{-1} & & & & -E_{i-1}^{-1} & E_i^{-1} & & \\ \vdots & & & & & & & & & & \\ 0 & & 0 & 0 & N_s & N_s+1 & & & & 2N_s & \\ 0 & \cdots & 0 & 0 & 2N_s\ L & 0 & \cdots & 0 & 0 & 2N_s\ 1 & \end{bmatrix} \begin{bmatrix} \vdots \\ c_1^{i-1} \\ c_1^i \\ \vdots \\ c_1^{n_s} \\ \vdots \\ c_2^{i-1} \\ c_2^i \\ \vdots \\ c_2^{n_s} \end{bmatrix} = \begin{Bmatrix} \vdots \\ A_i f(x^i) \\ \\ A_i g(x^i) \\ \vdots \\ 0 \\ -g(L) \end{Bmatrix} \tag{2.30}$$

A part of the matrix corresponding to the equations of the i-th segment has been highlighted. The material constant A is defined by:

$$A_i = (-1)^{i+h_1}(E_h^{-1} - E_s^{-1}) \tag{2.31}$$

where h_1 is a piecewise constant function whose value depends on the location of the outermost left soft segment:

$$h_1 = \begin{cases} 1 & x_1^1 = 0 \\ 0 & otherwise \end{cases} \tag{2.32}$$

The shape of the deflected structure is represented in the following form:

$$y(x) = \sum_{i=1}^{N_s} H_i y_i(x) \tag{2.33}$$

where H_i is the *Heaviside* function and y_i is the i-th segment's deflected shape function:

$$y_i(x) = \frac{1}{E_i}\left(g(x) + c_1^i x + c_2^i\right) \tag{2.34}$$

2.4 NUMERICAL VERIFICATION

In order to verify the analytical results, a finite element (FE) analysis was performed using ABAQUS ver. 6.8.1®. Python scripts were created to interact with the FE result database and with MATLAB© to simulate the morphed shapes. A linear 2D beam element (B21) with rectangular cross section was chosen. This element represents a Timoshenko beam and is useful for modeling thin or thick members. As the beam becomes slender, Euler-Bernoulli theory is approximated. Table 2-2 describes the simulated model specifications.

Table 2-2: Specification of the simulated beam model

Variable	Description	Value	Unit
Geometrical Properties			
L	Beam Length	200	mm
W	Width of rectangular section	10	mm
H	Height of rectangular section	2	mm
Material Properties			
E_h	Hard phase modulus	3000	MPa
E_s	Soft phase modulus	750	MPa
ν_h, ν_s	Poisson's ratio (hard&soft phase)	0.3	–

An initial mesh size of $2mm$ was assigned for FE simualtion. A comparison of the numerical and analytical results for this example has been demonstrated in Figure 2-12.

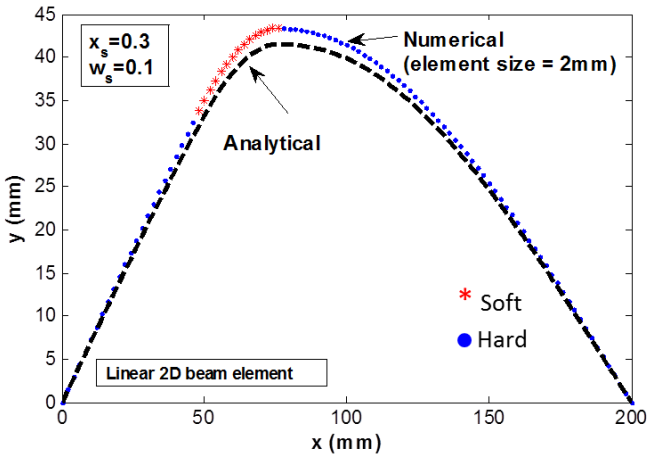

Figure 2-12: Analytical vs. numerical displacement (coarse mesh)

An approximate maximum shape error of 4% is observed in the vicinity of the peak point. In order to lessen the error, finer elements with size decreasing increment of $0.5mm$ (i.e. $1mm, 0.5mm, 0.25mm$ and $0.1mm$) are replaced. Figure 2-13 shows the numerical vs. analytical solutions on the peak region with different mesh sizes. The RMS error is plotted in Figure 2-14.

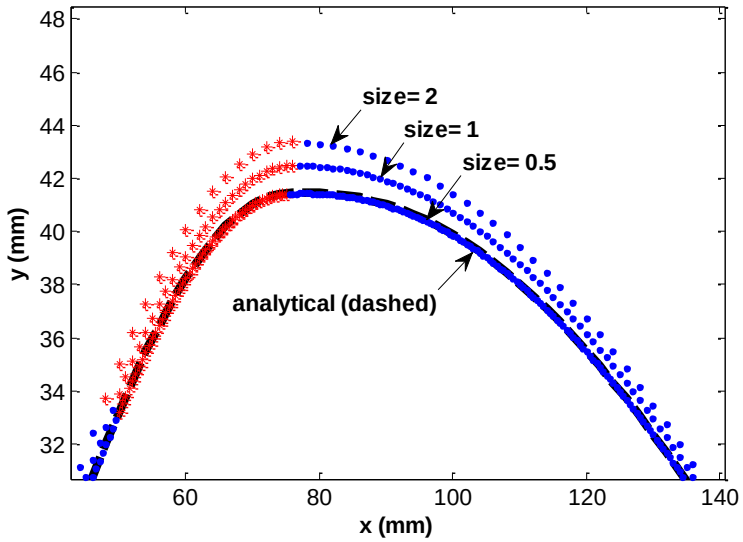

Figure 2-13: Numerical vs. analytical solutions on the peak region with different mesh sizes

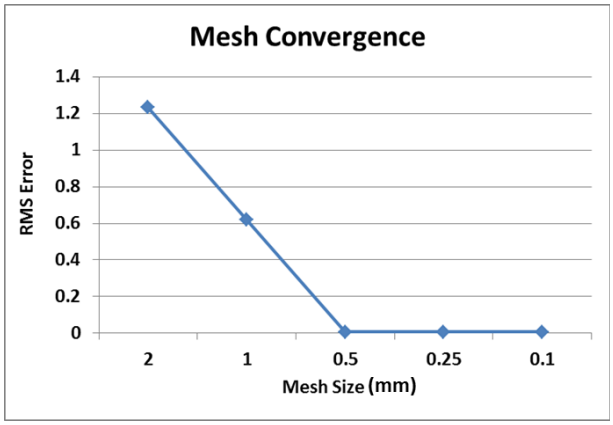

Figure 2-14: Mesh convergence for the numerical simulation

It can be seen that the FE solution has converged after $0.5mm$ mesh.It is assumed that this element size satisfies the mesh convergence for all other modulus distributions, so it will be used for further simulations.

2.5 STRESS, CURVATURE AND PERMISSIBLE FORCE

Figure 2-15 shows a section of the beam undergoing bending before and after the deformation, where M is the bending moment at the section, ρ is the radius of curvature and y is the distance from the neutral axis of the beam.

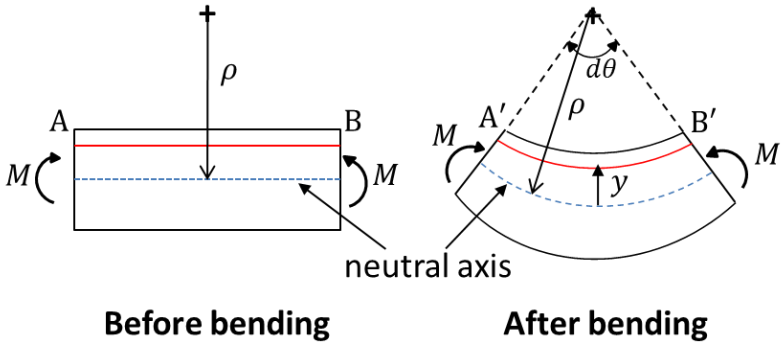

Figure 2-15: Section of the beam before and after bending

The strain along a line segment (AB) in the top surface is calculated from Eq. (2.35):

$$\epsilon = \frac{\overline{A'B'} - \overline{AB}}{\overline{AB}} \tag{2.35}$$

where $\overline{AB}$ and $\overline{A'B'}$ are the lengths of segment before and after the deformation:

$$\begin{aligned} \overline{AB} &= \rho d\theta \\ \overline{A'B'} &= (\rho - y)d\theta \end{aligned} \tag{2.36}$$

Substituting in Eq. (2.38) results in

$$\epsilon = \frac{y}{\rho} = \kappa y \tag{2.37}$$

where κ is the curvature. Stress can be related to the curvature by Hooke's law:

$$\sigma = E\epsilon = Ey\kappa \tag{2.38}$$

The latter equation for the maximum stress will turn into:

$$\sigma = Ec\kappa \tag{2.39}$$

where c is the maximum distance from the neutral axis. This formula shows a direct relationship between the maximum bending stress and the maximum curvature:

$$\sigma_{max} \propto \kappa_{max} \tag{2.40}$$

Figure 2-16 illustrates the bending moment diagram of a simply supported beam with a single load, where the maximum bending moment is given by:

$$M_{max} = \frac{Pab}{L} \tag{2.41}$$

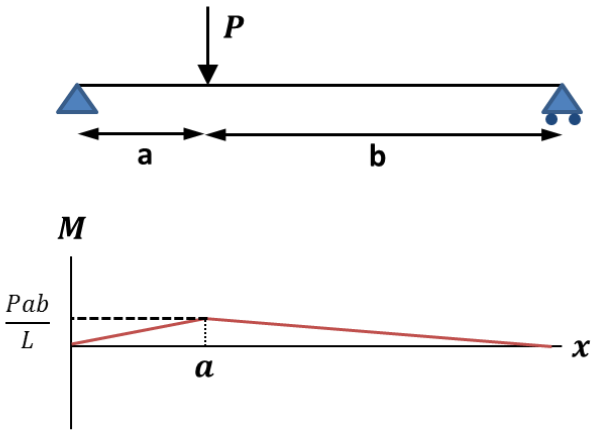

Figure 2-16: Bending moment diagram in a single-loaded supported beam

Assuming elastic deformation, maximum normal stress can be related to maximum bending moment via the following equation:

$$\sigma_{max} = \frac{M_{max}c}{I} \tag{2.42}$$

The stress-strain curve for an elastic material is presented in Figure 2-17.

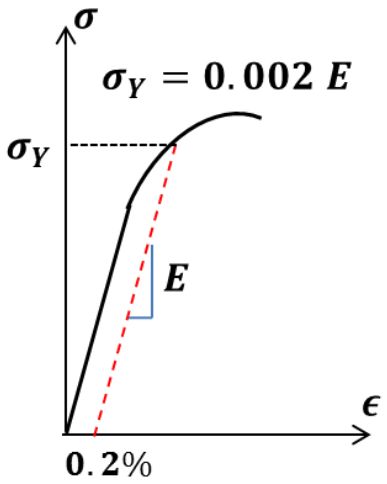

Figure 2-17: Elastic stress vs. strain curve

To ensure the elastic stability of the material, the maximum stress in the curve should not exceed the yield stress, which is related to the modulus by Eq. (2.43).

$$\sigma_Y = 0.002E \tag{2.43}$$

By combining Eqs. (2.41-43), the force that causes the structure to yield, P_Y, is determined by Eq. (2.44):

$$P_Y = 0.002E\left(\frac{IL}{abc}\right) \tag{2.44}$$

This equation establishes a direct relationship between the permissible force and the modulus. Let P_Y^h and P_Y^s be the maximum permissible elastic force in the entirely hard and soft states respectively. This implies that to guarantee material stability, actuation force should satisfy Eq. (2.45).

$$|P_Y^s| \leq |P| \leq |P_Y^h| \tag{2.45}$$

2.6 MORPHING SCHEMES

In the previous section, elastic stability of a simply supported beam under a single loading was studied and relationships between the curvature, stress and permissible actuation force were established. In this section, forward morphing of the beam is explored and the relationship between the morphed shapes and morphing parameters such as number of soft segments and their location and length is established. To characterize the various achievable shapes, principal morphing schemes are introduced in which one or more soft segments are progressively placed at

different locations along the length of the beam. Each scheme comprises a certain configuration of soft segments and guides the beam into defined space. Figure 2-18 pictures a schematic of the loaded beam that will be used for all the cases in the following sections. From a conservative standpoint, the maximum allowed load (i.e. the load that does not cause yielding) in the soft state was used for all simulations.

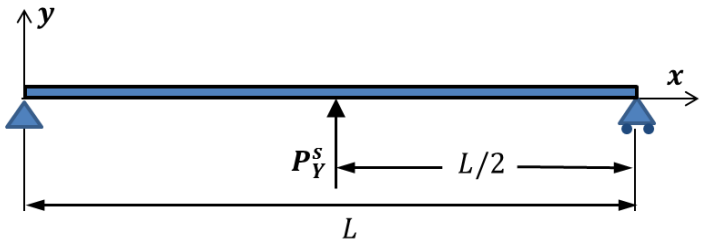

Figure 2-18: Schematic of the loaded beam in this work

2.6.1 Uni-section scheme

To explore the various achievable shapes when the beam modulus locally changes, two primary morphing schemes were considered, uni-section and bi-section morphing. Each morphing scheme comprises of certain arrangement of soft segments, as explained below.

(a) uni-section morph scheme is defined as only one section of the structure is softened. Figure 2-19 depicts three proposed patterns in a uni-section scheme. Soft segments with two different lengths have been shown. Case 1 presents a pattern in which the section is constrained on the left (or right) support while the length of the section grows. In Case 2, the soft segment grows symmetrically from the mid span. In Case 3, a soft segment with a fixed length shifts through the structure (from left end to right end, or vice versa) over consecutive stages.

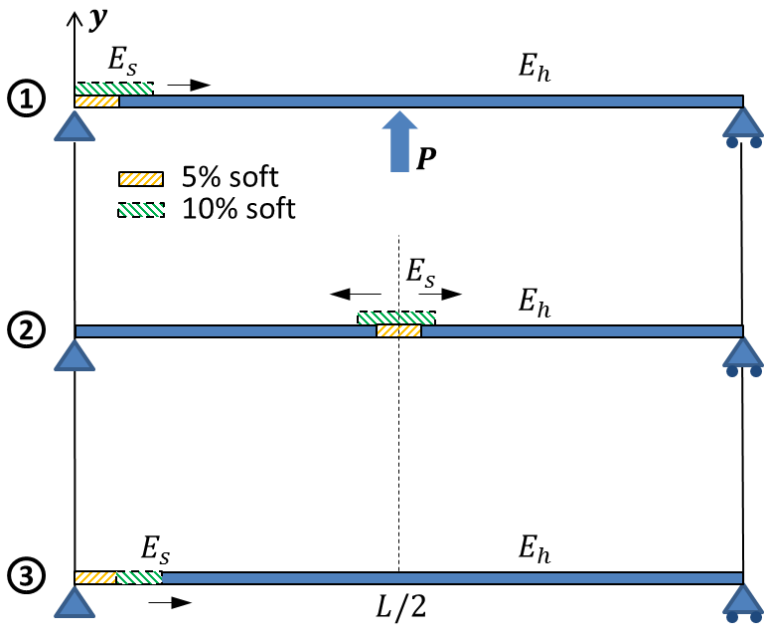

Figure 2-19: Three different patterns used in uni-section morphing scheme. Case 1) transitioned section grows from the left end of the beam, Case 2) transitioned section grows symmetrically from the mid span, and Case 3) soft segment with a fixed length shifts left end to right end.

Figure 2-20 shows the results of morphed shapes for Case 1 in which the soft segment grows from 0% to 100% of the beam length in increments of 5%. An example morphed shape, with soft segment highlighted, is shown for the 50% soft trial. Two distinct features appear in the results. First, the amplitude of shape change increases with the increased softened region, as expected. Second, for all shapes except for the fully-hard or fully-soft beam, the shape is skewed to the left (non-symmetric about the midspan). Clearly the modulus change enables an expanded space of possible shapes, not only in amplitude but in quality (in this case symmetry) too.

In order to track and quantify the spatial configuration of the beam in different morphing scenarios, it is reasonable to define a unique metric that characterizes the shape of the deflected beam. A *peak locus* is referred to as the set of the peak points during a particular morphing process (from 0% to 100% softened). A plot of peak locus demonstrates the spatial distribution of these highlighted points (see Figure 2-20). Notice the peak loci in pattern 1 form the borders

of an envelope. It is worth noting that the mirror image of the peak loci can be formed by initiating the scheme of case 1 from the right end of the beam.

Another way to interpret the curves is the space of possible beam shapes that are enabled by morphing without changing the applied force. In this work, this space is referred to as *morph space*. The lowest beam shape shown (blue dashed line at the bottom) is the shape generated when the force is applied to the original hard beam. All of the other shapes, with larger and some non-symmetric deformations, are available by changing modulus of various sections according to the scheme of Case 1.

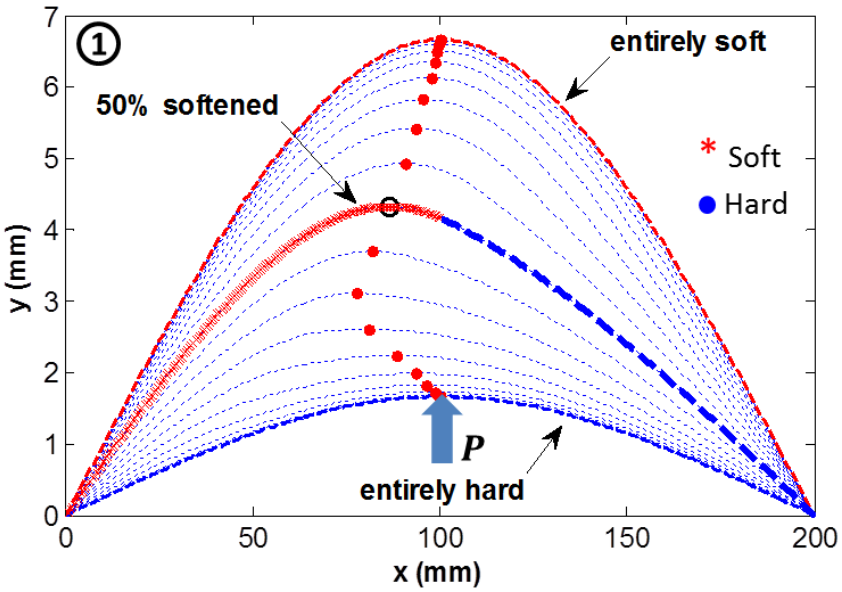

Figure 2-20: Morphed shapes with highlighted peak points (Case 1)
(fixed soft segment at the left grows to the right with 5% size increments. Mirror peak locus will form by moving the sections from right to left). An example curve with 50% soft segment is highlighted. An envelope is formed by the loci of morphed shapes' peaks and their mirror image.

Figure 2-21 pictures the morphed shapes with their highlighted peak points for Case 2. Once again, the results are shown for increasing soft segment lengths from 0% (bottom curve) to 100% (top curve) in 5% increments, but this time the soft segments are centered at the beam's midspan. As an example, one of the intermediate curves (25% softened) has been indicated. Unlike the

previous pattern, all the deformed shapes are symmetric with respect to the midspan and no deviation of the peak points is observed. One could anticipate this by considering the central and symmetric orientation of the soft segments.

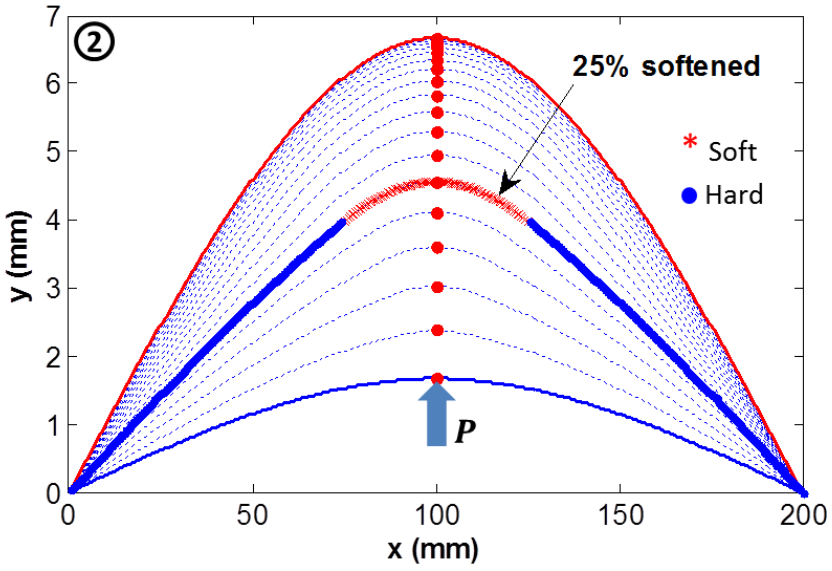

Figure 2-21: Morphed shapes with highlighted peak points (Case 2)
(fixed middle soft segment grow symmetrically to both sides in 5% increments)

Morphing under Case 3 results in asymmetric shapes. Recall that in this case, a constant length soft segment is marched along the beam from left to right. To understand the behavior, we present the results in terms of fixed-length soft segments marched along the beam, where the section length increases for each subset of data. For example, assume a constant segment length of 10% (of the total beam length). If one simulates the deflection of the beam for each marching step, Figure 2-22a is resulted. This figure contains a group of morphed shapes as the 10% soft segment marches from left to right along the beam. The larger (red) points highlight the peak beam deflections, indicating asymmetric morphing for cases in which the soft segment is off-centered (for example three instances are shown with the soft segments highlighted with (red) cross symbols, at 0.20, 0.40 and 0.70×L from the left end of the beam). The middle solid arrows

indicate the direction of peak movement as the 10% soft segment marches from left to right, starting with point *S*.

Now if one simulates the deflection of the beam with soft segments of different lengths (starting at 5% of the total beam length and increasing in section length to 50%) and marching from left or right, and the peak loci are plotted at each iteration. Figure 2-22b is resulted. As the segments become wider, the peak loci spread out in both vertical and side directions. It is interesting to note that the peak points of Case 3 occupy the inside of the envelope formed by the peak points of Case 1. Note that for all the soft segment lengths, the peaks never surpass the envelope borders.

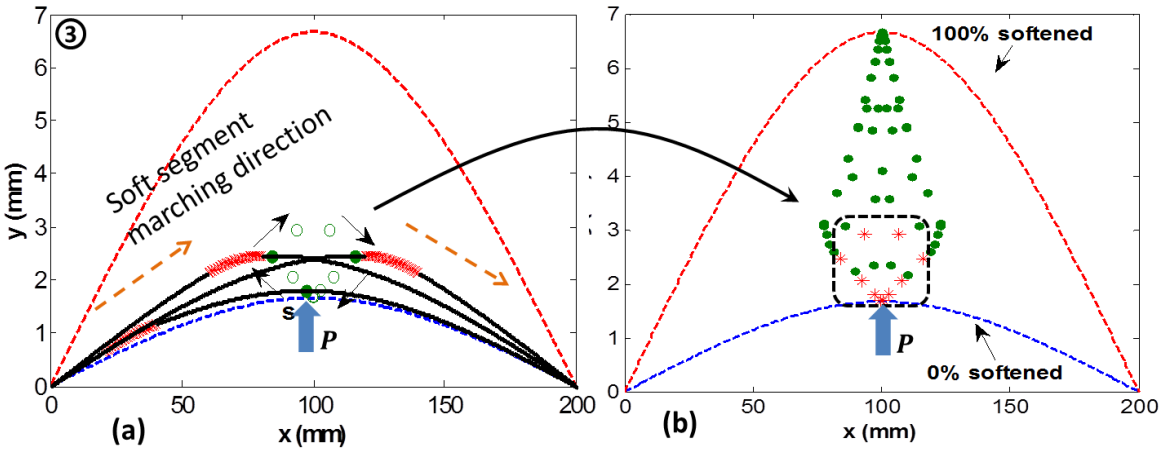

Figure 2-22: Peaks locus in asymmetric scheme (Case 3)
(a) Constant 10% segment length marching from left to the right. Sample morphed shapes are shown. Start point, S and moving direction of the peaks are specified (b) Peaks distribution for different soft segment's length (0-100%). Peak locus corresponding to 10% length is highlighted within dashed box

There are few points worth considering with regard to Case 3. Firstly, in all cases of uni-section pattern, the boundaries of the "morphing space" are represented by 0% and 100% soft segment length. Moreover, the accessible peak points (or equivalently shapes) with this pattern are significantly spatially diverse. While the morph cases 1 and 2 created shapes along the side borders and middle axis of the envelope (previously shown in Figure 2-20), the third model

could produce shapes whose peaks lie not only along the borders but also within the envelope. In addition, the distribution pattern provides a measure to quantitatively adjust the required section length to achieve the desired horizontal and vertical positions of the peak.

2.6.2 Bi-section scheme (symmetrical and unsymmetrical)

A schematic of a symmetrical bi-section morph pattern is shown in Figure 2-23 in which two separate sections are transitioned simultaneously, and their sizes grow as different trials are evaluated. The first case, which we'll call Case 4, is similar to the corresponding case in uni-section morph where the sections remain tied at the supports and their widths grow in consecutive steps. Likewise, the second case in Figure 9, which we'll call Case 5, is a marching section pattern where fixed-length segments continue to move along the structural domain.

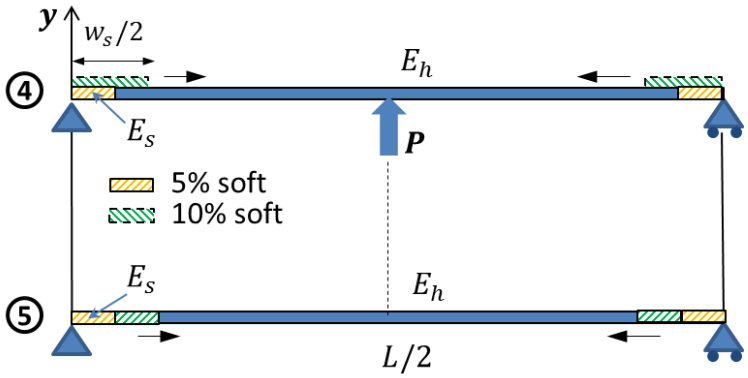

Figure 2-23: Symmetrical bi-section morph patterns (Cases 4 and 5)

The morphed shapes with their highlighted peaks are simulated in Figure 2-24. As indicated, this morphing strategy results in symmetric shapes, i.e. no spatial variation in the peak locus, but with widened curves in the vicinity of the peaks. The left plot highlights a trial in which 75% of the beam is softened, and this trial is expanded in the right plot.

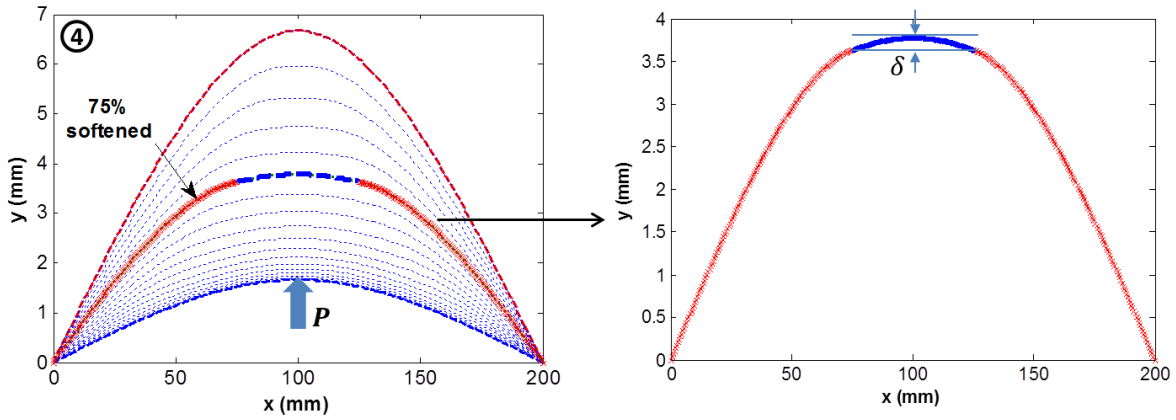

Figure 2-24: Morphed shapes in a bi-section pattern (Case 4)
(two soft segments are tied to the supports and grow in length in consecutive 5% steps)

In order to quantify the width of the shapes, a *flat zone* is defined as a part of the curve, in the neighborhood of the peak, where the displacement fluctuation remains within a certain assumed tolerance ($\delta = 0.15\%$).

$$\left|\frac{y_{i+1} - y_i}{y_i}\right| \leq \delta \tag{2.46}$$

Each flat zone is identified by its edge points plotted in Figure 2-25.

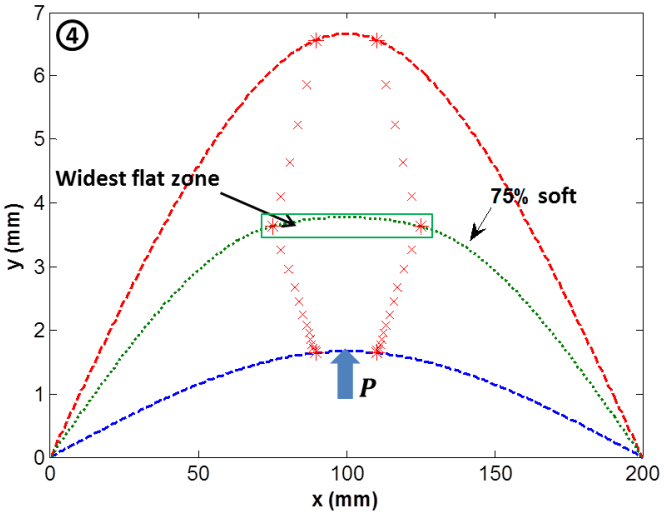

Figure 2-25: Loci of the boundaries of the flat zones

The patterns presented in Figure 2-26 are two additional bi-section morphing strategies (Cases 6 and 7) where the morphing sections are unsymmetrical with respect to the midplane of the structure. This scheme includes two major patterns: in Case 6, soft segments keep their starting locations and propagate through the beam, whereas in Case 7, constant length sections march from left to right (or right to left) in sequential steps.

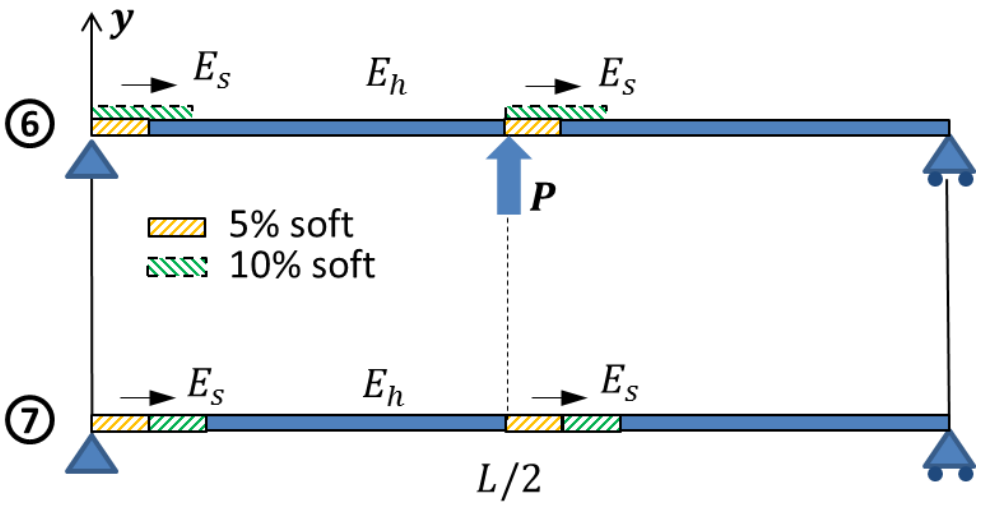

Figure 2-26: Asymmetrical bi-section morph patterns (Cases 6 and 7)

To recall, the produced shapes from Case 1 (as fixed soft segment at the left grew to the right with certain size increments) are shown in Figure 2-27a. Similarly, for Case 6, two soft segments, one fixed at left end and the other in the center, grew from left to right with 5% incremental segment length increase and peak locus of morphed shapes were traced by solid dots. The results are presented in Figure 2-27b. Firstly, similar to its uni-section counterpart (Case 1, Figure 2-27a), the diversion of peak loci is a significant feature in this pattern. Secondly, unlike the first pattern in the uni-section scheme where the peaks were situated on the left side of the actuation force, the loci fall on the right. The central soft segment seems to be

dominating in steering the peak locus. Notice that a mirror pattern would have resulted if the marching went from right to left.

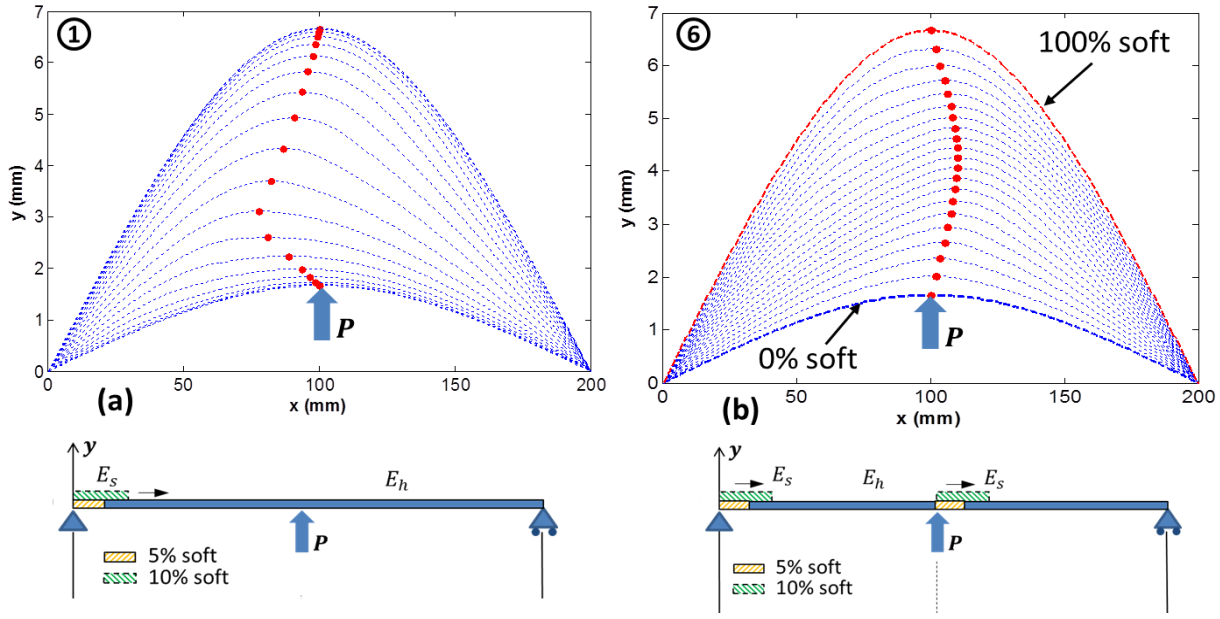

Figure 2-27: Morphed shapes of the beam with highlighted peak points (Case 1 vs. 6)
(a) soft-section pattern; (b) asymmetric bi-section pattern (two soft segments, one fixed at left end and the other in the center, grow sequentially from left to right)

Figure 2-28 shows the peaks of case 7 when two constant-length ($w = 5\%$) segments begin marching from left and move to right in consecutive steps. An intermediate shape with soft segments is shown. At every step, the closer segment to the middle controls the direction of the peak; as such, peaks start from the right side of the midline and gradually move to the left.

Figure 2-29 plots the peak locus for various segment lengths in the marching asymmetric bi-section scheme. For small segments, shapes are more spread out. As the soft region grows, the peaks coincide on the locus of the previous bi-section pattern.

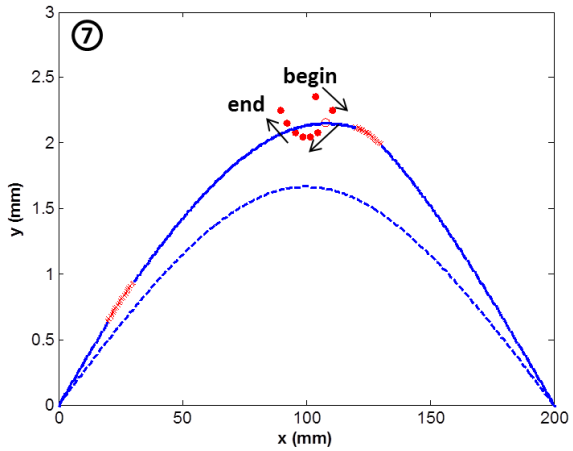

Figure 2-28: Peak locus in a bi-section scheme (Case 7)
Segment length is $w = 5\%$. An intermediate curve with its peak is shown.

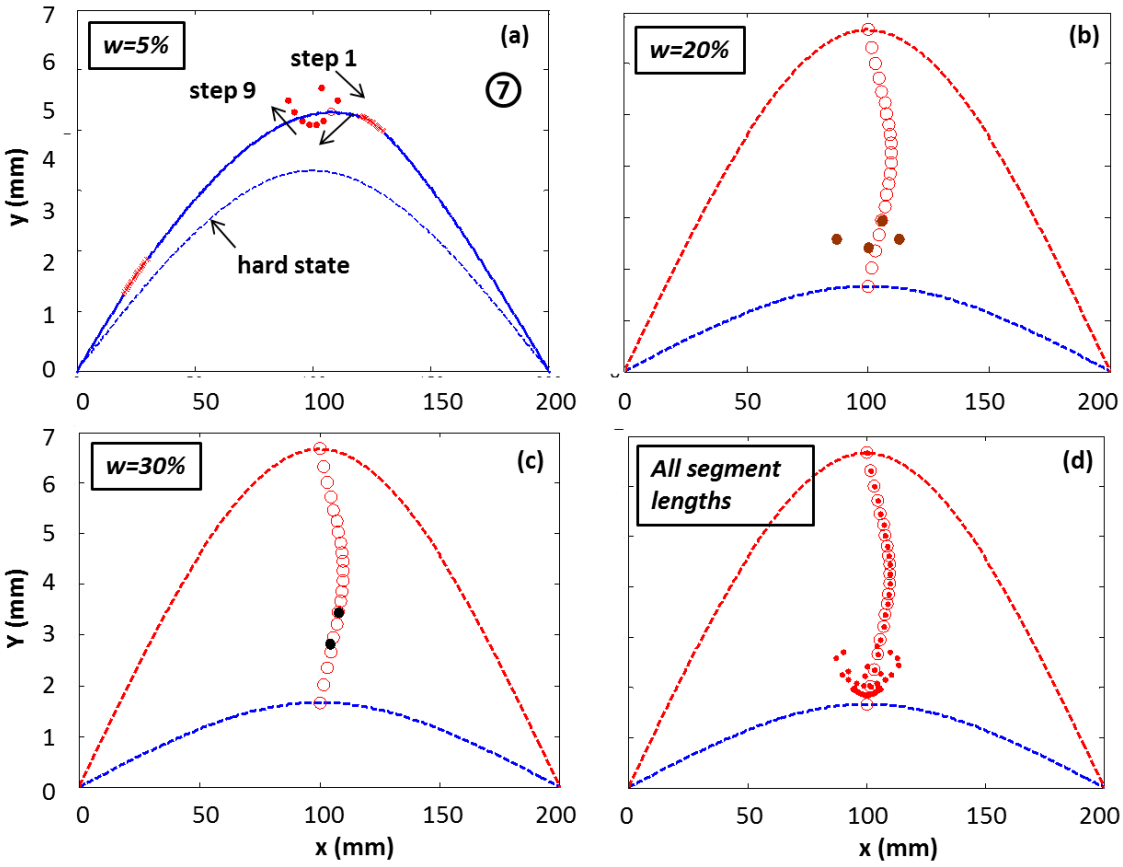

Figure 2-29: Peaks distribution in Case 7 for various segment's length

Summary

Two major morphing patterns (i.e. uni-section and bi-section) have been so far considered. For each pattern, the distribution of the peaks of the morphed shapes was explored and the achievable shape space was determined. Figure 2-30 illustrates the aggregation of results, showing peak distribution with highlighted potential achievable spaces by morphing with different patterns. One could observe that the uni-section morph scheme yields a wider accessible space (22.5% vs. 12% of beam length). Adding the second morphing section would cause an additional degree of flexibility in the opposing direction as the first section which reduces the overall deviation in the morphed structure.

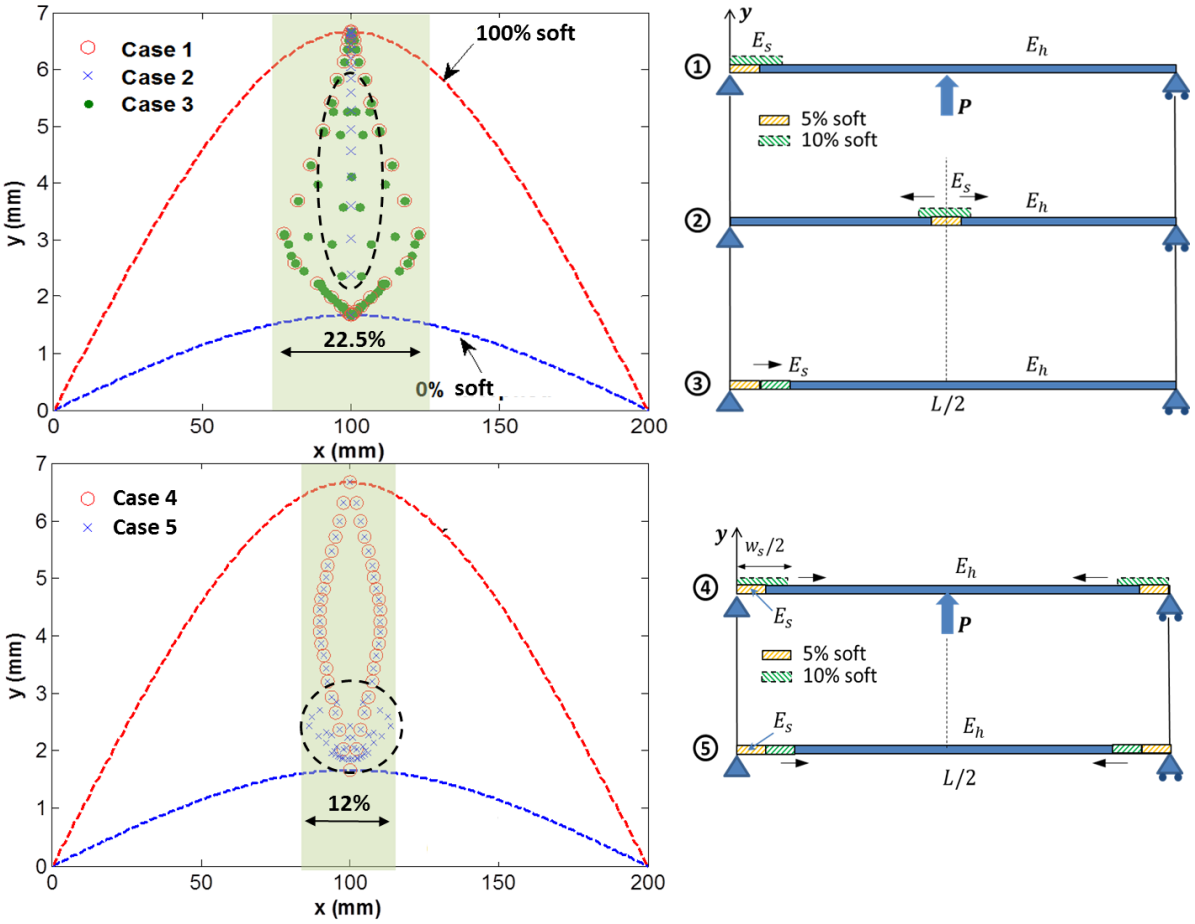

Figure 2-30: Morphing schemes comparison: uni-section (top) and bi-section (bottom)

Secondly, the uni-section morph pattern covers more peak points inside its accessible space. The bi-section scheme can produce shapes with more scattered peaks in lower soft segment lengths, whereas for the larger segment lengths, the locus concentrates on a narrower defined boundary. This could also be related to the middle section which limits the dominating role of the side section in deviating the peaks. The other observation one would notice is on the peak value of the most deviated morphed shape in each morphing scheme. While the uni-section pattern can create well-deviated or top-flat shapes, the bi-section model can produce tall and slim shapes under the same morph parameters. This is due to reduced bending rigidity of the structure by adding transitioned sections.

It is worth noting that introducing a third soft section (and more) will result in shapes whose peaks are enclosed by the uni-section envelope (Figure 2-31) so there is little value in adding additional soft segments for this loading pattern. For other loading patterns, additional soft segments may be helpful.

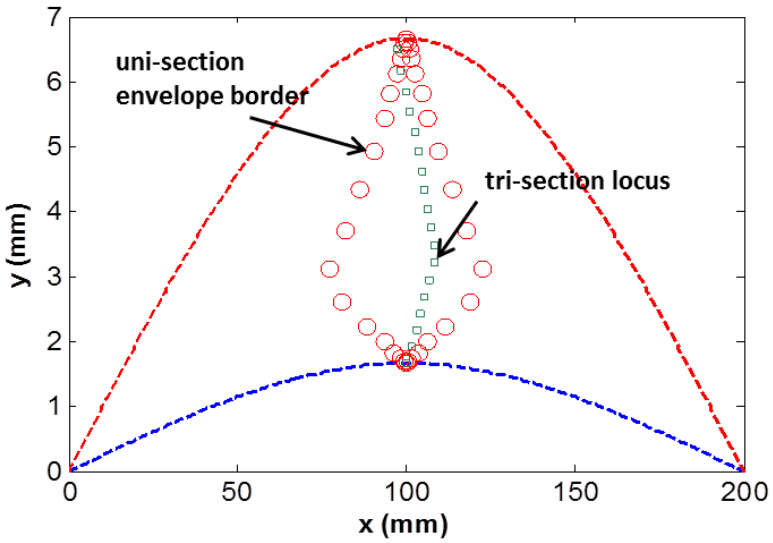

Figure 2-31: Peak locus in a tri-section spreading scheme

2.6.3 Boundary characterization

As noticed in Figure 2-30, the extent of the deviated shapes is prescribed by the first pattern of the uni-section morphing scheme. For this pattern, there is a particular segment length that results in the most asymmetric shape whose peak defines the *edge* of the morph boundary. The significance of this length is investigated in this section.

The closed form solution for case 1 could be summarized as:

$$\begin{bmatrix} E_s^{-1} & -E_h^{-1} & 0 & 0 \\ x_2E_s^{-1} & -x_2E_h^{-1} & E_s^{-1} & -E_h^{-1} \\ 0 & 0 & 1 & 0 \\ 0 & L & 0 & 1 \end{bmatrix} \begin{bmatrix} \boldsymbol{c_1^1} \\ \boldsymbol{c_1^2} \\ \boldsymbol{c_2^1} \\ \boldsymbol{c_2^2} \end{bmatrix} = \begin{Bmatrix} Af(x_2) \\ Ag(x_2) \\ 0 \\ -g(L) \end{Bmatrix} \tag{2.47}$$

Solving for the coefficients c_1^1 and c_1^2 will result in:

$$c_1^1 = \frac{A[g(x_2) - x_2f(x_2) + Lf(x_2)] - E_h^{-1}g(L)}{LE_s^{-1}} \tag{2.48}$$

$$c_1^2 = \frac{A[g(x_2) - x_2f(x_2)] - E_h^{-1}g(L)}{LE_h^{-1}}$$

where functions $f(x_2)$ and $g(x_2)$ are previously defined as:

$$f(x) = -\frac{Pb}{2L}x^2 \tag{2.49}$$

$$g(x) = -\frac{Pb}{6L}x^3$$

Recall L is the total length and b is the force distance from the right support. Recall that the shape of the beam is described by two piecewise functions,

i.e. $y = H_1 y_1 + H_2 y_2$

where

$$y_1(x) = \frac{1}{E_s I}[g(x) + c_1^1 x] \tag{2.50}$$

$$y_2(x) = \frac{1}{E_h I}[g(x) + c_1^2 x + c_2^2]$$

Let x_2 be the length-normalized coordinate measured from the left support and x_2^p be the location of the peak. Solving for x_2^p from each of two shape functions y_1 and y_2 results in:

$$x_2^p = \frac{2L}{Pb}\boldsymbol{c_1^1}$$
$$x_2^p = \frac{2L}{Pb}\boldsymbol{c_1^2} \tag{2.51}$$

For this model with specification introduced in Table 2-2, if one plots the variation of x_2^p in terms of the coefficients c_1^1 and c_1^2 defined in Eq. 2.248, Figure 2-32 is obtained. Compatibility of the peak location is only satisfied in the intersection of the plots where the segment length is 37.5% of the beam length. This can be graphically verified in Figure 2-20 by approximating the segment length corresponding to the most asymmetric shape. Assuming small deformations, the value of x_2^p also represents the extent of the achievable space from the mid plane.

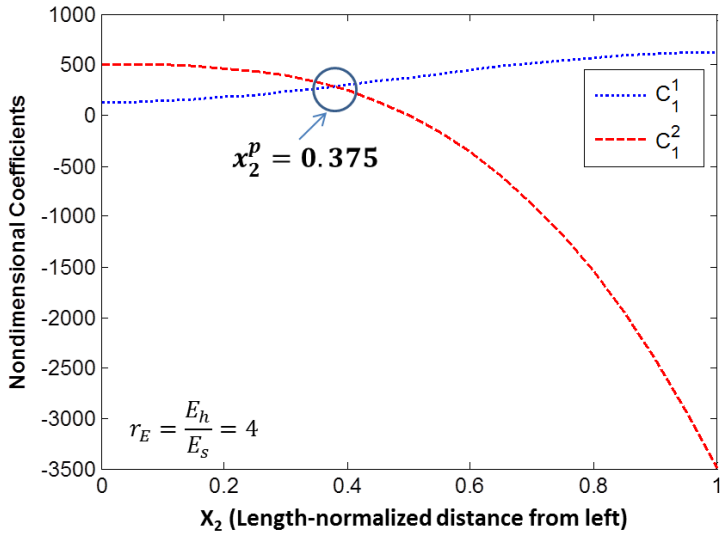

Figure 2-32: Variation of the shape coefficients in terms of longitudinal coordinate

Effect of model parameters on boundary edge: According to Eq. 2.52, location of the boundary edge is a function of the beam geometry, actuation and the two (upper and lower) moduli. Figure 2-33 shows the coefficient curves in the vicinity of their intersection (similar to those in Figure 2-32) for different hard-to-soft modulus ratio ($r = E_h/E_s$). For the same set of actuation force and beam geometry, the boundary edge expands to the sides as the lower modulus decreases. Another significant observation is regarding the vertical beam displacement: notice (in Figure 2-33) that the value of nondimensional coefficients (c_1^1 and c_1^2) increase with modulus ratio. These coefficients were directly used in Eq. 2.51 to calculate the vertical beam displacement. This means that one can expand the morph space's horizontal and vertical bounds by selecting larger hard-to-soft modulus ratio.

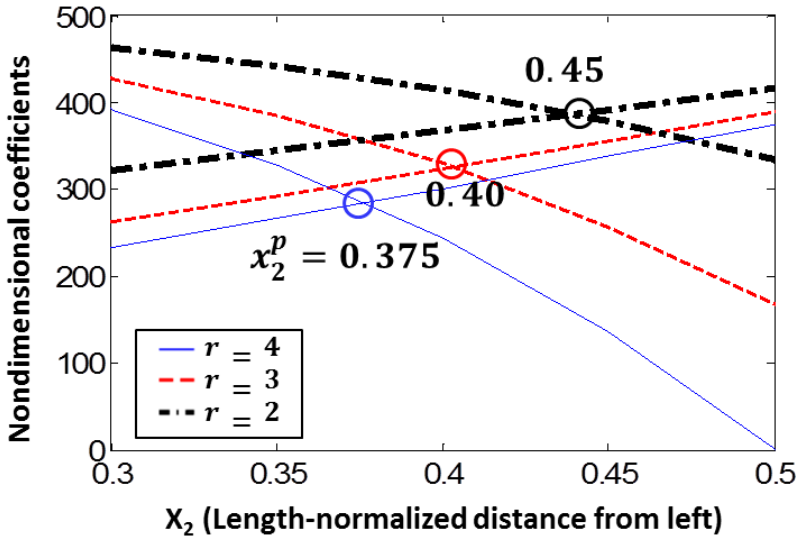

Figure 2-33: Effect of hard-to-soft modulus ratio on the boundary extent (intersection point)

Figure 2-34 displays the effect of actuation force. Unlike modulus, increasing the force does not change the extent of the morph space in lateral (side) direction; however, it increases the vertical boundaries of the achievable shapes. This can also be explained by observing the coefficients' trend and realizing their direct contribution in the vertical deformation.

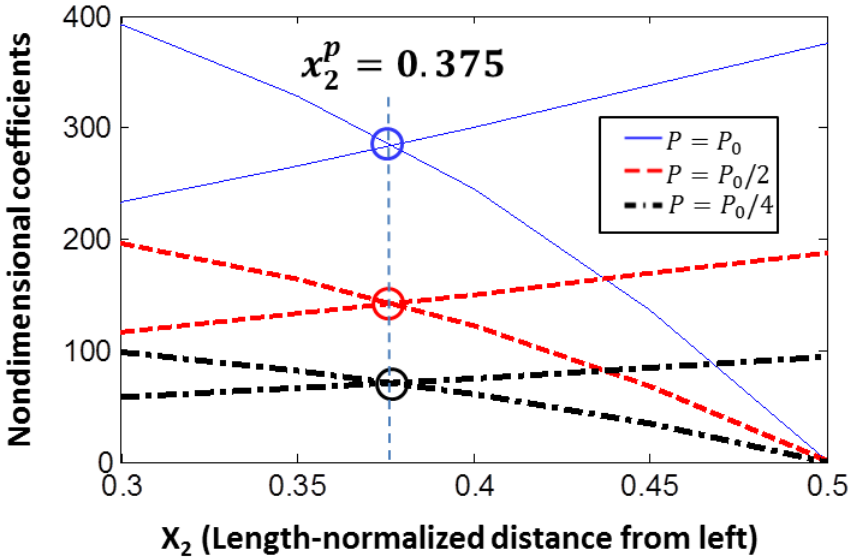

Figure 2-34: Effect of actuation force on the boundary edge

Figure 2-35 presents variation of the side boundary for different beam lengths. The margins of the morphed shapes do not vary with beam length. For similar load and moduli, the margin remains at 37.5% of the length. Moreover, one may expect to see higher vertical displacements in a larger-span beam.

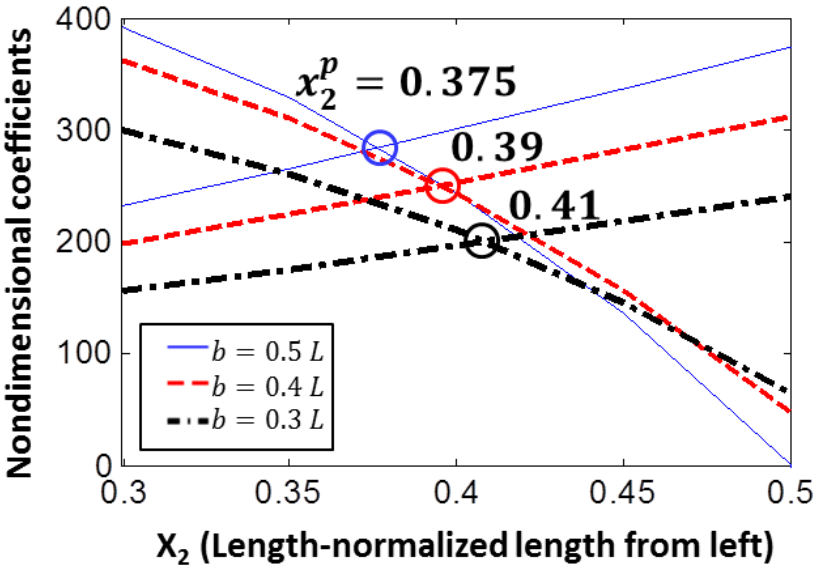

Figure 2-35: Effect of beam length on the boundary edge

Figure 2-36 shows the effect of force location on the side limit. Recall that b is the distance of the actuator to the right support. As the force moves towards the right, the morph space shifts in the same direction, as expected. By observing the coefficients plot, one could verify that as the force moves off the centerline, the vertical extent of the morphed shapes would reduce.

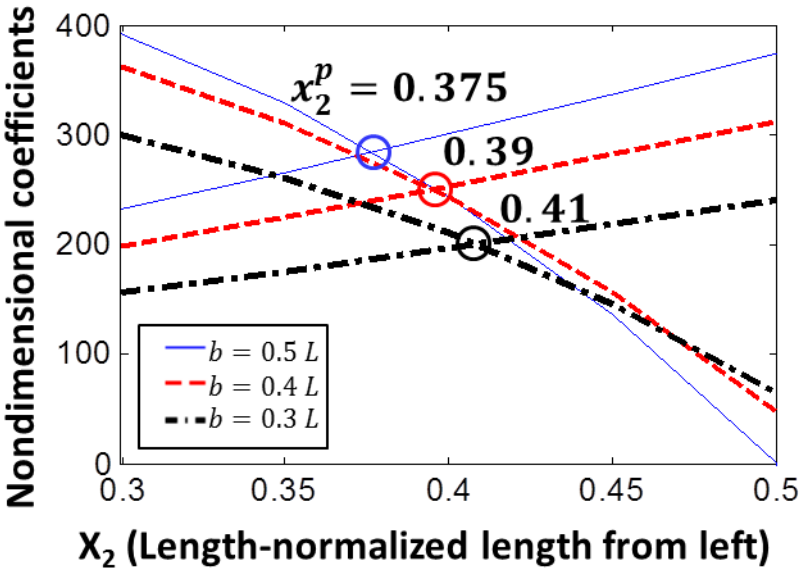

Figure 2-36: Effect of force location on the side boundary edge

2.6.4 Stability study of the morphed shapes

It was shown in Section 2.5 that the stress in the deformed beam is proportional to the curvature of the morphed shape at that section. In a morphing process where diverse shapes with different curvatures are resulted, it is essential to ensure that all the intermediate shapes are elastically stable. This section studies the stability of the resulted morphed shapes.

Consider an example curve from a uni-section pattern with 40% segment length (Figure 2-37a). Red dots indicate the peak points. The corresponding curvature profile of the morphed beam is illustrated in Figure 2-37b.

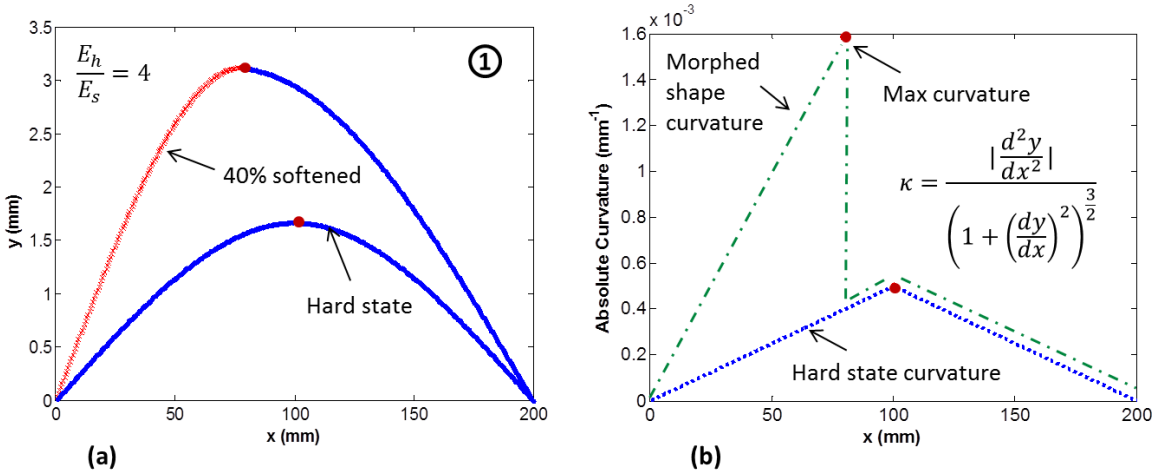

Figure 2-37: (a) An intermediate morphed shape; (b) the corresponding curvature

The transition point shown on the curvature plot has a particular significance. Consider the first and second derivative plots individually as presented in Figure 2-38.

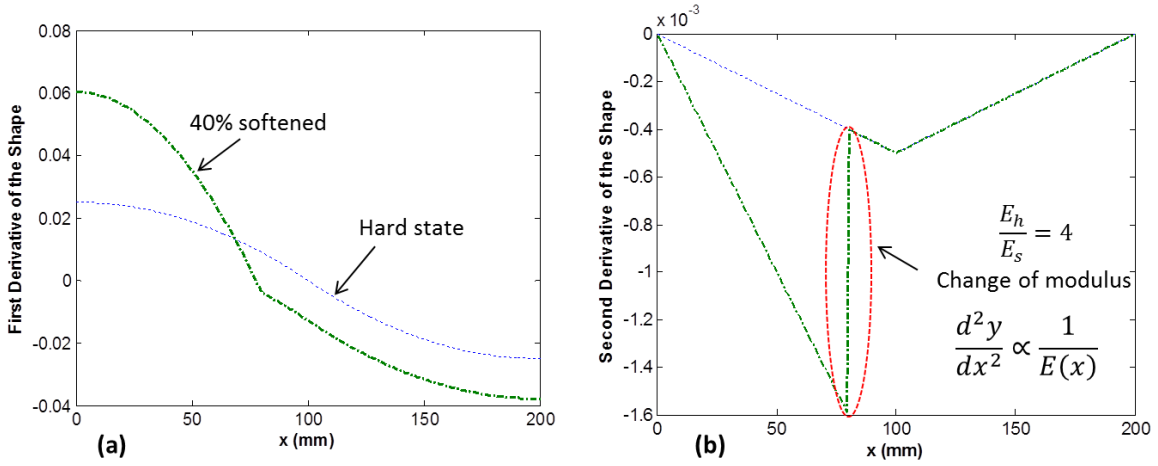

Figure 2-38: (a) First derivative; (b) second derivative of the morphed shape

Notice the abrupt change in the second derivative plot that occurs at 40% of the beam length. This is where the modulus changes from a low to a higher value. Since the moment distribution is constant and independent of the material state, the constitutive elastic equation of the beam (Eq. 2.11) describes an inverse relationship between the second derivative and the modulus.

Looking at the transition point on the curvature plot (Figure 2-37), as the beam transforms from soft to hard state, a drop-off in the curvature is observed.

Figure 2-39 displays the maximum curvature distribution of the shapes for case 1 scheme with softening progression of 0 to 100% (dashed arrows). Note that the maximum curvature magnitude of the intermediate curves are less than the one in the soft state, which, due to direct relationships of curvature and stress, implies the maximum stress is lower than the one in the soft state and the morphed shapes are elastically stable.

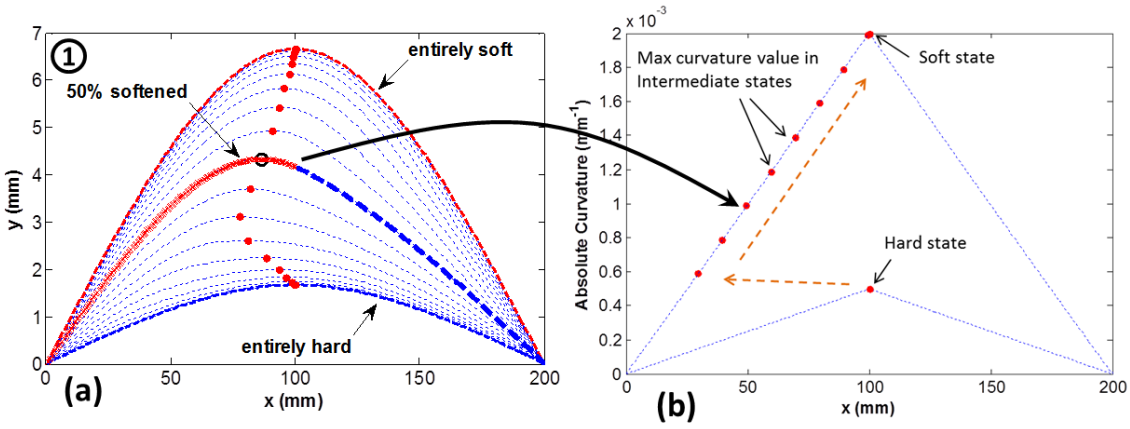

Figure 2-39: (a) A family of morphed shapes in pattern 1; (b) maximum curvature values in different morph states are all lower than that of completely soft state case.

Similarly, the maximum curvature distributions of the morphed shapes generated from all the uni-section patterns were studied. It was observed that their maximum curvature is within the secure region (see Figure 2-40 for Case 3).

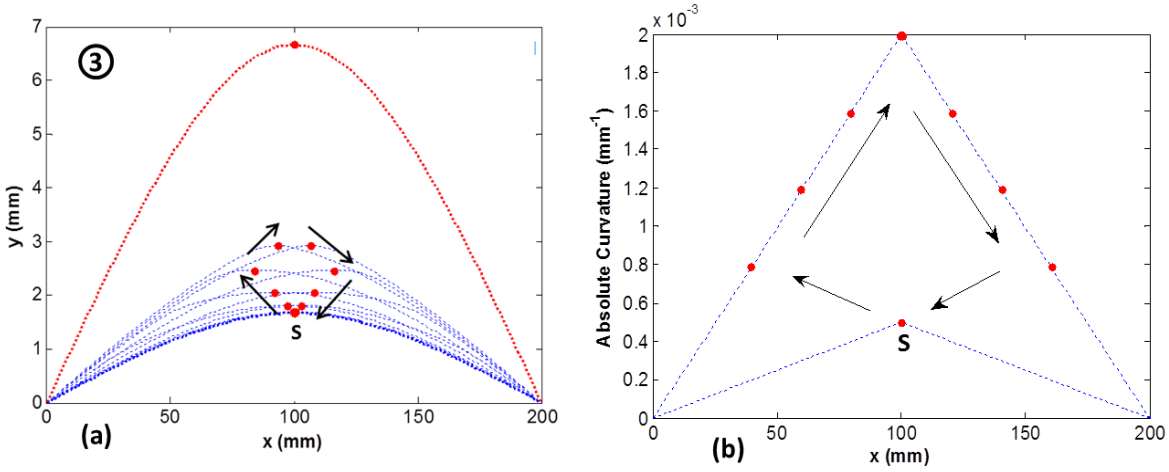

Figure 2-40: Maximum curvature of the morphed shape (symmetric Case 3)

Figure 2-41 shows an intermediate (segment length of 25%) morphed shape with the corresponding curvature distribution plot. Similarly, for all other segment lengths, the maximum curvature values fall on the soft beam. This implies that the structure is statically stable.

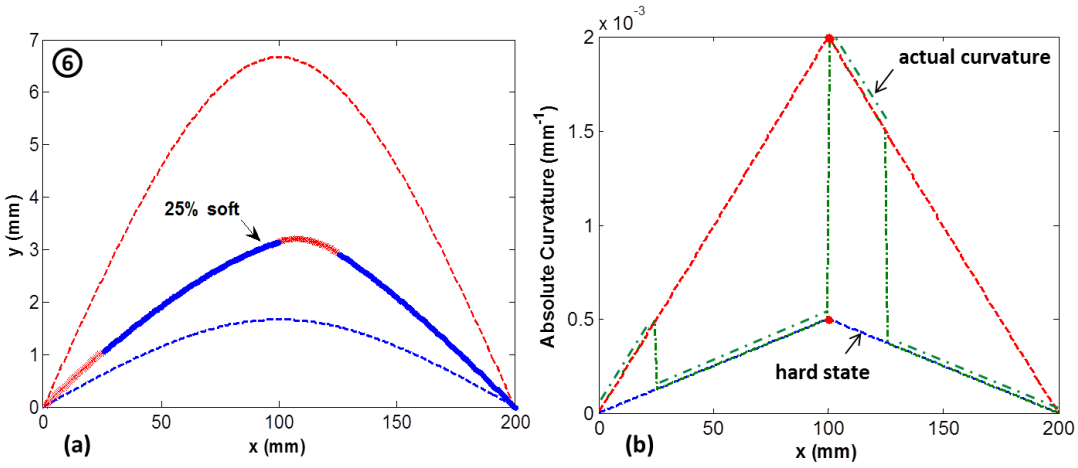

Figure 2-41: (a) An intermediate morphed shape in asymmetric Case 6; (b) curvature plot

To understand the structural stability of the morphed shapes, consider an intermediate step in the curves with 10% segment length (Figure 2-42a). The corresponding curvature profile with its highlighted maximum value is shown on the right. Figure 2-42c represents the peak locus of all

the morphed shapes with possible segment lengths. The maximum curvature values confirm the structural stability of the morphed shapes.

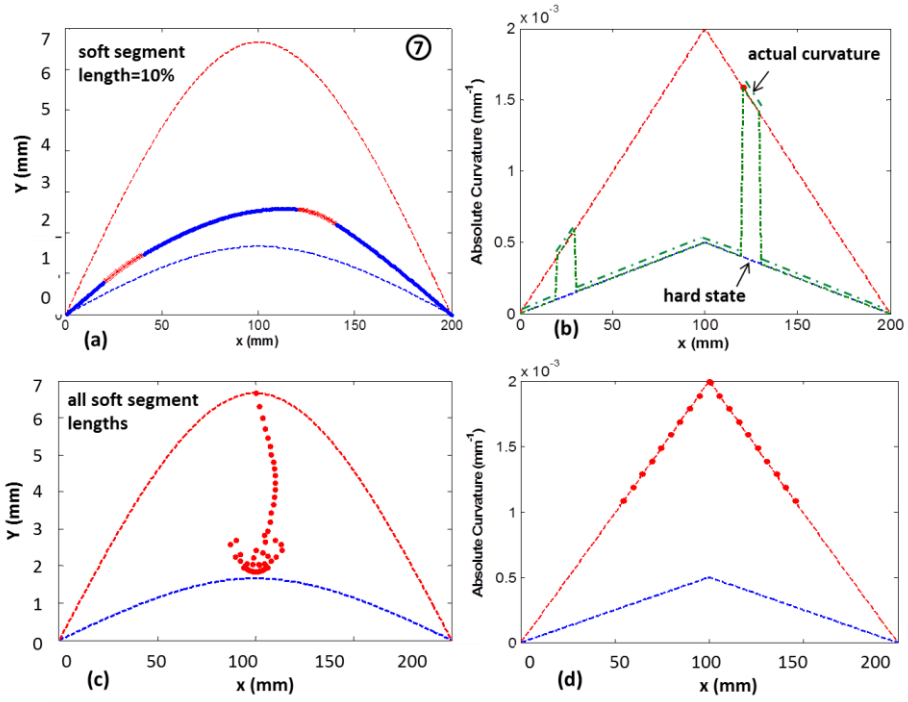

Figure 2-42: (a) morphed shape in the asymmetric Case7.
(b) curvature plot with maximum value; (c) peak locus for all soft lengths; (d) maximum curvature points

3.0 INVERSE SHAPE MORPHING

The previous chapter illustrated forward shape morphing of a supported beam. It was shown that, with local softening in the structure, a larger morph space can be achieved without moving or changing the force. Yet, a challenging question is that, if one wants to create a specific shape, how the morphing should be performed. In this chapter, the problem of inverse shape morphing of the structure with variable stiffness has been investigated.

Generally, inverse morphing is finding the set of softening regions and actuation forces that produce a desired shape. For each soft region, a *segment length* (normalized by total length) is determined. The problem complexity is determined by the variability of the softening and actuation sets. A target shape is either defined explicitly or drawn using a computer aided design (CAD) program. CAD shapes are normally drawn as B-spline curves. In order to convert them into the explicit form, the theory of B-spline curves has been explored and conversion algorithms are developed. The proper optimization approach is selected based on the convexity of the objective function. The inverse problem is analytically characterized and numerical methods are used to validate the results of the optimization routine.

3.1 STATEMENT OF THE PROBLEM

Consider a simply supported beam with discrete finite regions of transformed (soft) material (Figure 3-1). Let x_s^k be the center point of the k^{th} soft segment measured from the left support whose length is represented by w_s^k ($0 \leq x_s^k, w_s^1 \leq L$). P is the actuated force at the distance x_a ($0 \leq x_a \leq L$). It is assumed that the maximum possible numbers of soft regions (N_s) is known.

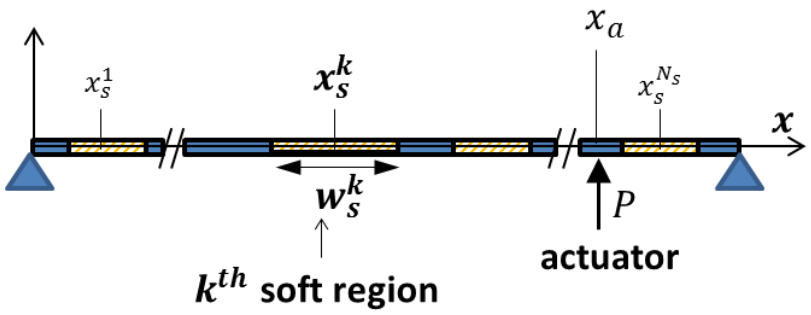

Figure 3-1: Simply supported beam model subjected to morphing

The shape of the morphed beam is prescribed by conditions of the soft regions and the actuation force, i.e. $y_m = y(x_s^k, w_s^k, x_a, P)$. The objective is to find the optimized segments' length and actuation conditions in order to minimize the root-mean-square shape error (E_{RMS}) between the morphed shape, y_m and the target shape, y_t (Eq. 3.1). Geometrical constraints impose that the two extreme regions need to lay within the domain (Eq. 3.2) and the adjacent soft segments are not allowed to overlap (Eq. 3.3).

This optimization problem could be summarized in the following form:

$$\min J = E_{RMS}\{y(x_s^k, w_s^k, x_a, P), y_t\} \qquad k = 1,2,\dots,N_s \tag{3.1}$$

$$\begin{cases} x_s^1 - \dfrac{w_s^1}{2} \geq 0 \\ x_s^{N_s} + \dfrac{w_s^{N_s}}{2} \leq L \end{cases} \tag{3.2}$$

$$x_s^k + \frac{w_s^k}{2} \leq x_s^{k+1} - \frac{w_s^{k+1}}{2} \tag{3.3}$$

$$|P_Y^s| \leq |P| \leq |P_Y^h| \tag{3.4}$$

The error objective function introduced in Eq. (3.1) is found by the difference in vertical coordinate locations and can be expressed in a more explicit form (Eq. 3.5), where n is the number of nodes.

$$E_{rms}^2 = (y_m - y_t)^2 \tag{3.5}$$

Performance index convexity (numerical investigation)

The convexity of the defined performance index was numerically investigated. Consider the beam subjected to three actuations where a *uni-section* morphing scheme is applied (Figure 3-2). This scheme is just a specifically defined softening pattern where the soft segment is constrained on the left support while its length grows.

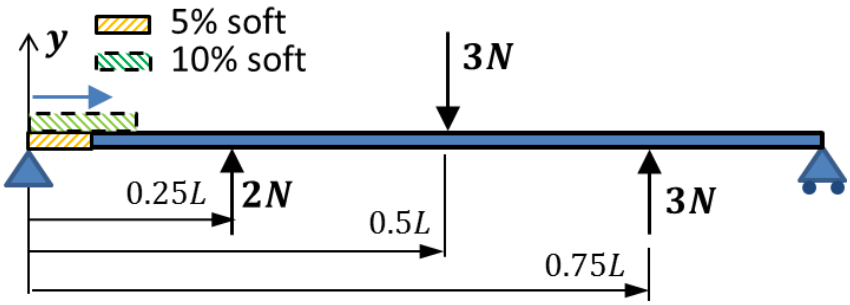

Figure 3-2: Morphing beam with multiple loading

Figure 3-3 shows the shape of the morphed beam for various soft-segment lengths. The shapes are obtained using numerical FE methods. Squared numbers represent different states and in general as the number increases so does the soft-segment length. As expected, as the soft segment grows, the beam assumes different shapes for the same fixed-location/magnitude force conditions. Some are closer to the target shape than others.

In this example, the performance index for a given morphed condition is defined by Eq. (3.1) which is a least mean square of the separation of the achieved shape from the target shape. The performance index is plotted as a function of percent segment length in Figure 3-4. The performance index is non-convex, as it has a local minimum in the second illustrated morphing condition where the global minimum occurs under the fourth morphing condition. Due to non-convexity, we chose a Genetic Algorithm (GA) integrated with MATLAB® optimization toolbox as the primary non-gradient based optimization routine in this work.

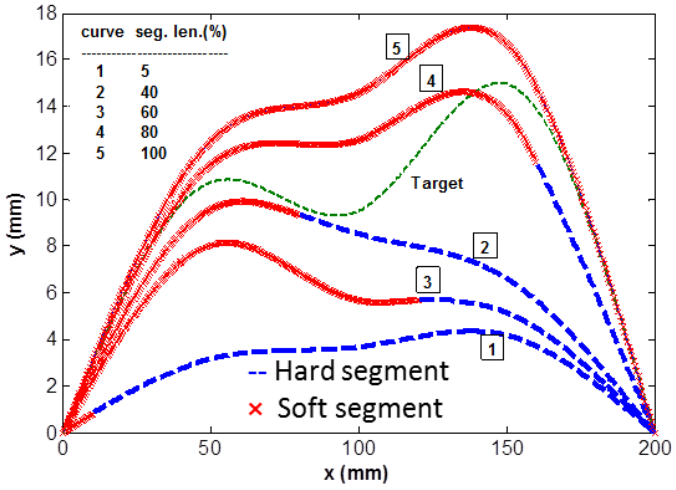

Figure 3-3: Shape of the morphed beam with various soft segment lengths

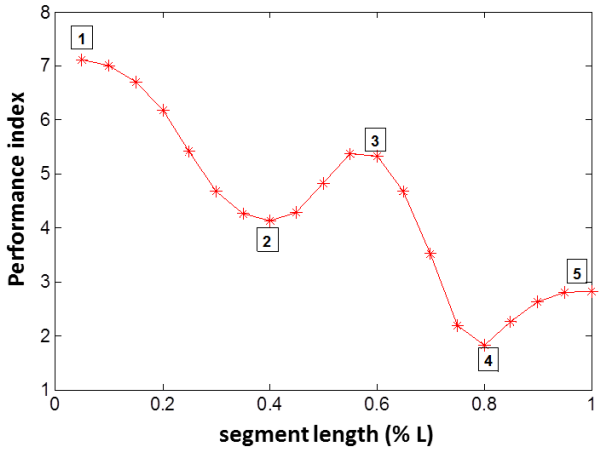

Figure 3-4: Performance index value vs. soft segment lengths

3.2 SOLVING OPTIMIZATION PROBLEM USING GENETIC ALGORITHM (GA)

GA is a robust optimization technique that can be used for a variety of optimization problems not well suited for standard optimization algorithms, e.g. problems with discontinuous, non-convex (such as this work) or highly nonlinear. In the algorithm, a random *initial population* is created. Each member is scored by its performance index and higher index members are chosen as *parents* who can generate *children* for next generation by using different rules such as random change in a single parent (*mutation*) or combining a pair (*cross-over*). Individuals with the best performance index (*elites*) automatically survive to the next generation. Optimization progresses by replacing the current population with the children. The stopping criteria may be maximum number of generations, time limit or meeting a defined tolerance of the performance index (See Appendix A for more details on GA).

GA parameters selection

To obtain more reliable and faster optimization results, it is necessary to determine reasonable GA parameters. Some of these important parameters include initial range, reproduction variables (elite count and crossover fraction) and effect of using a hybrid (combined) function which are listed in Table 3-1. In order to approximate the values, an arbitrary uni-section softening pattern was first assumed where the segment was not fixed to the ends ($x_s = 0.68; w_s = 0.3$) and a constant load ($P = P_Y^S$) was applied in the middle. By solving this forward problem, the morphed shape was determined and set as desired shape. For different sets of GA parameters, the inverse optimization problem was then solved and the standard error between the optimized and target values was evaluated. The values of the set that reported the minimum error (i.e. shaded set 4) were chosen for the rest of the work. For a better convergence, GA was hybridized with constrained nonlinear interior-point method.

Table 3-1: Different parameter sets used by GA in inverse problem.
The average result columns show the optimized center and length of the segment. The optimal results are compared to the actual defined values (0.68, 0.3) and shaded row values are selected based on the minimum standard error.

Set No.	Initial range (1)	Elite count (2)	Crossover fraction (3)	Hybrid function	Average Results		Standard error	
1	[0;1]	2	0.8	None	0.670	0.340	0.017	0.036
2	[0;5]	2	0.8	None	0.672	0.261	0.012	0.011
3	[0;5]	2	0.7	None	0.690	0.270	0.005	0.014
4	[0;5]	2	0.6	fmincon (4)	0.684	0.292	0.010	0.009
5	[0;10]	2	0.4	fmincon	0.694	0.270	0.009	0.011

(1) Range of the vectors in the initial population
(2) Number of individuals guaranteed to survive to the next generation
(3) Fraction of the next generation (excl. elite children) produced by crossover rule
(4) Constrained nonlinear multivariable function for minimization

3.3 SINGLE ACTUATION INVERSE MORPHING

3.3.1 Introducing the problem

In this section, the general study being conducted involves finding the set of softening regions and actuation forces that produce a desired shape. For each soft region, *segment center* (x_s) and *segment length* (w_s) (both normalized by beam length) are determined. The initial assumption is to use a uni-section scheme where only one segment, which can be arbitrary placed, is softened.

It should be noted that all the developed methods and algorithms in this study are general for a supported beam; however to present numerical results, some specific parameters were selected. Table 3-2 shows the specifications of the simulated beam model.

Table 3-2: Specifications of the simulated beam model

Variable	Description	Value	Unit
Geometrical Properties			
L	Beam Length	200	mm
W	Width of rectangular section	10	mm
H	Height of rectangular section	2	mm
Material Properties			
E_h	Hard phase modulus	3000	MPa
E_s	Soft phase modulus	750	MPa
ν_h, ν_s	Poisson's ratio (hard&soft phase)	0.3	–

The studied target shape is a B-spline curve skewed to the right and displayed in Figure 3-5. B-spline curves are comprehensively covered in Appendix B.

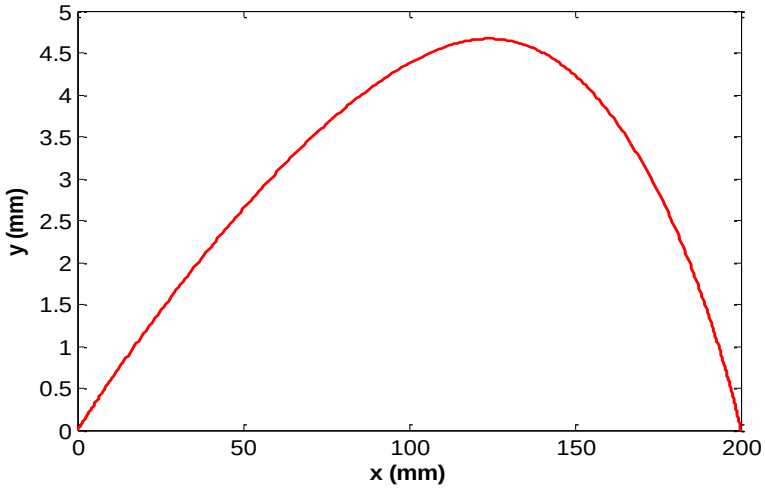

Figure 3-5: Target B-spline curve for studied inverse morphing problem

Case studies: Depending on the variability of the actuation force, P, and its location, a, the inverse problem could be divided into four categories shown in Table 3-3, including Case 1: constant force location and constant magnitude; Case 2: constant force location and variable magnitude; Case 3: variable for location and constant magnitude; and Case 4: variable force location and magnitude. Each case and its results are presented below.

Table 3-3: Various conditions in a single actuation morphing problem

	Constant P	Variable P
Constant a	Case 1	Case 2
Variable a	Case 3	Case 4

3.3.2 Results and discussions

Case 1: This is a case where a constant actuation force is exerted in a given location. From a conservative standpoint, force was chosen to be $P = P_Y^s = 0.25P_Y^h$. Let the actuator be located at

the mid span ($a = 0.5L$). The objective in this case is to find the optimal soft segment ($N_s = 1$)) defined by its center point (x_s) and length (w_s).

Figure 3-6 illustrates the shape improvement as the optimization algorithm proceeds. The performance index (shape error, J) is shown for each case. The optimal values (case *d*) were found to be $x_s^* = 0.73,\ w_s^* = 0.54$ with the superscript '*' representing the optimized value. Note that to minimize the shape error, the soft region's center moves to the right while its length increases. Also recall that the applied force is in the center of the beam for all cases.

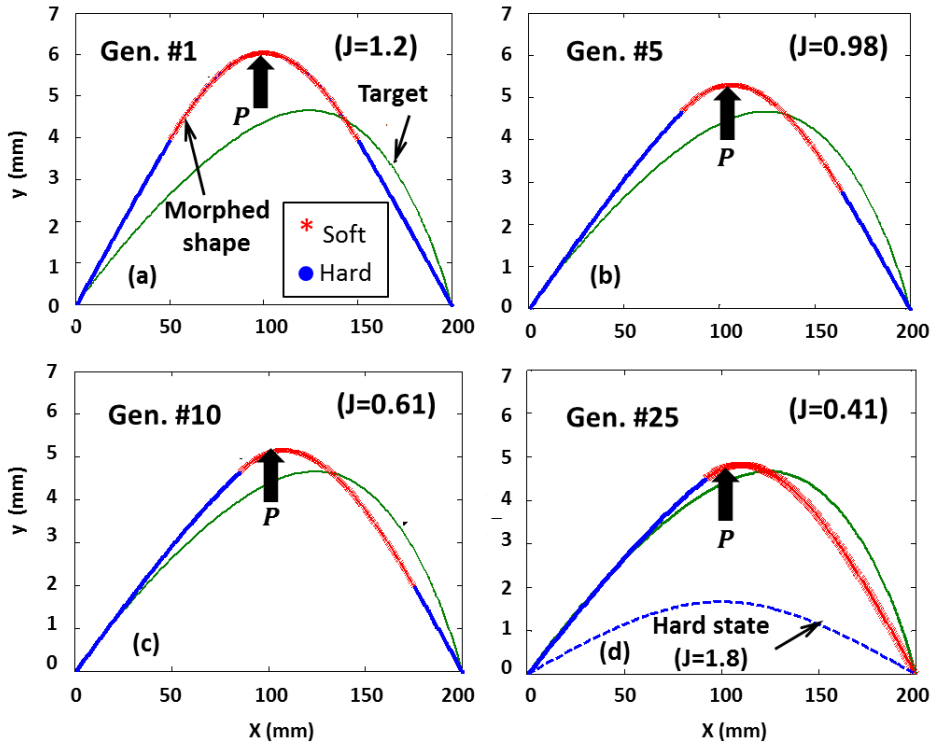

Figure 3-6: Shape improvement over generations
The numbers in the parentheses represent the performance index. The solution converged after 25 generations. The index for the hard state in the final solution is also shown. For all cases $\boldsymbol{P = P_Y^s = 0.2N}$

It is worthwhile to mention that the optimization procedure was repeated with multi-section morph schemes (set $1 < N_s \leq 3$ in simulation); however the results indicated that adding a second (or higher) soft segment did not significantly improve the morph due to very small

reported lengths for the subsequent segments. (for example for $N_s = 2$: $x_s^* = [0.44 \;\; 0.72]$, $w_s^* = [0.05 \;\; 0.53]$, $J = 0.40$), meaning that the added soft segment has width of only 5% of the beam length and marginal improvement in *J*).

***Case 2*:** Now, consider the case where the actuation force is no longer restrained to have a constant magnitude. Let $P_Y^s \leq P \leq P_Y^h$ and $a = 0.5L$. The optimization algorithm successfully determined the optimal softening values as well as actuation magnitude: $x_s^* = 0.79$; $w_s^* = 0.31$; $P^* = 0.43\, P_Y^h$ (J = 0.25). Figure 3-7 illustrates the morphed beam under these conditions. It is notable that the increased actuation force as compared to that used in Case 1 was compensated with reduced segment length, although the center point of the soft segment remained unchanged. Notice that the hard beam shape under the same force magnitude and location and its corresponding performance index is also shown. One can appreciate the worthiness of modulus variation in shape morphing with fixed position actuators.

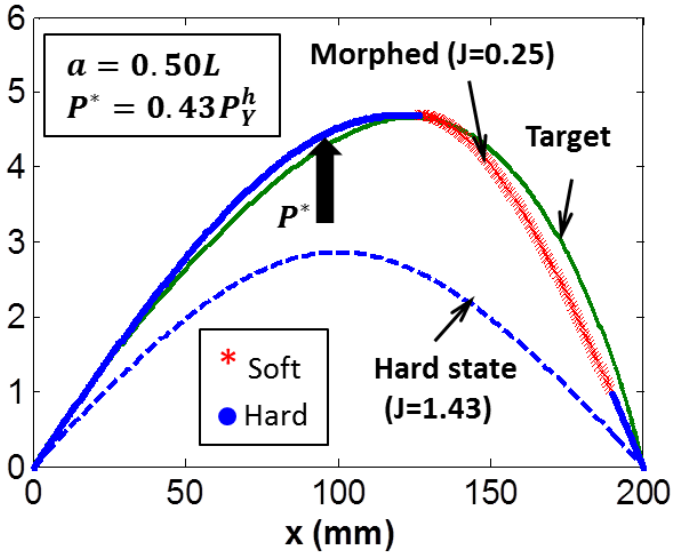

Figure 3-7: Morphing with variable force in the middle.
The performance index value for the morphed shape is shown. Dashed curve represents the deformed hard beam with same boundary conditions

***Case 3*:** In this case, the constraint on the actuation point was partially relieved and the single actuator was allowed to be selected from discrete known positions along the beam ($a \in [0.25 \;\; 0.5 \;\; 0.75] \times L$). The single force remained constant ($P = 0.25P_Y^h$). For this case, the optimization routine was modified to accommodate multiple actuator positions and to choose the best actuator location from among that set. For this case the optimal values were reported to be: $a^* = 0.75L;\ x_s^* = 0.6;\ w_s^* = 0.79;\ (J = 0.35)$. For comparison purposes, the best parameters for each actuator placement, its associated performance and the performance index resulted from applying the same actuation condition to the hard state are presented in Table 3-4. It is notable that local stiffness reduction has substantially improved the target shape approximation.

Table 3-4: Morphing parameters in constant force in different actuation points (optimal case is shaded)

Actuation point ($\times \boldsymbol{L^{-1}}$)	**Segment center** ($\times \boldsymbol{L^{-1}}$)	**Segment length** ($\times \boldsymbol{L^{-1}}$)	**Performance index** ($\boldsymbol{J}$)	**Index at hard state** ($\boldsymbol{J_h}$)
0.25	0.6	0.78	0.84	2.55
0.5	0.73	0.54	0.41	2.21
0.75	0.6	0.77	**0.35**	2.52

Figure 3-8 displays the optimal morphed shapes as the force is positioned in three designated points. The shape of the beam in the hard state is also plotted for each load position. When the actuator is in the far left position ($a = 0.25L$), the material transforms to a large extent ($w_s = 0.84\%$). This allows the structure to move upward with its peak slightly to the right. However, due to the opposite locations of the actuator and target shape inclination, softening could not effectively morph the beam to the target. As the actuator moves to the middle ($a = 0.5L$), the force drives the middle apex upward. The actuation displaces the peak high enough where only

54% softening is necessary to divert the apex to the right in the vicinity of the target. In the third actuation placement ($a = 0.75L$), similar to the first case, the softening is aimed to transfer the peak in vertical as well as lateral direction. Therefore, more material transformation, compared to previous case, is required. Since the target curve is inclined to the right half, the latter actuation point yields to the best morphed shape.

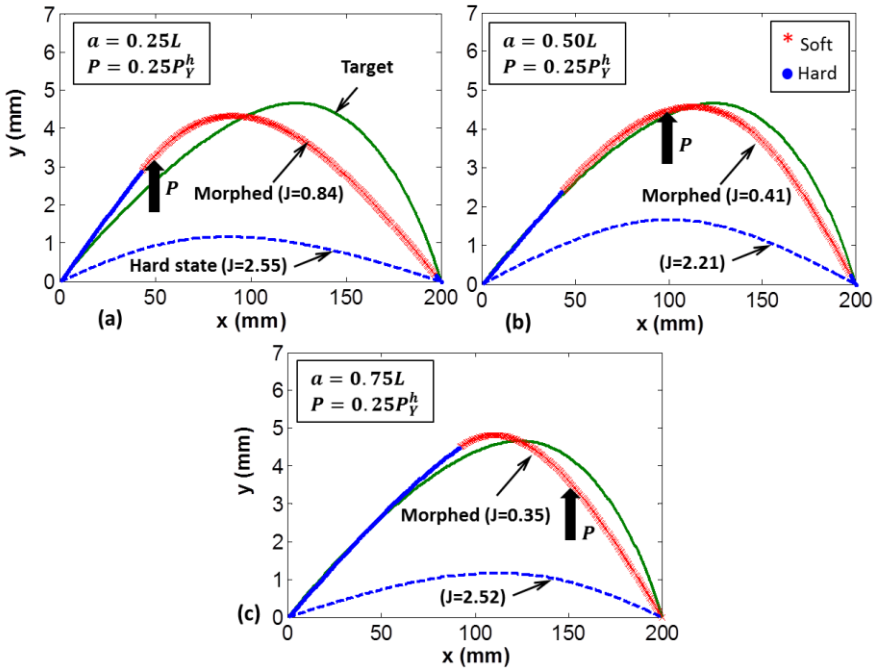

Figure 3-8: Morphing with constant force applied at three different locations. Deformed hard beam under same boundary condition is also shown. Indexes are shown in parentheses.

Case 4: This is the generalized case where the force location and magnitude were allowed to change within the previously prescribed limits (i.e. $a \in [0.25 \quad 0.5 \quad 0.75] \times L$ and $P_Y^S \leq P \leq P_Y^h$). The optimization routine, in its most comprehensive form, determined the optimal values to be $a^* = 0.75L$, $x_s^* = 0.87$, $w_s^* = 0.20$, $P^* = 0.73\, P_Y^h$ (J = 0.07). Similarly, from a comparison perspective, the optimal values for each force location are listed in Table 3-5.

Table 3-5: Optimal morphing parameters for each actuation point (optimal case is shaded)

Actuation point ($\times L^{-1}$)	**Actuation force** ($\times 1/P_Y^h$)	**Segment center** ($\times L^{-1}$)	**Segment length** ($\times L^{-1}$)	**Performance index** (J)	**Index at hard state** (J_h)
0.25	0.44	0.78	0.42	0.44	1.98
0.5	0.43	0.79	0.31	0.25	1.43
0.75	0.73	0.87	0.20	**0.07**	0.98

Figure 3-9 presents the morphed shapes in the three actuation positions. In the first location ($a = 0.25L$), while the structural displacement increases compared to that of the hard state due to reduced stiffness, the soft segment center on the right half of the beam causes the peak of the morphed curve to incline to the right to minimize the shape error. However, as discussed before, the actuator placement was found to be ineffective. In the middle-actuation case ($a = 0.5L$), the peak in the completely stiff beam is already closer to the target's apex, therefore smaller stiffness change (compared to the left actuation case) must be contributed to move the beam vertically. , This is observed by comparing the two segment lengths. The center of the soft segment is still on the right half side to steer the peak towards the target. While the optimal actuation force, compared to the first position, remains unchanged, the shape error is decreased. As the actuator locates toward the right end of the beam ($a = 0.75L$), softening parameters are significantly improved. The larger force, as opposed to two previous cases, is due to the off-center position of the actuator which demands additional energy to move the structure in the vertical direction. The larger actuation value is then compensated by the reduced segment length which primarily guides the beam in the lateral direction towards the target. The shape morphing with the latter parameters is the most accurate among all the previously studied cases.

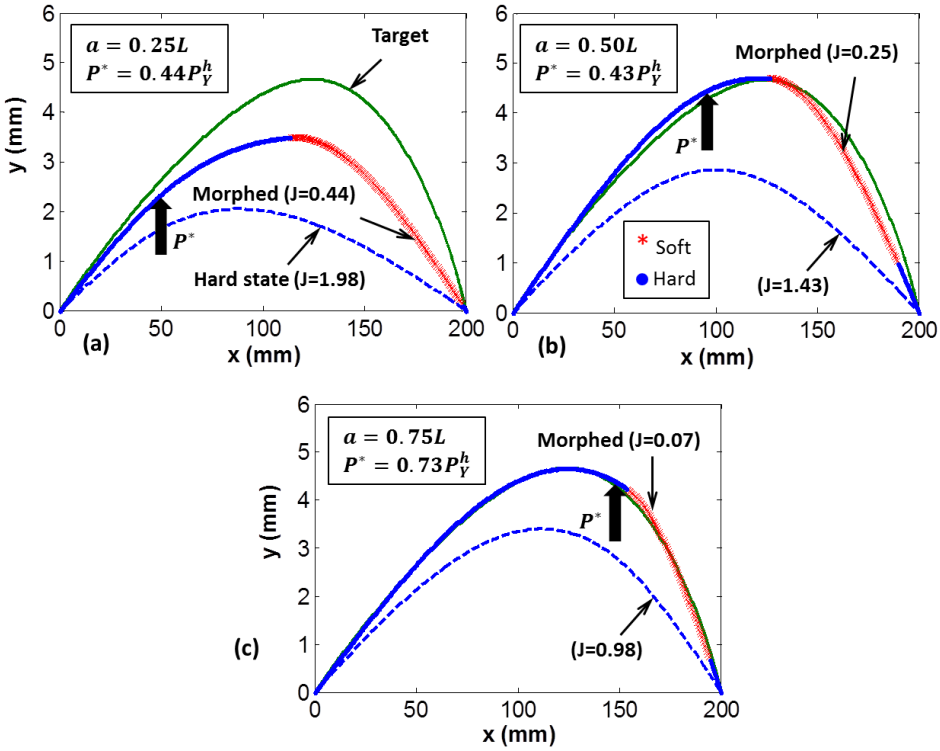

Figure 3-9: Morphing with variable force and actuation points.
Deformed hard beam under same boundary condition is also shown. Indexes are displayed in parentheses

3.3.3 Results summary and remarks

Table 3-6 shows a summary of optimal results for the above four cases. For each case, the performance index numbers for the morphed shape and that of the totally hard case (using same boundary conditions) are presented. By comparing the index values, one could appreciate the advantage of local softening in reducing the force and error. It is worth mentioning that for all the cases, the multiple-segment study ($1 < N_s \leq 3$) was also performed. In all cases, a uni-segment scheme ($N_s = 1$) was reported to be optimal. When the actuation location and magnitude were constrained, the worst shape error ($J = 0.41$) was observed, although a large softening length was invested.

Table 3-6: Comparison of four single actuated cases

Case	a	P	w_s^*	P_s^*/P_Y^h	J	J_h
1	Constant	Constant	0.54	0.25	0.41	1.80
2	Constant	Variable	0.31	0.43	0.25	1.43
3	Variable	Constant	0.79	0.25	0.35	2.52
4	Variable	Variable	0.29	0.73	0.07	0.98

w_s^*: optimal segment length, J: shape error, J_h: shape error in the totally hard case

P_s^*: optimal force, P_Y^h: maximum allowable force in hard state

$N_s = 1$ (Optimal number of soft segments for all the cases)

As one of the constraints (force location) was released, with larger material transformation, better shape ($J = 0.35$) was achieved. A further improvement in shapes was observed when the actuator remained fixed in the middle but larger force was spent ($J = 0.25$). Note that higher force is compensated with less modulus change. The most accurate shape ($J = 0.07$) was achieved when actuation magnitude and position were both allowed to be optimized.

It is interesting to point out that softening of segments of the beam enabled the wide variety of shapes to be obtained with limited forces. After the change is achieved, if the soft segment(s) hardens and the force is removed, the beam would retain a shape which is between the morphed and undeformed shape due to the inherent elasticity of the modulus when morph occurred.

Multiple soft segments: It was noticed that no more than one soft segment was needed for an efficient shape morphing and the second soft segment appeared to be trivial. Now, consider an alternative target shape with a flat head shown in Figure 3-10. The loading condition is selected to be $a = 0.5L;\ P_Y^s \le P \le P_Y^h$. Table 3-7 summarizes the optimization results.

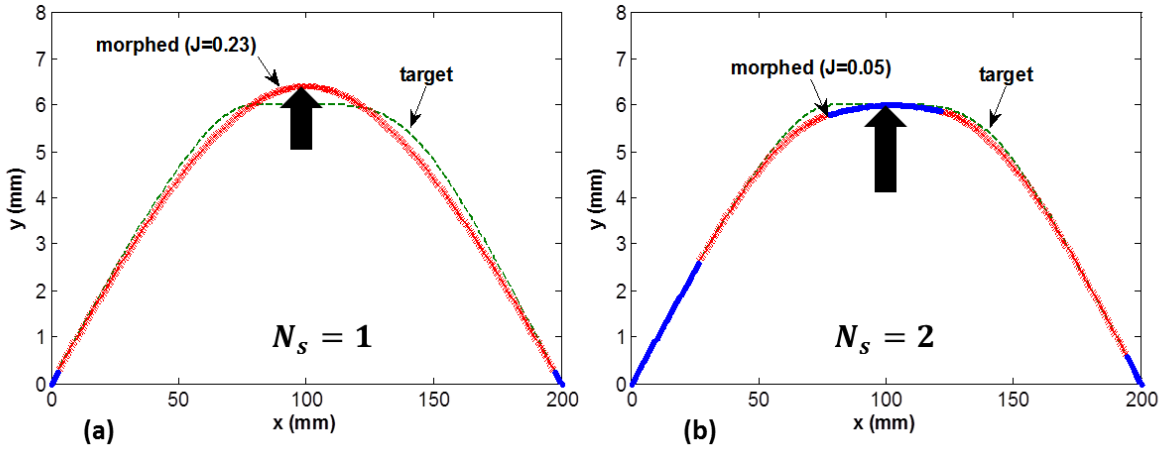

Figure 3-10: Morphing with different numbers of soft segments

Table 3-7: Morph parameters with different number of soft segments

Number of soft segments	**Actuation force** $(\times 1/P_Y^h)$	**Soft segment center** $(\times L^{-1})$	**Soft segment length** $(\times L^{-1})$	**Performance index** (J)
1	0.24	0.5	0.97	0.23
2	0.38	(0.26 , 0.79)	(0.25 , 0.36)	0.05

Figure 3-10 shows the morphed beams with two different numbers of soft segments. As the target is horizontally symmetric and has no peak in the center, the uni-section softening scheme does not seem to perform efficiently. The optimization algorithm also supports this fact by reporting no material transformation when the maximum number of soft regions was set as one. The resulting force could conform the sides of the desired shape; however the top of the morphed shape has large dissimilarity with the target (Figure 3-10a). With two soft segments, a bi-section morphing scheme creates the top flat shape and the shape error is reduced drastically. Note the increased force magnitude is required to cause the flat edges to bend.

Comparing the number of segments for the two studied target curves reveals that using a more complex algorithm with larger possible soft segments seems favorable, as any extremely short soft segments (like morphing to the first target curve) can always be disregarded in cases where a uni-sectional scheme is just as good.

3.3.4 A practical example

We propose an application example to support the significance of the discussed inverse morphing method. Consider a micro switch whose function is to activate one of the several states at any given time (Figure 3-11). The immobile actuator is positioned in the middle while the tip of the deflected structure would connect to the desired point to establish the electrical connection. Multi state switching is achieved by local manipulating of the modulus.

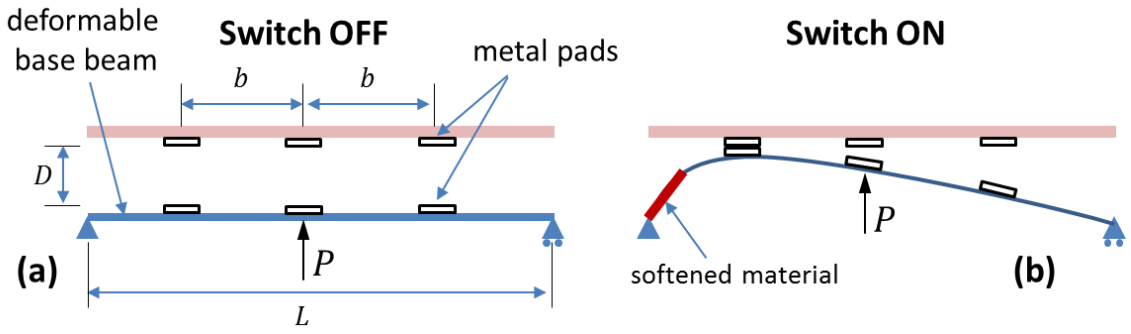

Figure 3-11: Multi-state switch activated with middle force and modulus-changing

Table 3-8 presents the specific geometrical parameters for the switch. To activate the left state, the beam should deform to a shape whose peak is located on the left pad's position and its maximum vertical displacement equals to the designed value (Figure 3-11b).

Table 3-8: Geometrical specifications of multi-state switch

Parameter	Specification	Value
L	Length of the base beam	100 mm
D	Metal pads vertical distance	10 mm
b	Metal pads horizontal distance	20 mm

A B-spline curve that satisfies the functional requirements was generated by manipulating the control point (Figure 3-12). The cubic B-spline has 6 control points (two at the left end, one shown intermediate point located at (14,20 *mm*) and three at the right end). This curve was then converted and utilized as the target shape.

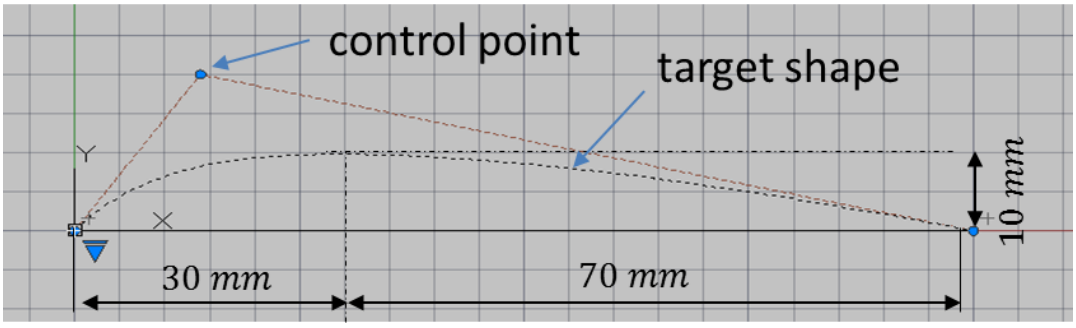

Figure 3-12: CAD drawing of the target shape for this example

It was assumed that the actuation force is constant ($P = 0.25P_Y^h$) and the material modulus is nominally 3,000 MPa, and can change to one of four discrete lower moduli (100, 250, 500 and 750 MPa). In this study the GA was repeatedly run with different values used for the soft modulus. The optimization routine took multiple moduli into account and automatically reported the best modulus to change to be $E_s^* = 100\ MPa$. For the sake of comparison, the soft modulus was manually changed and the optimal case for each value was found and reported in

Table 3-9. In all cases, a uni-section morphing scheme was used while the force value remained constant; Figure 3-13 compares the progression of the morphed shapes with different

soft moduli. As the material becomes softer, the segment's center moves towards the left as does the peak of the achieved shape. The peak in case 4 locates in the desired pads' contact position.

Table 3-9: Morphing parameters for various soft moduli
(the optimal set is shaded)

Case No.	Lower modulus (MPa)	Soft segment center ($\times L^{-1}$)	Soft segment length ($\times L^{-1}$)	Performance index (J)
1	750	0.5	1	3
2	500	0.3	0.7	1.9
3	250	0.24	0.46	1
4	100	0.19	0.28	0.5

For all the cases: $E_h = 3000\ MPa\ , P = 0.25P_Y^h$

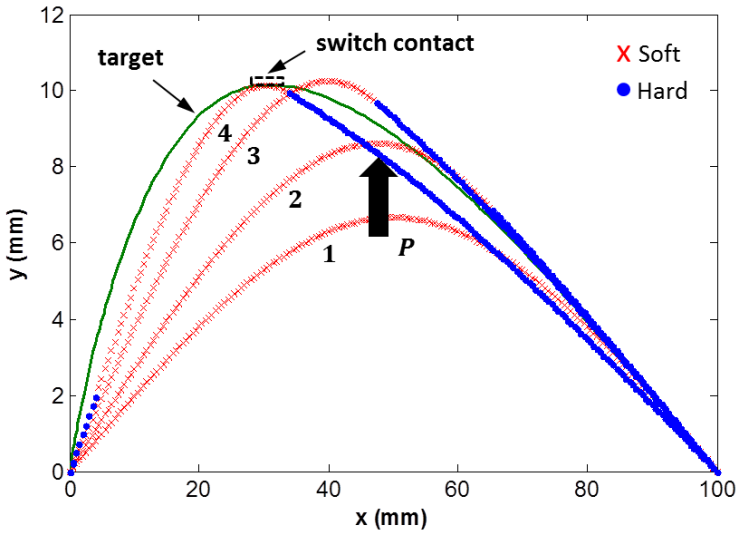

Figure 3-13: Progression of the morphed shapes with various low moduli.
Note that the force is always fixed in the middle

Note that to achieve contact with the right pad the morphing pattern can be mirrored about the beam midspan, and to make contact with the center pad one can simply apply the same force

with complete modulus change to 500 MPa. It is worth noting that in all cases, same force value and location is used.

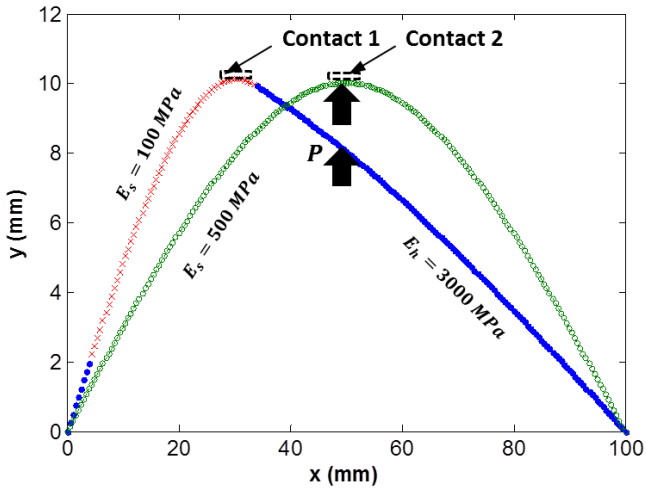

Figure 3-14: Establish left and middle contact using fixed force and different lower moduli

4.0 MULTIPLE ACTUATION INVERSE MORPHING

In the previous chapter, the inverse morphing problem with single actuation was formulated and solved. When more complex target shapes are expected, using a single force might not be sufficient and using higher number of actuators would be necessary. As an extension, this chapter is dedicated to solving the inverse shape morphing of the structure when finite numbers of actuators are exerted in certain fixed locations of the structure. The beam geometry is similar to the previous chapter.

4.1 STATEMENT OF THE PROBLEM

Let consider the simply supported beam shown in Figure 4-1. There are finite N_a fixed actuators in locations indicated as x_a^j where $j = 1,2,\dots,N_a$. Softened segments of the structure are represented by their center points (x_s^k) and lengths (w_s^k), where $k = 1,2,\dots,N_s$ and N_s is the maximum number of segments given as a known parameter.

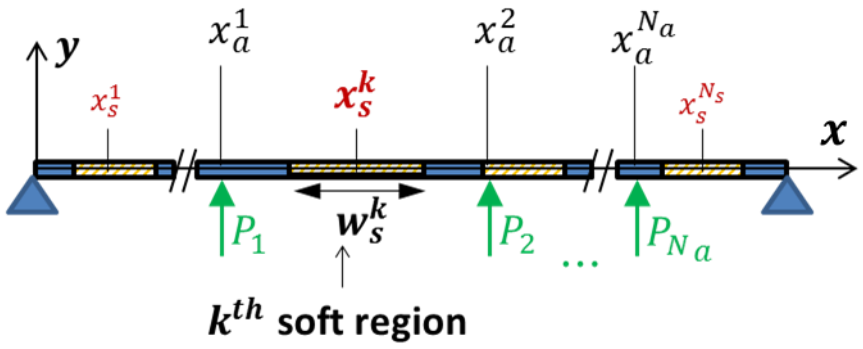

Figure 4-1: Local softening of the beam with multiple actuations

The shape of the morphed beam is prescribed by the arrangement of the soft segments and the actuation forces, i.e. $y_m = y(\vec{P_j}, x_a^j, x_s^k, w_s^k)$. Given a target shape, $y_t(x)$, new optimization problem could be summarized in the following form:

$$\min J\{y(\vec{P_j}, x_a^j, x_s^k, w_s^k), y_t\} \qquad 1 \le j \le N_a\ ;\ 1 \le k \le N_s \tag{4.1}$$

Similar constraints as introduced in section 3.1 are used for this problem.

4.2 STRUCTURE'S SHAPE EQUATION

For a supported beam with multiple actuations (Figure 4-1), assuming a planar deformation, the governing elastomechanical equations can be defined as:

$$M(x) = E(x)I\frac{d^2y}{dx^2} = \sum_{j=1}^{N_a} \vec{P_j}\left[-\frac{(L - x_a^j)}{L}x + < x - x_a^j >\right] \tag{4.5}$$

Double integration of the moment equation yields the elastic shape of the structure:

$$y(x) = \frac{1}{E(x)I}\left(\sum_{j=1}^{N_a}\frac{1}{6}\vec{P_j}\left[-\frac{(L-x_a^j)}{L}x^3 + < x - x_a^j >^3\right] + c_1 x + c_2\right) \tag{4.6}$$

where constants c_1 and c_2 can be determined from the boundary conditions and continuity of displacement and slopes in adjacent segments. These conditions are described in the following three sets of equations:

$$y_1(x)|_{x=0} = 0$$
$$y_{N_s}(x)\big|_{x=L} = 0 \tag{4.7}$$

$$y_i(x)|_{x^i} = y_{i+1}(x)\,|_{x^{i+1}} \tag{4.8}$$

$$\frac{dy_i}{dx}\bigg|_{x^i} = \frac{dy_{i+1}}{dx}\bigg|_{x^{i+1}} \tag{4.9}$$

Where $y_i(x)$ defines the displacement of the ith segment that is described with its center point (x_s) and length (w_s).

Applying these conditions, one can summarize Eqs. (4.7-9) in the following closed form and solve for the segment constants:

$$\begin{bmatrix} \cdots & & \cdots & & \cdots & & \cdots & \\ \vdots & & & & & & & \vdots \\ i-1 & -E_{i-1}^{-1} & E_i^{-1} & & & & & \\ \vdots & & & & & & & \\ i+N_s-2 & -x^i E_{i-1}^{-1} & x^i E_i^{-1} & & & & & \\ \vdots & & & & & & & \\ 0 & 0 & 0 & & & & & \\ 0 & \cdots & 0 & 0 & & & & \\ & & & N_s & N_s+1 & & i+N_s-1 & i+N_s \\ & & & 2N_s & L & \cdots & -E_{i-1}^{-1} & E_i^{-1} \\ & & & 2N_s-1 & 0 & & 0 & 0 \\ & & & 2N_s & 1 & & & \end{bmatrix} \begin{bmatrix} \vdots \\ c_1^{i-1} \\ c_1^i \\ \vdots \\ c_1^{n_s} \\ \vdots \\ c_2^{i-1} \\ c_2^i \\ \vdots \\ c_2^{n_s} \end{bmatrix} = \begin{Bmatrix} \vdots \\ A_i f(x^i) \\ A_i g(x^i) \\ \vdots \\ 0 \\ -g(L) \end{Bmatrix}$$

In the above matrix, elements corresponding to the i-th segment have been highlighted. The material constant A was defined in Eq. (2.20). $f(x)$ and $g(x)$ are functions defined as:

$$f(x) = \sum_{j=1}^{N_a} \frac{1}{2}\vec{P_j}\left[-\frac{(L - x_a^j)}{L}x^2 + < x - x_a^j >^2\right]$$
$$g(x) = \sum_{j=1}^{N_a} \frac{1}{6}\vec{P_j}\left[-\frac{(L - x_a^j)}{L}x^3 + < x - x_a^j >^3\right] \quad (4.10)$$

Ultimately, the morphed shape of the structure is represented as the following form:

$$y(x) = \sum_{i=1}^{N} H_i(x) y_i(x) \quad (4.11)$$

where $H_i(x)$ is the *Heaviside* function and $y_i(x)$ is the i-the segment's deflected shape function:

$$y_i(x) = \frac{1}{E_i(x)}\left(g(x) + c_1^i x + c_2^i\right) \quad (4.12)$$

4.3 EXTENDED WEIGHTED PERFORMANCE INDEX

Previously, the performance index was defined only based on shape similarity. An index $J_{err}(y(x), y_t(x))$ controlled the RMS error of the morphed shapes with the target. This index was effective and robust enough to determine optimum shape morphing; however, depending on the application, one might rather optimize the other physical parameters than shape, such as softening energy (i.e. energy used to soften a part of the structure) or actuation external work. The current index is incapable of involving these terms in the optimization procedure. Based on

the physical limit, each index would have a nominal weight to normalize the term. In this section, effect of additional terms and weight factors are studied.

4.3.1 Additional performance terms

A *softening energy* term (J_{sft}) is defined to specify the energy used for transforming the material in certain locations of the structure from a known high to low modulus. As a fair estimate, this energy term could be represented by the ratio of the soft segments' lengths to the total length of the beam (Eq. 4.13)

$$J_{sft} = \frac{\sum_{k=1}^{N_s} w_s^k}{L} \tag{4.13}$$

Where w_s^k is the length of the k-th segment. This implies that without needing a scaling weight, the softening energy term is always bounded between 0 and 1.

While stimulation energy is dedicated to locally transform the smart material, actuation work causes the structure to morph towards the target shape. Let J_{wrk} be the external work of the actuators that, assuming no structural damping, is stored as elastic *strain energy*. In a multiple-actuated supported beam, the external work is calculated from Eq. (4.14).

$$J_{wrk} = \int_0^L \frac{M(x)^2}{2E(x)I}\, dx \tag{4.14}$$

Where $M(x)$ is the moment distribution function defined in Eq. (4.5).

4.3.2 Determine scaling weights

The objective terms discussed so far have different magnitudes and thus are not comparable in a single function. In order to have a sensible performance, all the terms should have magnitudes of the same order. This can be assured by assigning proper scaling weights to bound each term within 0 and 1. With that in mind, a new performance index is defined in the following form:

$$J = \alpha_e J_{err} + J_{sft} + \alpha_w J_{wrk} \tag{4.15}$$

Where α_e, α_w are the error and external work scaling weights, respectively. These weights are determined based on the physical limits as well as mechanical properties.

a) External work weight: Consider the simply supported beam shown in Figure 4-2. For fixed force locations, external work depends on the force and softening length (Eq. 4.8). In order to scale the values, we use maximum external work.

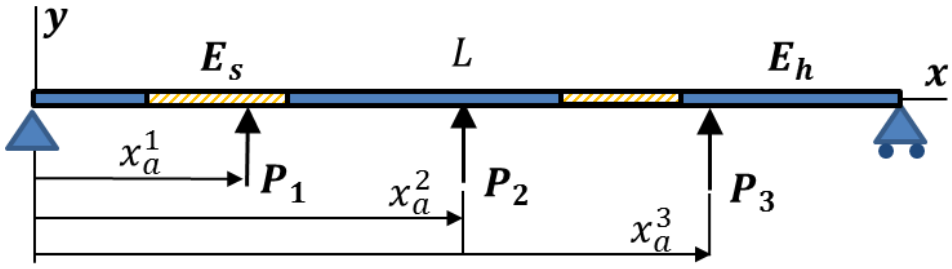

Figure 4-2: Multiple-actuated supported beam

Figure 4-3a presents five different morphing configurations with their strain energies. P^h and P^s are the permissible forces in hard and soft state defined in Eq. (3.1). Figure 4-3b shows the corresponding morphed shapes.

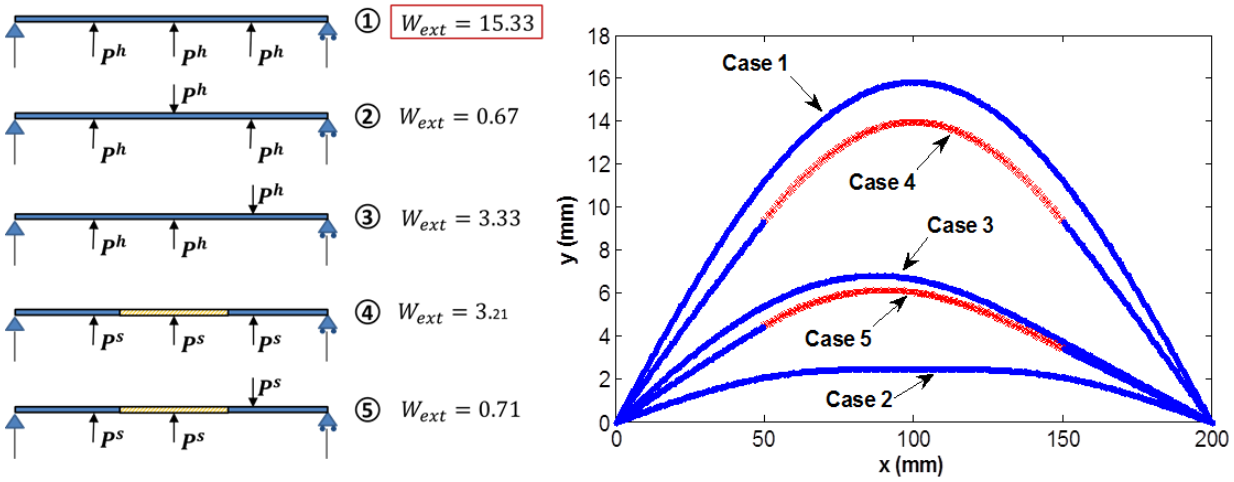

Figure 4-3: Different loading configurations and their produced work. Corresponding morphed shapes are shown in the right.

It is noticed that maximum external work is for the case where all the actuators use their largest capacity in the same direction to deflect the entirely hard beam. We use the maximum external work to define the normal weight α_w as follows:

$$\alpha_w = \frac{1}{J_{wrk}\left(P_j = P^h, x_a^j, x_s^k, w_s^k = 0\right)} \tag{4.16}$$

b) Shape error weight: to determine the shape error weighting, we need a good estimate of the maximum error value. We propose two different approaches:

Approach 1: This method determines the error weight based on the target shape. We assume that the maximum error occurs when the structure morphs to the shape which is the mirror of the target with respect to the horizontal axis (Figure 4-4). In other words, the maximum error is two times the error between unloaded beam and target shape. The normal weight is then:

$$\boldsymbol{\alpha_e^1} = \frac{1}{2J_{err}(y|_{P=0}\,,\, y_t)} \tag{4.17}$$

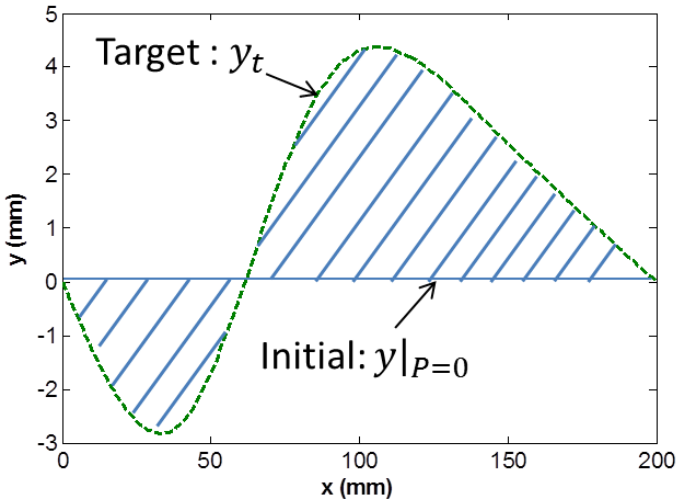

Figure 4-4: The error of the target with the unloaded beam is used to determine the weight

Approach 2: This method assumes the largest error is double the reference shape resulted by loading the hard structure with full actuators all in the same directions (Figure 4-5). Similarly, the *double* factor is because the most undesirable morphing would be a case where target is selected as the mirror of the maximum loaded shape.

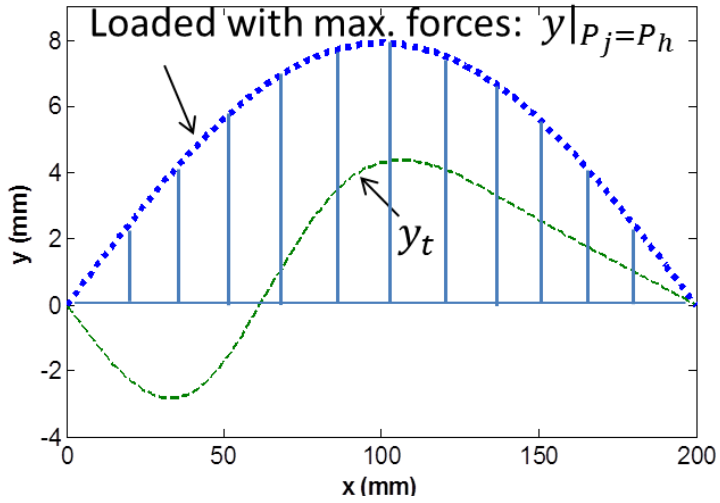

Figure 4-5: Error between the outermost shape with unloaded beam used for weighting

Therefore, the alternative normalizing error weight could be calculated using:

$$\boldsymbol{\alpha_e^2} = \frac{1}{2J_{err}\left(y|_{P_j=0},\ y|_{P_j=P^h,\ w_s^k=0}\right)} \tag{4.18}$$

The latter weight includes all the achievable elastic shapes and can be calculated while finding the energy weight. Hence, this weight will be used for the rest of the analysis.

4.3.3 Numerical examples

To compare the effect of the performance weightings, a multi-actuated case is studied. Figure 4-6 demonstrates the target shape created as a B-spline curve.

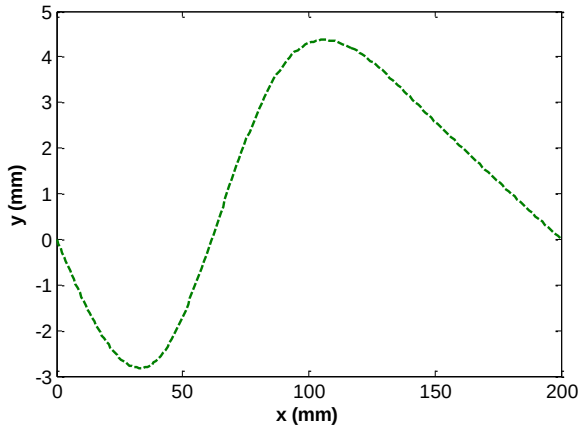

Figure 4-6: Target shape (B-spline curve) for weights effect study

The loading and softening boundary conditions are defined to be:

$$\begin{aligned} &N_s = 3 \text{ (maximum number of soft segments)} \\ &N_a = 3 \text{ (maximum number of actuators)} \\ &\overrightarrow{x_a} = [0.25\ \ 0.5\ \ 0.75] \times L \text{ (actuation points)} \\ &0.2 \le |P_j| \le 0.8\,; \quad 1 \le j \le 3 \end{aligned} \tag{4.19}$$

Considering the performance terms in Eq. (4.16), various cases are defined:

Case 1: The objective is to only minimize the shape error using weighted performance index ($J = \alpha_e J_{err}$). The optimized results are shown in Figure 4-7. The force values are normalized to their maximum capacity (P^h). For comparison, the softening and strain energy costs are also included in the figure but not used in the optimization.

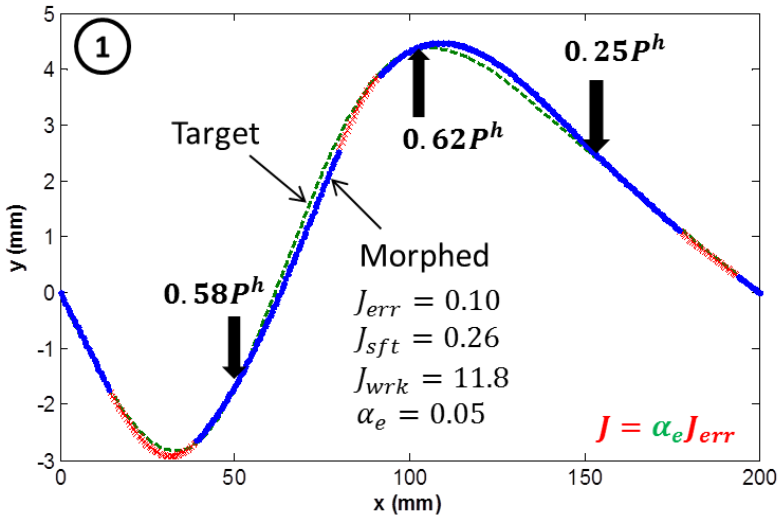

Figure 4-7: Morphed shape using shape error cost function (case 1)

The morphed shape is significantly similar to the target. However, in the absence of other cost terms, considerable energy has to be used to soften the material and actuate the beam.

Case 2: The objective includes the softening energy. The morphed shape is illustrated in Figure 4-8. Compared to previous case, less energy is now invested for changing the material's phase. Due to the constrained modulus variation, however, the shape error increased. Moreover, because of reduced compliance, larger external work is required to deform the structure.

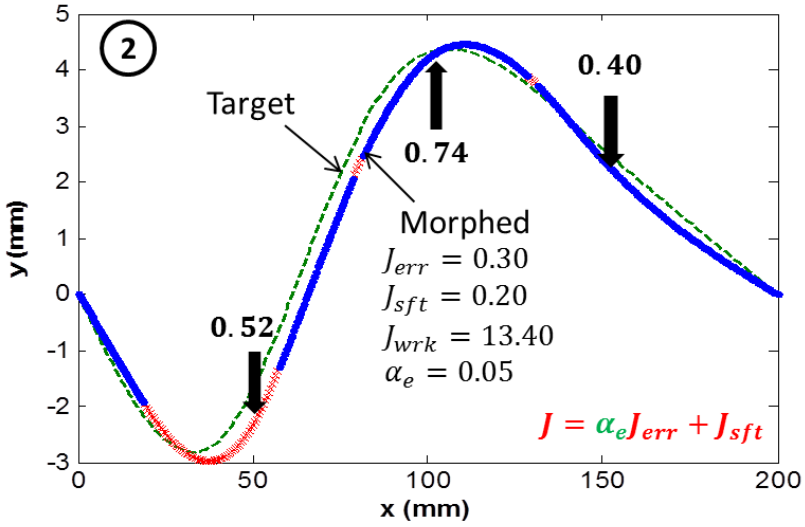

Figure 4-8: Morphed shape using error and softening energy costs (case 2)

Case 3: This case includes all the performance indexes while the strain energy term is non-weighted. The resulted morphed beam is illustrated in Figure 4-9.

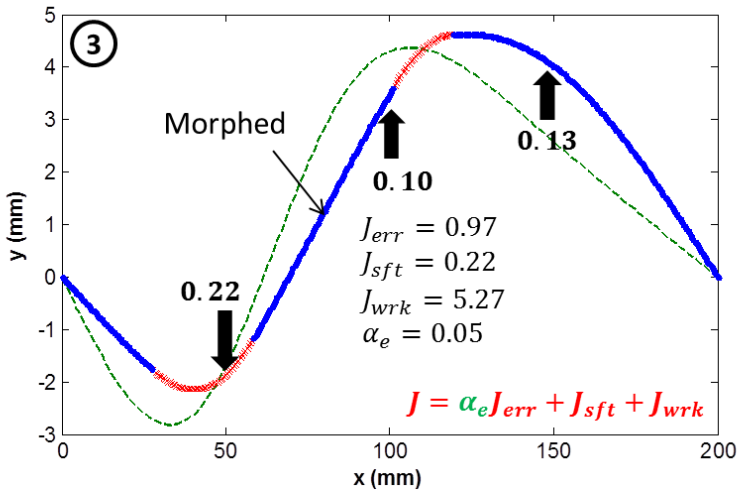

Figure 4-9: Morphing with error, softening and *non-weighted* strain energy (case 3)

Notice that the external work is substantially decreased. However, due to magnitude difference of the terms, the optimization algorithm could not efficiently determine the optimal value. This emphasizes the need for proper scaling weights in the performance index.

Case 4: In this case, the index is appropriately weighted based on the discussed scaling factors. The resulted shape is presented in Figure 4-9. Despite a slight increase in strain energy (compared to previous case), the shape error is significantly improved.

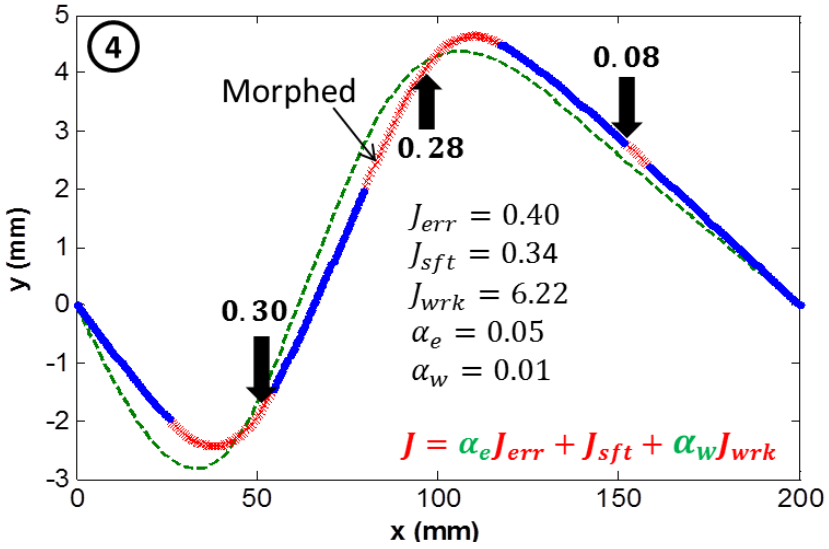

Figure 4-10: Morphing with shape error, softening and *weighted* strain energy (case 4)

In this section, using a numerical example, the effect of various objective terms on the morphed shape was investigated. Depending on the application and significance level of the terms, one might choose to include some or all of them in the performance index. Since the shape similarity is of the utmost importance in a morphing application, we keep the shape error as the primary objective in the following chapter.

5.0 NUMERICAL MORPHING FOR ARBITRARY SHAPES

For most of the engineering structures with arbitrary shapes, an analytical solution for the elastic deformation does not exist. In these problems, numerical methods are employed to solve the shape morphing problem. In this chapter, a comprehensive algorithm to solve the morphing of an arbitrary structure is presented and then validated using the previous results. Ultimately, the morphing of a specific engineering application is explored.

5.1 COMPUTATION ALGORITHM

A numerical algorithm to solve the morphing of an arbitrary structure is proposed in Figure 5-1. In this algorithm, computational and numerical programs are interchangeably used. The boundary conditions (location and limit of the actuators and maximum number of segments) and initial conditions including population size, reproduction rules (e.g. crossover fraction, mutation rate) and stop criterion are realized and introduced. A new generation with given properties is generated in the computational platform (here MATLAB®). Each population in the generation contains a solution set. For example, to solve for the location and length of one single segment, introducing an initial population size of 50 results in the formation of 50 random solution sets (individuals) in the form of $[x_s, w_s]$ at the first generation. Then, each individual is sent into a performance evaluation subroutine which continuously interacts with the numerical

FE solver (Abaqus®, Simulia Inc). Based on the given conditions, the structure's model is built and the deformed shape data is stored. Another subroutine calls a written *Python* script to collect the stored results and compute the performance index for that specific individual.

Once the index for all the members of the generation is found, each individual is scored by its performance index and higher index members are chosen as *parents* who can generate *children* for next generation. Individuals with the best performance index (*elites*) automatically survive to the next generation. A new generation is produced using initial parameters and the optimization progresses by replacing the current population with the children. The stopping criteria is either by reaching the preset maximum number of generations or by meeting a defined tolerance of the performance index. The final solution is reported once one of the stop conditions is satisfied.

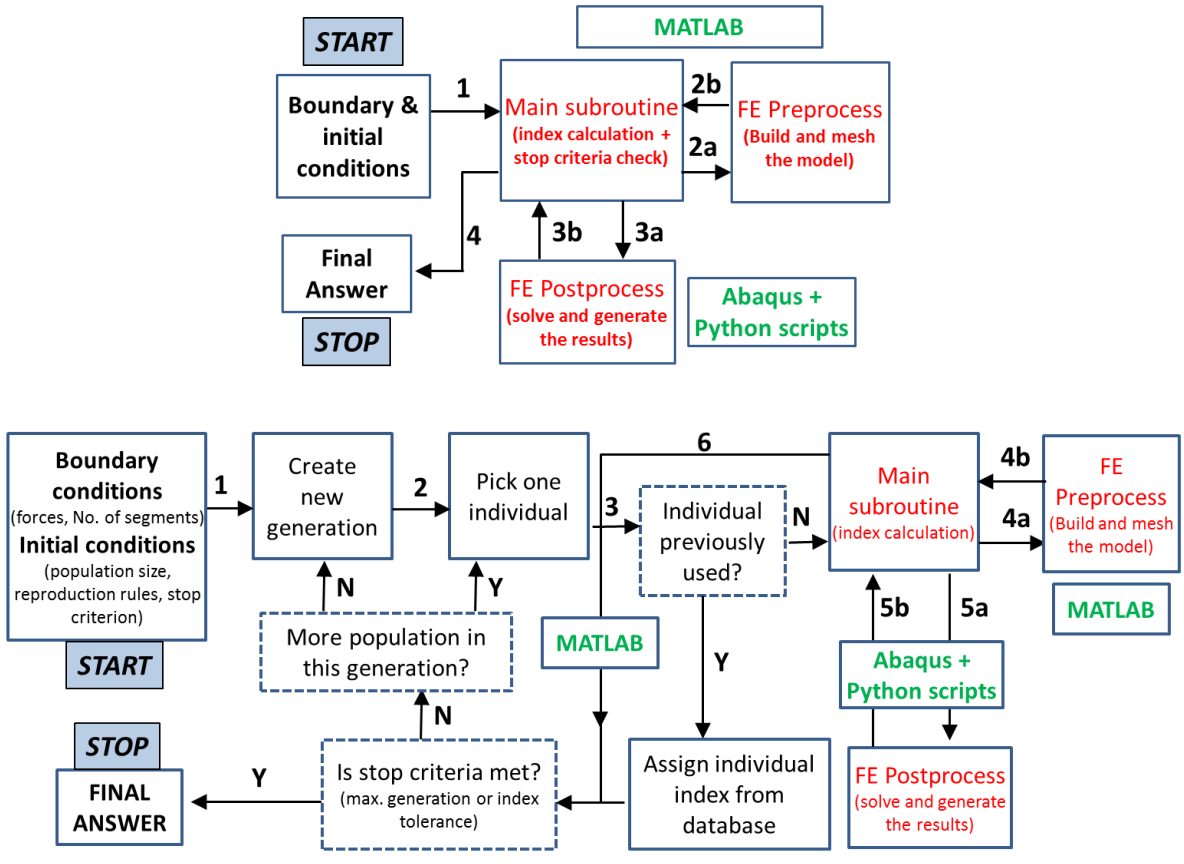

Figure 5-1: Numerical algorithm to solve shape morphing of arbitrary shapes
top: simplified algorithm (arrows show the routines execution order); bottom: detailed algorithm (dashed blocks represent conditions and dotted blocks are developed routines)

5.2 NUMERICAL APPROACH VALIDATION

To validate the algorithm results, two previous cases are studied. Consider case 1, where one off-center load is used to produce an asymmetric curved shape (Figure 5-3*top*). It should be noted that for each geometric model, determining the right population size for the genetic algorithm (GA) is very crucial. The population size, which is the number of individual sets in each generation, is an important measure since it controls the randomness of generated entities which directly affects the chance of finding a result closer to the optimal solution. This study for case 1 is presented in Figure 5-2.

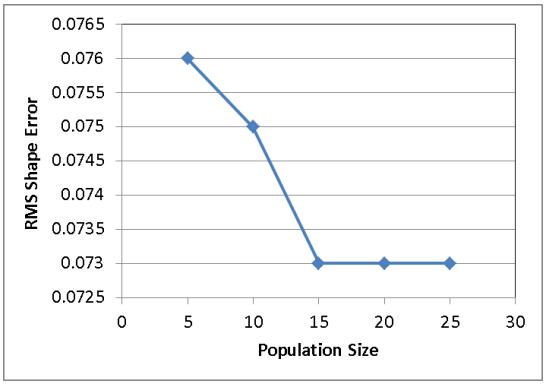

Figure 5-2: Determine the effective population size for case 1

Figure 5-3 illustrates a comparison of analytical and numerical results using the effective population size. Recall that w_s^* and P^* represent the optimal normalized total segment length and force. Both cases were previously investigated with analytical approaches.

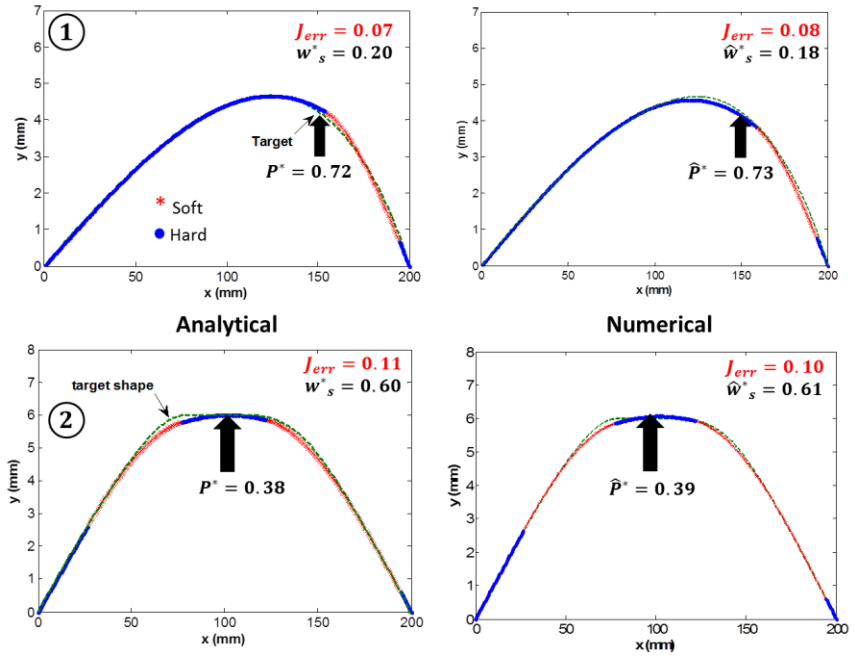

Figure 5-3: Comparison of numerical and analytical solution
case 1 (top) and case 2 (bottom) (* represents the optimal values and ˆ denotes numerical solutions)

Table 5-1 presents a comparison of the two methods. The results are in good agreement. Notice that as the complexity of the target shapes increase, larger population sizes are used and more generations are required to converge to the final optimum solution. To handle even more complex shapes, a population size of 50 was used for the rest of this work.

Table 5-1: Comparison of numerical and analytical results

Case No.	Analytical solution (w_s^*, P^*)	Numerical solution $(\widehat{w_s}^*, \widehat{P}^*)$	No. generations for convergence	Population size
1	(0.2, 0.72)	(0.18, 0.73)	30	15
2	(0.60, 0.38)	(0.54, 0.45)	40	25

5.3 MORPHING IN HYDROKINETICS APPLICATION

As a new way for harvesting water stream energy, hydrokinetics involves suspending a body with particular shape against the flow stream, where the hydrodynamic load distribution causes fluctuations that can be synchronized in a power harvester (Figure 5-4a). Assuming that water stream is uniform and the body depth is considerably larger than the section, one can represent the rigid body with a 2D shape shown in Figure 5-4.

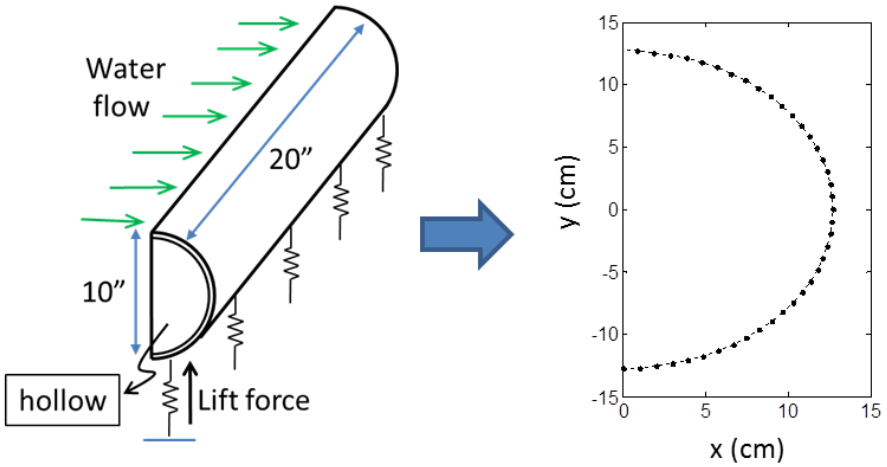

Figure 5-4: Schematic of baseline shape in a hydrokinetic application and the 2D model

The performance of a device is a function of various parameters, including electrical load or speed of the water. As the structure oscillates, surrounding flow parameters such as velocity would also change. Assuming the device adapts for the flow conditions, it should change its shape throughout a cycle to keep its response “optimum”. In each discrete stage of the cycle, there exists an optimum shape that maximizes the lift, hence the extracted power. The goal is to develop morphing algorithms to change from a baseline to multiple target shapes. We assume these shapes are known and would be reached successively. To facilitate the analysis within the scope of morphing, we also neglected the fluid-structure interactions.

5.4 FORWARD MORPHING PROBLEM

We define the *passive* shape as the unloaded baseline geometry shown in Figure 5-5A. The shape can be expressed in an implicit form of $f(r,\theta)$. We assume N_a actuators (here $N_a = 3$) are placed radially at *certain* and *fixed* angular positions (θ_a^j, where $1 \le j \le N_a$). The actuators are assumed to have no rotational degree of freedom during the morphing.

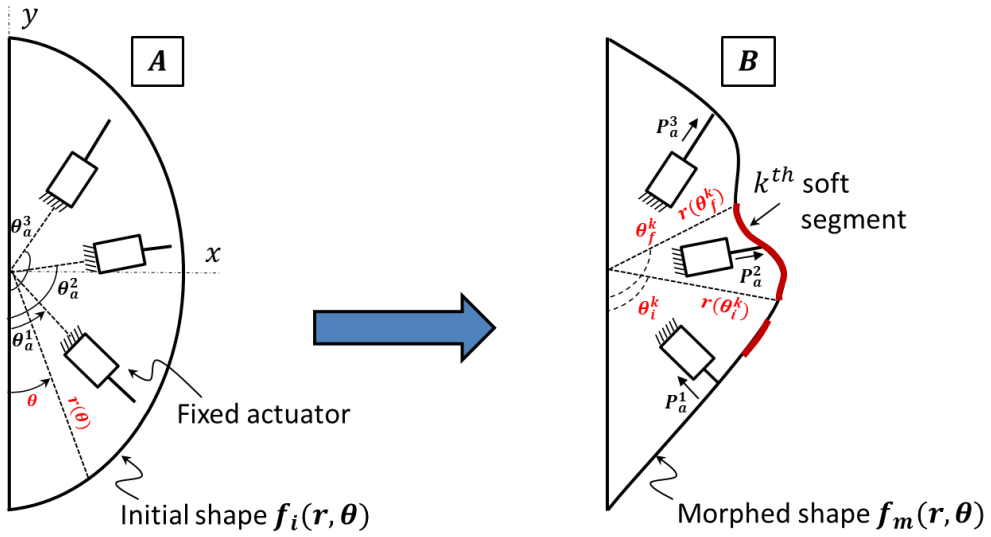

Figure 5-5: Morph from a passive (A) to an arbitrary shape (B) by selective local softening

By manipulating the stiffness in selected segments of the domain while actuating the structure, one can anticipate obtaining an extended family of the shapes (e.g. Figure 5-5B). Assuming finite N_s soft segments, each segment can be represented by the angular position of its initial and final node, namely θ_i^k, θ_f^k, where $1 \le k \le N_s$. The actuation force is also denoted by a force vector $\overrightarrow{P_a^j}$ where $1 \le j \le N_a$.

The forward morphing problem thus involves introducing the location of the soft segments as well as actuation vectors. In order to implement the approach, we developed a MATLAB subroutine to create the FE model and solve the loaded structure via interface with Abaqus FE

software. To build the model, a 2D linear beam element (BEAM) was selected and a mesh convergence study was first performed. To conduct the study, an arbitrary forward morph pattern was defined by using two actuators located at 45° and 135° with magnitudes of $50N$ and $100N$ respectively. For material properties, high and low modulus of 40 and 10 MPa were chosen and a quarter of the structure ($\frac{\pi}{4} \leq \theta_s \leq, \frac{\pi}{2}$) was selected to be softened (Figure 5-6a); then we picked an initial element size of 4cm and using the defined morph scenario, the deformed shape was determined by FE program. Later, the element size was halved subsequently and at each increment, the RMS error between the current and previous morphed shapes was computed. The optimum mesh size of 1cm was chosen based on a defined 5% error variation tolerance (Figure 5-6b). Note that it was assumed that this mesh size will satisfy the convergence condition in any other material distributions.

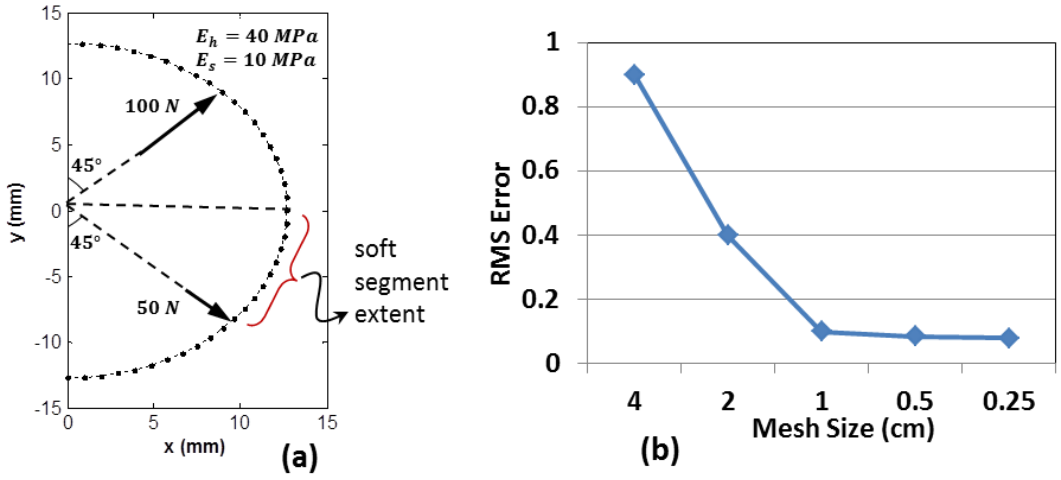

Figure 5-6: a) Morph scenario; b) convergence study to select the optimum mesh size

In the next step, veracity of the model building subroutine was inspected. Using 1cm element size and previous morph pattern (Figure 5-7a), deformation of the curved structure was determined in FE program (Figure 5-7b). Then, we employed our routine to build the model and

find the morphed shape (Figure 5-7c). The similarity of the morphed shapes ensures the validity of the routine to be used for future inverse problems.

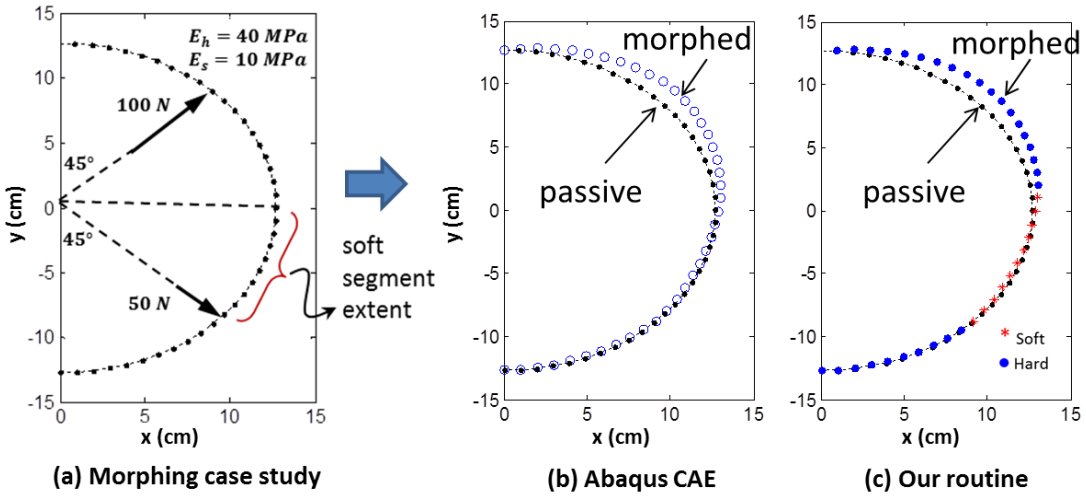

Figure 5-7: Morph case study and results comparison between Abaqus and our subroutine

5.5 INVERSE MORPHING PROBLEM STATEMENT

Given an initial passive and desired target shapes, location and force limit of the actuators and maximum number of segments, the goal is to determine the optimal loads and modulus distribution to minimize shape error. This has been illustrated in Figure 5-8.

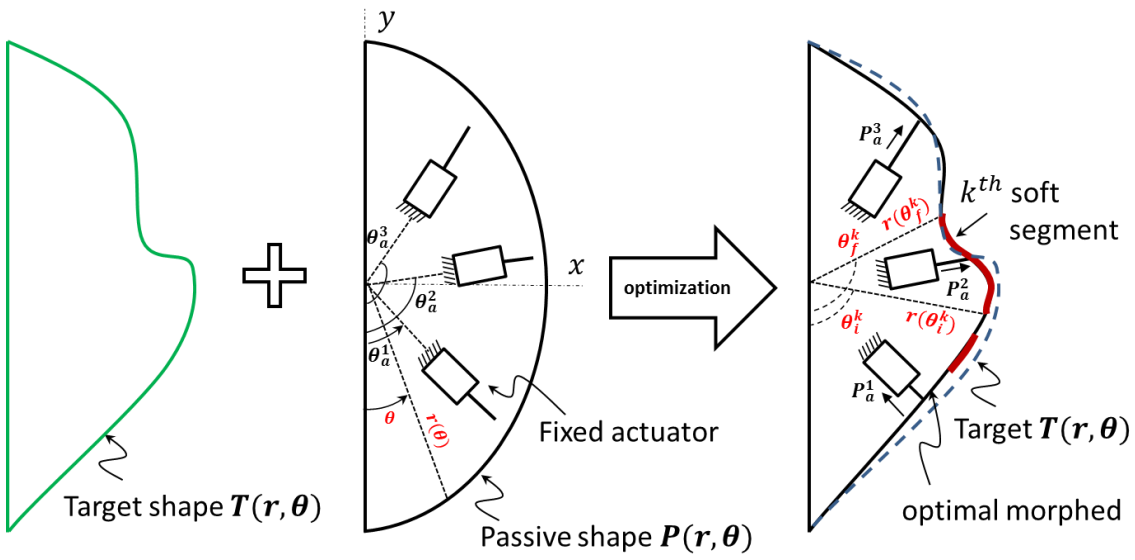

Figure 5-8: Schematic of the inverse problem statement

The optimization problem has been expressed in summary in Table 5-2.

Table 5-2: Mathematical expression of the inverse optimization problem

Given	Find	Constraints
$P(r,\theta), T(r,\theta)$ *(passive and target shapes)* N_s *(max number of segments)* θ_a^j *(position of actuators)* P_{max} *(maximum actuators load)*	*min* $J = E_{RMS}\{T(\theta_i^k, \theta_f^k, P_a^j), M\}$ $\theta_i^k, \theta_f^k, P_a^j$ $1 \le j \le N_a$; $1 \le k \le N_s$	$0 \le \theta_i^k \le \pi$ $\theta_f^k \le \theta_i^{k+1}$ *(no overlap in segments)* $\lvert P_a^j \rvert \le P_{max}$ *(elastic stability)*

5.5.1 Determine actuator's limit

In order to satisfy structural stability, the loading in the actuators should be limited. To determine the maximum allowable force, we assume an elastic behavior for the material and use

a maximum principal strain failure criterion. Accordingly, failure is defined when the maximum principal strain (normally circumferential component) exceeds 0.2% [Timoshenko, 1970].

Assume the baseline structure is actuated with three actuators located at $\pi/4, \pi/2, 3\pi/4$. For the sake of simplicity, we only activate the distal actuator at $3\pi/4$. From a conservative perspective, the structure is in its completely soft phase. We then continue increasing the load and monitoring the principal strain to its critical value (Figure 5-9).

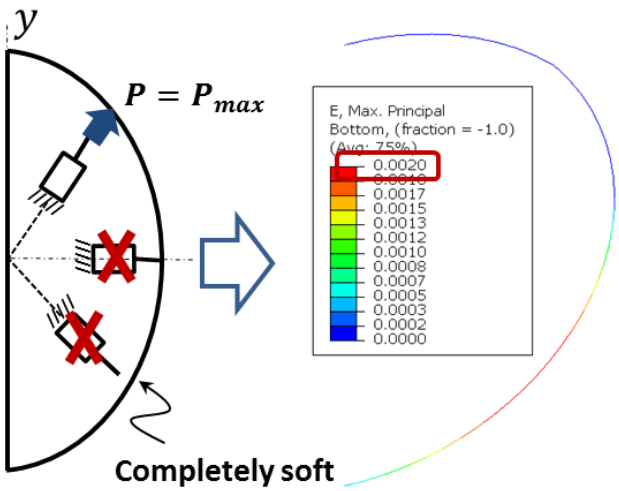

Figure 5-9: Loading with a single actuator and corresponding max. principal strain field

Once the maximum actuating force (P_{max}) is achieved, it is essential to consider various other loading scenarios. Figure 5-10 demonstrates four cases that deform the structure to extreme shapes. In all cases, the maximum loading with lower stiffness has been used.

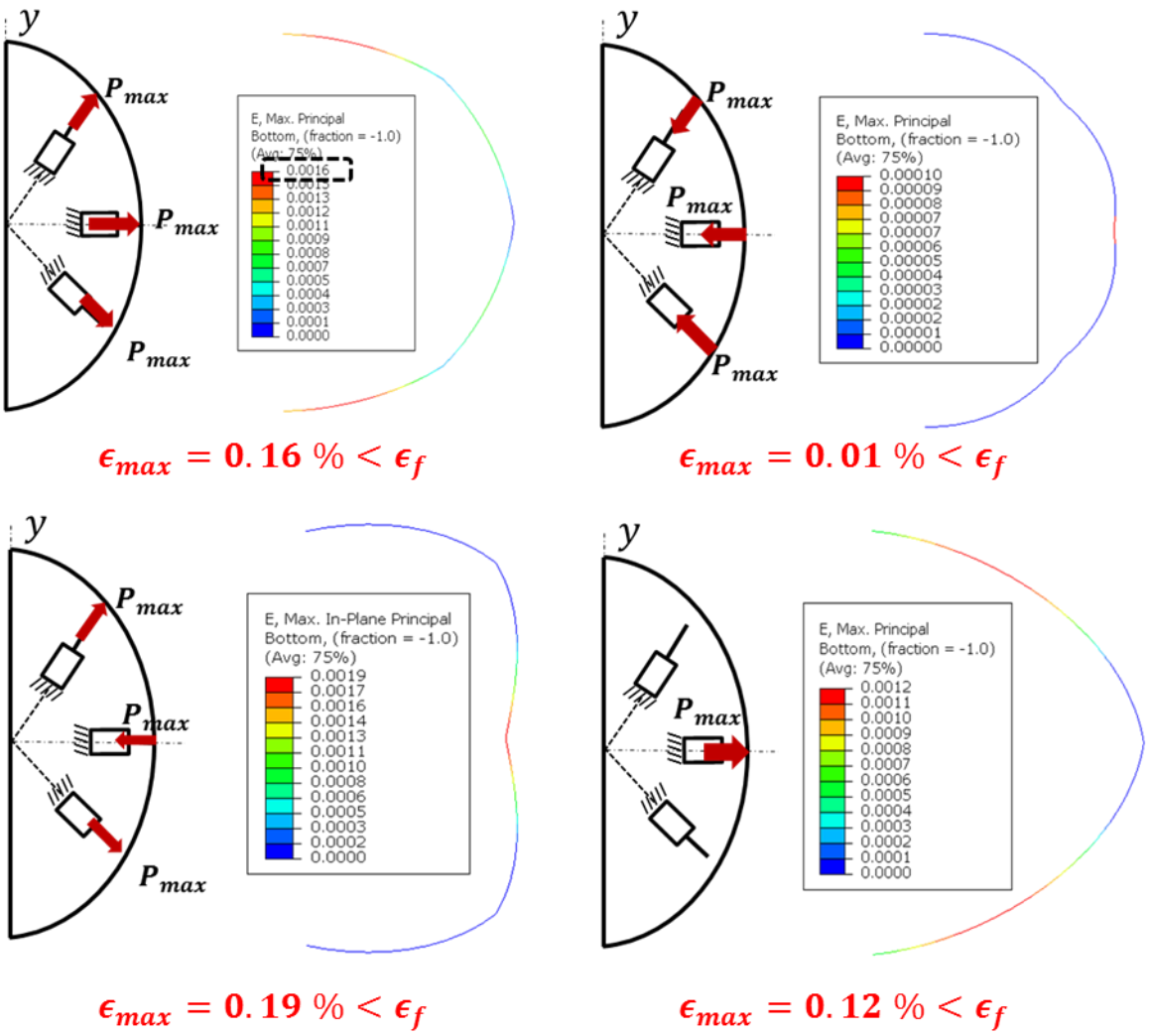

Figure 5-10: Loading scenarios. All maximum principal strains are below the failure limit

It is realized that in all of these cases, the maximum strain remains below the critical value and the structure is elastically stable. If the structure in any of these cases had failed, one would have decreased the force magnitude in the single-loading case and resolved to ensure the stability. We are now going to use the maximum force P_{max} as a bound for the actuators. It is worth noting that this is a conservative limit, since it is based on the most compliant state. Also, the method of choosing that initial actuator to determine the allowable load is specific for this configuration. For models with different loading, one may need to iterate other arrangements.

5.5.2 Discretized morphed and target shapes

As mentioned earlier, target shapes can be most readily represented as geometric *B-splines* or curves. For this example, PTC® Creo Parametric program was used to create the desired curves. Every spline curve can be explicitly defined as a summation of weighted basis functions evaluated in discrete knots. This implies that a spline curve is essentially a discrete function (see Appendix B for formulations).

On the other side, every morphed shape is obtained by loading the structure that is meshed by finite elements with definite stiffness properties. The error between a morphed and target shape is determined by comparing the nodal positions. However, establishing a one-to-one node relationship that guarantees the minimum error could be a challenge. The following example discusses the potential problem.

Figure 5-11a shows the discretized morphed and target shapes when the number of finite nodes in morphed shape (N_m) and spline knots in target shape (N_t) are selected to be equal. From the magnified regions, it can be inferred that, in the side regions, a fairly good one-to-one relationship between the nodes with minimum distance exists; however, in the central region, making such relationship that guarantees the smallest distance is difficult. As the number of knots in the spline curve becomes double the number of morphed nodes (Figure 5-11b), each morphed node can be compared to several target nodes to find a minimum distance ($d_2 < d_1$). The algorithm searches for this target node and once identified, its corresponding distance to the morphed node is recorded and that target node is removed from the search list. When all the morphed nodes found their target counterpart nodes, the RMS value of the stored distances is

reported as the error. From this study, one concludes that the ratio of N_t/N_m can affect the precision of finding a minimum distance. For the rest of this study, we used $\frac{N_t}{N_m} = 2$.

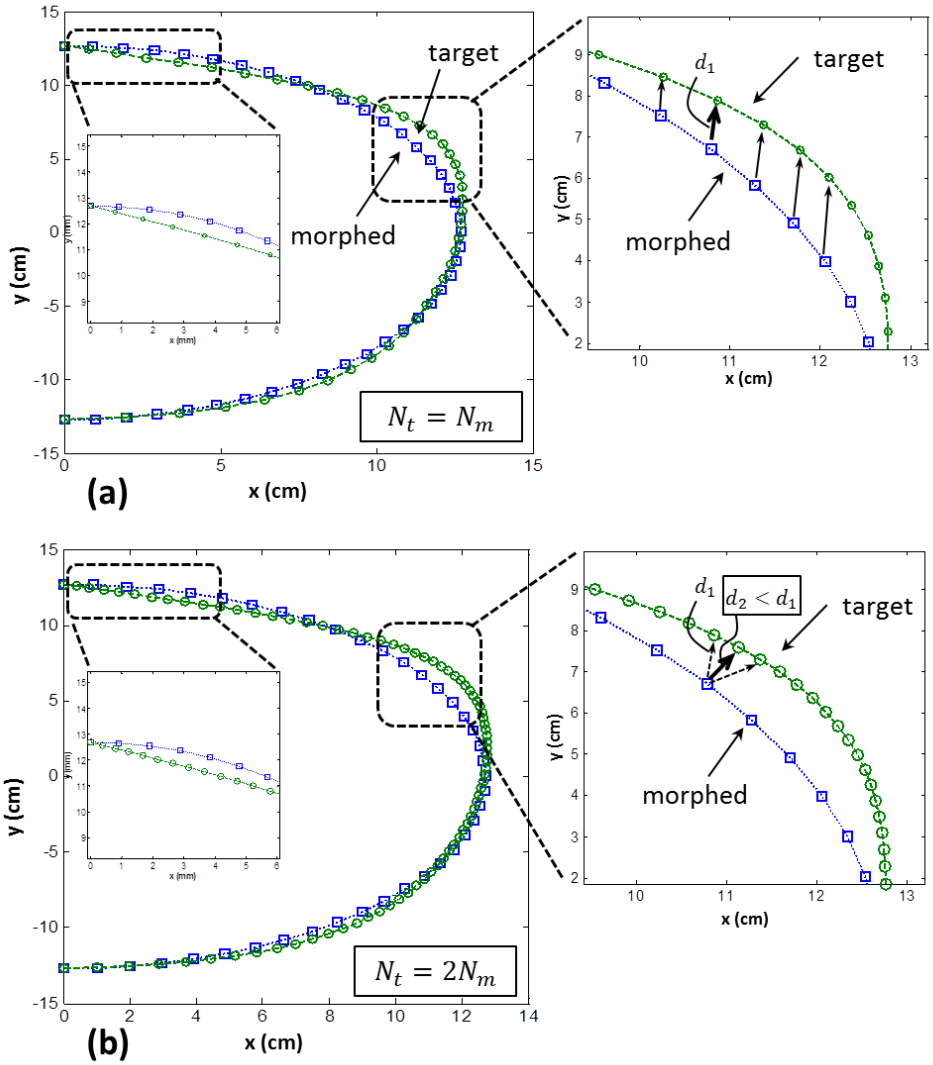

Figure 5-11: Comparing morphed and target shapes
(a) Equal number of spline knots and FE nodes. (b) Number of spline knots larger than FE nodes

5.6 MORPHING CASE STUDIES

Thus far, the optimization algorithm has been laid out and the actuator's limits as well as effective discretization ratio are determined. In this section, we will explore the results for couple of different morphing scenarios.

5.6.1 Single loading morphing

As a simple case study, consider the passive structure with a single fixed actuator at an angular position $\theta_a = 3\pi/4$ (measured from the bottom line). This condition is presented in Figure 5-12a. The performance index is evaluated based only on shape error ($J = J_{err}$). A similar study was conducted to determine the best GA population size. The results suggested a population size of 50, which was used for the rest of this work.

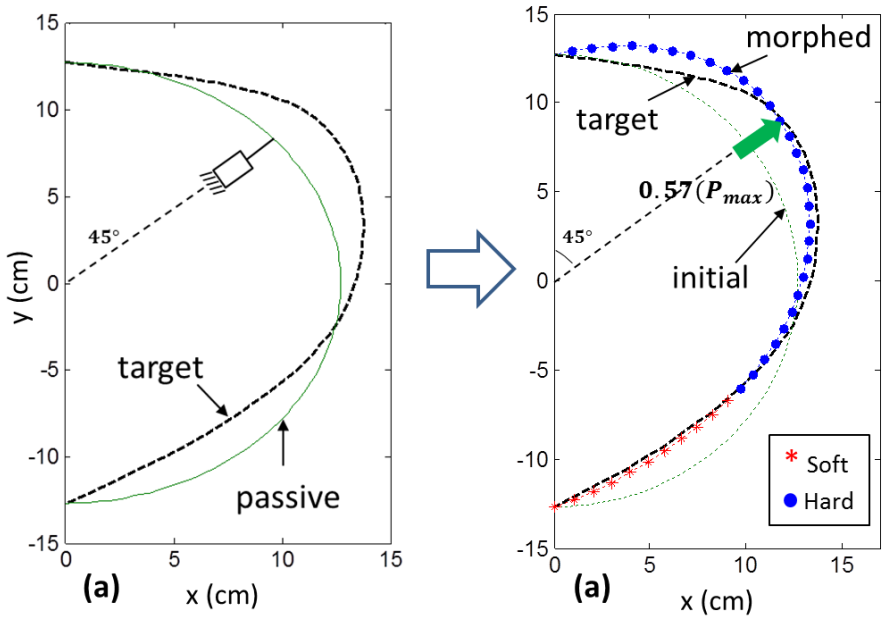

Figure 5-12: (a) Single radial loading; (b) morph with only 57% of the maximum load

The result of morphing is displayed in Figure 5-12b. Using 57% of the maximum load (P_{max}, which was determined in section 5.5.1) and softening 25% of the structure, a fairly accurate solution has been achieved ($J_{err} = 0.68$). It is notable that the lack of sufficient actuators on the bottom half to deform the structure is well compensated with stiffness reduction, yet maintaining the force as low as possible. To appreciate the advantages of the approach, a comparison between shape change with and without stiffness variation has been illustrated in Figure 5-13.

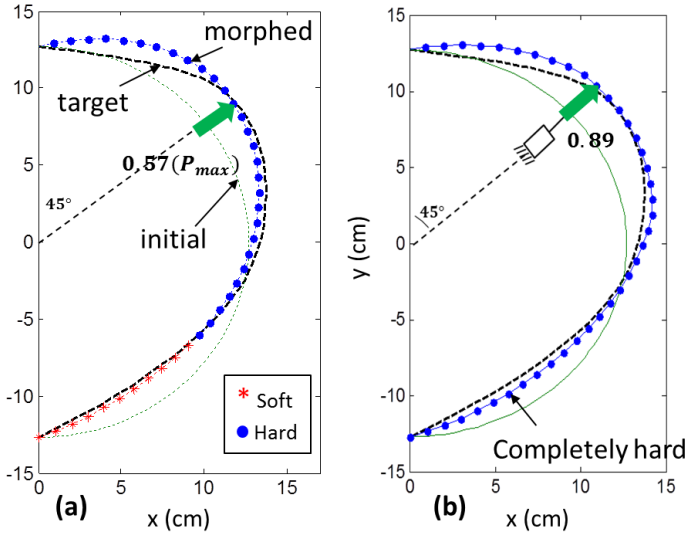

Case	$\frac{\theta_s}{\pi}$	$\frac{P^*}{P_{max}}$	J_{err}	J_{wrk}
a	0.25	0.57	0.68	130
b	0	0.89	0.95	190

Figure 5-13: Comparing single-loaded morph with and without stiffness change
(a) with stiffness change and (b) without stiffness variation

In the side table of Figure 5-13, θ_s/π represents the total angular lengths of soft segments. Firstly, in the completely hard structure, a significantly larger force is required. Despite investing greater force, the accuracy of morphed shape is not improved. Notice the absolute external work to morph (J_{wrk}) is substantially decreased when local modulus reduction was applied.

5.6.2 Higher number of actuators

So far, the validity of the morphing algorithm for a simple desired shape using a single load is verified; however, for more complex target shapes, one actuator may not be sufficient for an accurate morphing. In this section, a different target is selected and the inverse problem is solved. Later, using different performance indexes, the structure's behavior is investigated.

In the advanced configuration, three actuators are positioned at equal angular distance of 45°. The actuators are assumed to be fixed with no rotational degree of freedom (Figure 5-14*a*). Figure 5-14*b* illustrates the deformed structure when a shape error performance index is set as the objective. Notice a large portion of the structure (48%), mostly in the middle, has been softened to enable the major deformations. In the following section, a comprehensive discussion on the contribution of different performance terms is presented.

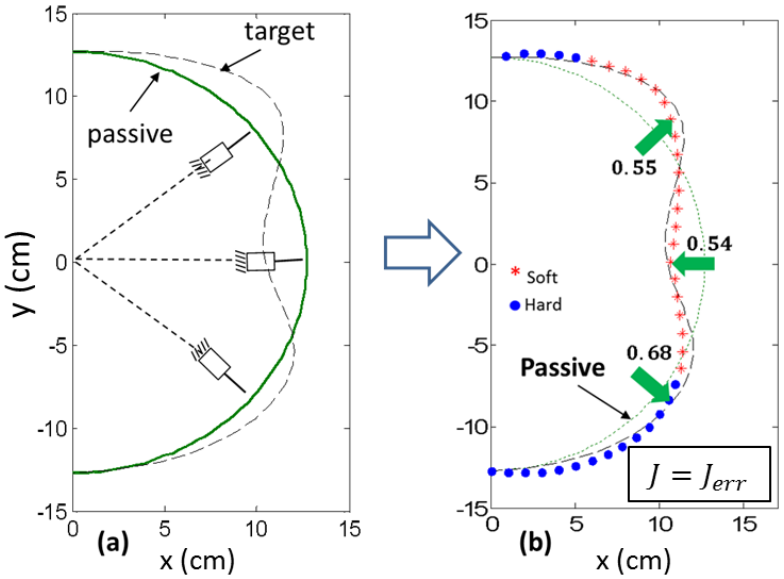

Figure 5-14: Morphing to the complex shape with minimum shape error (force values are normalized by the maximum value, P_{max})

5.7 EXPANDED PERFORMANCED INDEX

Thus far, the performance index has been defined based on shape similarity, as we assumed that it is the most determining parameter in shape morphing. Nevertheless, depending on the type of the application, other significant terms may also contribute in the performance index. Each term will have a nominal normalizing weight based on its physical limit and operational significance. The extra terms include *softening energy* (J_{sft}) and external work (J_{wrk}). These terms were previously defined in Chapter 3 and have the same meaning in this context. To maintain consistency, we need to define proper scaling weight for these terms. A reasonable way is to normalize the terms by their maximum values obtained in extreme morphing configurations. Let assume that the farthest accessible shapes are resulted by loading the *completely soft* structure with *fully-loaded actuators* all in the same radial directions (positive or negative). These extreme shapes are represented by F^+ and F^- in Figure 5-15.

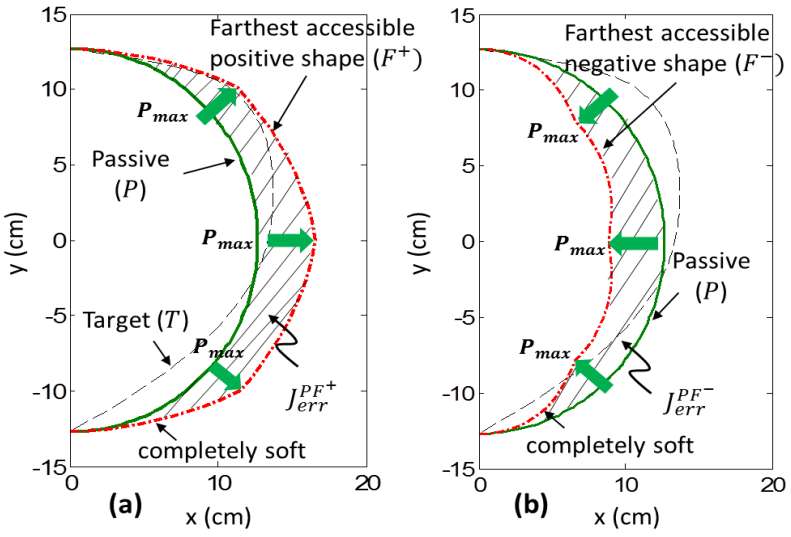

Figure 5-15: Our approach to determine the shape error weight
The summed shape errors between the farthest accessible shapes (F^+, F^-) and passive unloaded beam (P) is used to determine the weight

The error between an extreme morphed curve and a passive initial shape is denoted by J_{err}^{PF}. Assumingly, the highest error (most undesirable case) would occur when the morphed and desired shapes are farthest away in the opposite directions and the errors in positive and negative directions are accumulated. This implies that the error scaling weight is:

$$\boldsymbol{\alpha_e} = \frac{1}{J_{err}^{max}} = \frac{1}{J_{err}^{PF^+} + J_{err}^{PF^-}} \tag{5.1}$$

Likewise, the maximum external work occurs in one of the extreme shapes. Therefore, the corresponding normalizing weight is defined as:

$$\alpha_w = \frac{1}{J_{wrk}^{max}} = \frac{1}{max\,(J_{wrk}^{PF^+}, J_{wrk}^{PF^-})} \tag{5.2}$$

A comprehensive performance index can then be defined as:

$$J = \alpha_e J_{err} + J_{sft} + \alpha_w J_{wrk} \tag{5.3}$$

In order to investigate the effect of performance index terms on the morphing outcome, a case study is considered. Figure 5-16a shows the initial and target shapes. Before inspecting different morphing fitness, one optimization iteration was performed to deform the shape to the target shape with minimum error. Actuation was set to the maximum yielding force in the soft state. The result as shown in Figure 5-16b indicates that, even by exerting maximum force in all the actuators, a successful deformation may not be expected and morphing is necessary.

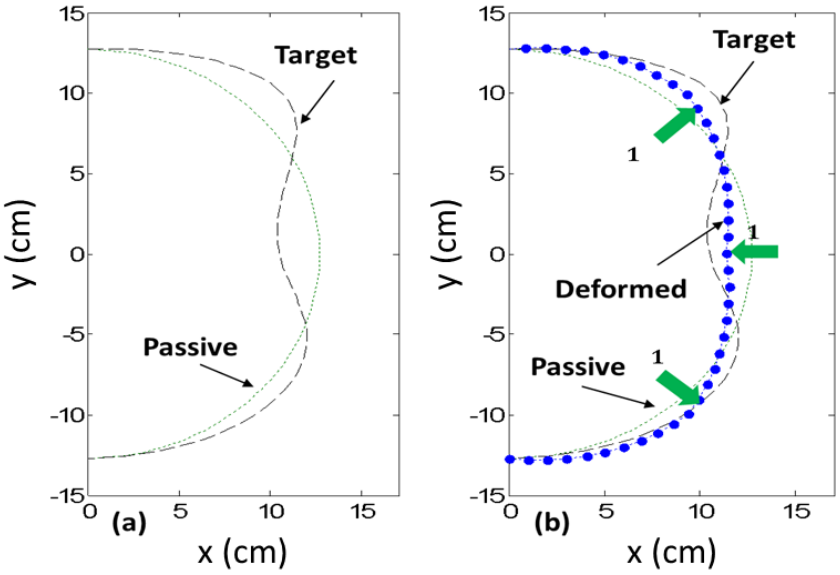

Figure 5-16: (a) Case study target shape; (b) body deformation without material softening (force values are normalized by the maximum allowable force)

Using three different performance indexes (i.e. shape error, softening rate and external work), we defined four objective functions. Each function includes the shape error term as the most desirable performance measure. Weighting factors for the error and external work terms are calculated based on the approach explained in the previous section. Since the modulus change energy is assumed proportional to the softened length, no scaling factor is assigned for that term.

The results of the morphing for different cases are illustrated in Figure 5-17 and listed in Table 5-3. For each case, the contributing terms in the corresponding overall performance index (J) have been highlighted. For the sake of comparison, the error between the passive unloaded and target shapes (J_{err}^{PT}) is evaluated and reported in the last column for each case. This value represents the maximum possible shape error.

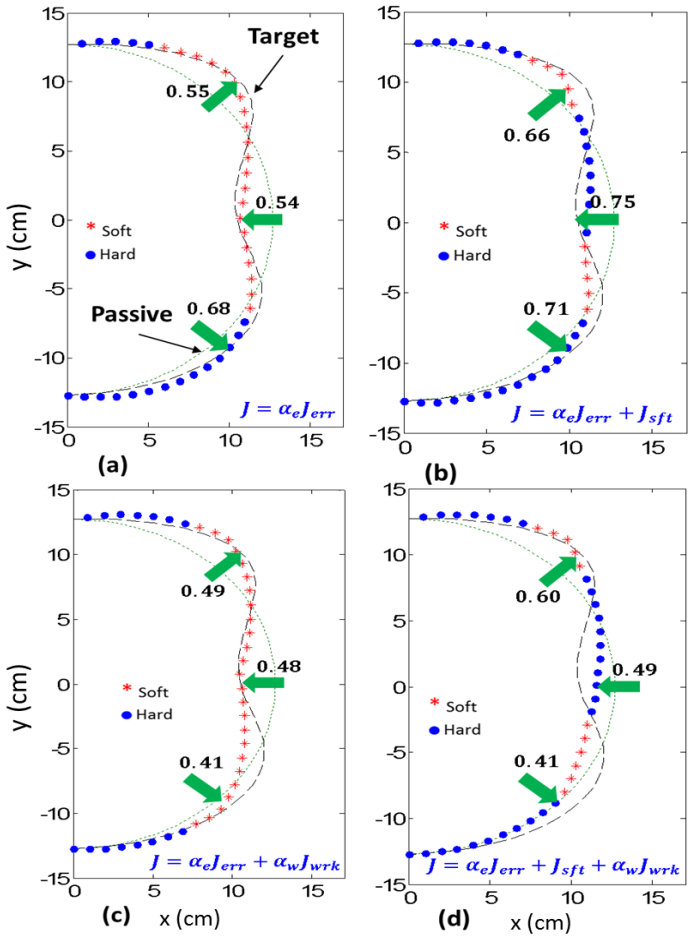

Figure 5-17: Optimal shapes using four different performance indexes

Table 5-3: Comparison of performance index terms in the above cases.
Shaded areas show the contributing terms used in the performance index (J). $\alpha_e J_{err}^{PT}$ is the error between passive and target shape and represents the maximum shape error ($\alpha_e = 0.22, \alpha_w = 0.002$).

Case	$\alpha_e J_{err}$	$\alpha_w J_{wrk}$	J_{sft}	J	$\alpha_e J_{err}^{PT}$
No morph	0.13	0.63	0	0.13	0.54
a	0.08	0.55	0.48	0.08	0.54
b	0.12	0.53	0.20	0.32	0.54
c	0.16	0.48	0.61	0.64	0.54
d	0.29	0.32	0.22	0.83	0.54

The initial row in the above table pertains to the case with no stiffness change (previously shown in Figure 5-16). The larger error indicates an unintended resulted shape. In case *a*, the performance is measured only based on the shape error without penalizing for any large modulus change energy and external work and the solution algorithm has the freedom to choose the best set of forces and softening rates. As a result, the optimal shape has the least dissimilarity with the target. In case *b,* material transformation energy also matters. Therefore, compared to the first case, smaller length is softened which results in a less accurate shape. Notice that although the structure is stiffer than in the previous case, due to the smaller overall deformation the work energy term is slightly lower. In the next case (case *c*), the effort is to minimize the shape error as well as the external mechanical energy. One notices that a decrease of the external work is compromised with an increase in the shape error as well as the softening energy. In the fourth case (case *d*), all the performance indexes (shape difference, material transformation energy and external work) are included. It is notable that the morphed shape error is considerably increased. This is because, i) due to penalizing stiffness variation energy, the structure tends to be stiffer than the previous cases and ii) since the actuation work is also constrained in the objective, smaller amount of actuation is used to move the stiff structure.

Another point worth noting is that, by comparing the values of performance index in these three cases, one notices an increasing trend in the final performance value with introducing more terms in the final index, despite the fact that the ultimate goal is to minimize the overall measure. Two reasons to explain the increment are: i) new terms are added at each step; and ii) a decrease in the added terms is compromised with an increase in the other contributing terms. Finally, one can observe that, as the number of terms in the performance function increase, more constraints are imposed in order to reach a precise shape, whose performance term was part of all the

selected functions. It is very essential to recognize the most important performance parameters based on the operation condition, physical limits and available energy resources.

5.8 SEQUENTIAL MORPHING

It was assumed that throughout the oscillation, the cylinder would morph to different unique shapes to maximize the lift at each stage. One question would be whether a current deformed structure should change to the next one in a sequential manner *or* return to the initial shape before morphing to the next one; in other words, is shape morphing a path dependent phenomenon? The primary goal in the following sections is to investigate this question.

5.8.1 Simplified spring model

In order to explore and analyze the behavior of the actual structure in different morphing paths, we define a simplified analytical framework. The assumptions throughout the analysis are made to agree with those in the numerical solver.

Consider a mass and spring system shown in Figure 5-18. We call this the initial position (A). It is assumed that the spring's stiffness can switch between a higher (k_H) and a lower (k_L) value and it is initially at the higher value. The block is massless and force F is used for actuation. In order to cover different possible scenarios and without losing generality, we assume the force is discrete with dF increments and has a maximum limit of F_{max}; also the spring becomes plastic beyond an extended length of X_{max}. In this analysis, position vectors are represented by X measured from the unstretched origin.

We will study a three-stage morph problem: from the initial position A to an intermediate target position X_t^B and then to a final position X_t^C (where the *t* subscript designates target) shown in Figure 5-18. Both target positions are within the elastic range. Two paths are defined: sequential ($A \rightarrow B \rightarrow C$) and non-sequential ($A \rightarrow B \rightarrow A \rightarrow C$).

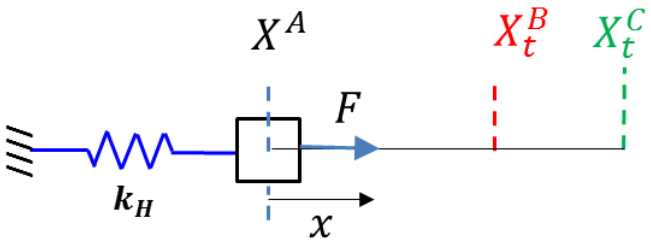

Figure 5-18: The mass and spring in initial position A with arbitrary target positions B and C

1) Morph from state A to B: We begin by keeping the spring in the hard state and increasing the force to arrive at the target. Two possible case scenarios are assumed:

Case 1: while the spring has high stiffness, the force is increased to F_{AB}^H to move the mass to the desired position (Figure 5-19). The notation F_{AB}^H represents the force used in the A-B path with high stiffness spring; also the B_H label on the left shows the stiffness used during the morph.

Case 2: In this case, with hard spring, the target is beyond the reach of the available force. Another way to reach to target is to switch the spring to the lower stiffness prior to loading and using a lower force F_{AB}^L to drive. We assume that a switching energy E_{sch} is used to change the stiffness (Figure 5-19). Since the spring has no stored energy at A, the substitution of a new spring is easy to realize. It is worth mentioning, our assumption is that for each transition, change of stiffness precedes the load application.

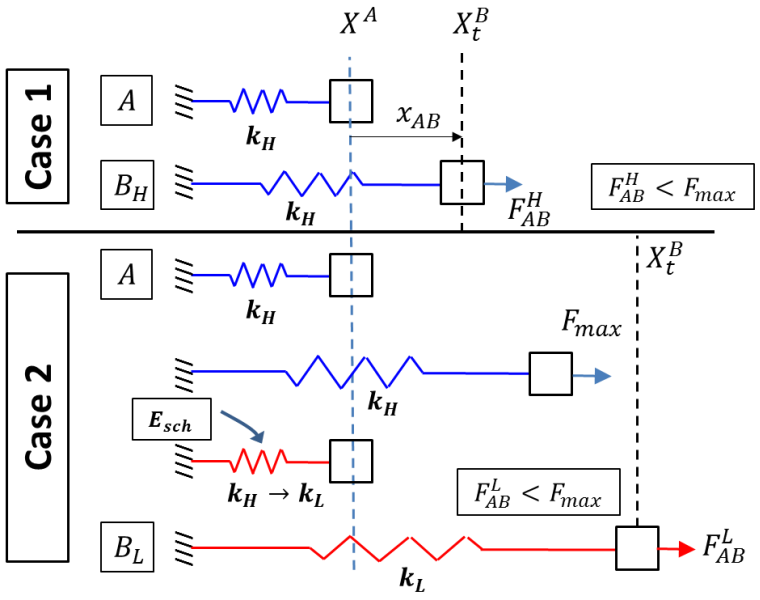

Figure 5-19: Morph from position A to target B with and without stiffness switching

For both cases, the displacement and energy stored in the spring at position B can be found from the following equations:

$$x_{AB} = \frac{F_{AB}^j}{k_j} \quad \left(j = L, H\ , x_{AB} < x_{max}, F_{AB}^j < F_{max}\right) \tag{5.4}$$

$$E_{AB} = \frac{1}{2} k_j x_{AB}^2 \quad j = L, H \tag{5.5}$$

2a) Morph from state B to C – Introducing preload To analyze the second transition, a few important assumptions need to be pointed out: 1) if needed to return to initial state A, the system should be unloaded and the exact previous position is achieved; 2) for transition to the next state (C), configuration B can be treated as an initial state, provided that a preload F_{AB} exists. This means that the force F_{AB} should be always taken into consideration during the second morph while F_{BC} is applied. This is a reasonable assumption because, the system should revert back to

B (and not A) after unloading from state C. In the next sections, this assumption is implemented in the FE solver to simulate multi-stage morph of an actual structure.

Now, starting from B with hard spring from previous step (Figure 5-20-top), let a small force δF move the mass by displacement δx (Figure 5-20, middle).

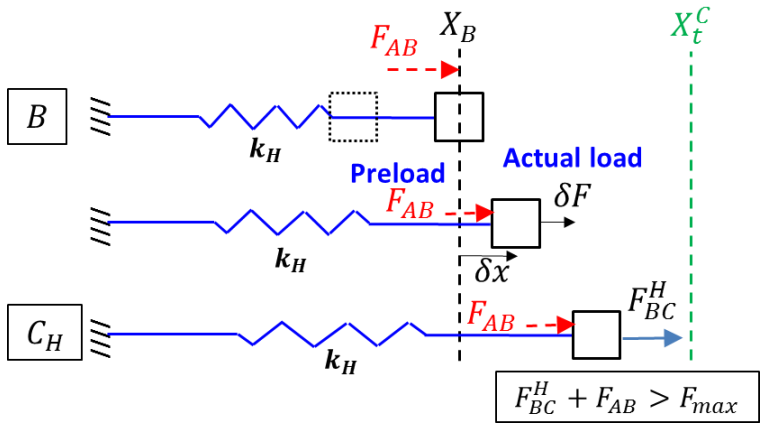

Figure 5-20: Morph from position B to C without stiffness switching

The equation of motion at equilibrium position is:

$$k_H(x_{AB} + \delta x) = F_{AB} + \delta F \tag{5.6}$$

It can be verified that by removing the additional load δF in this equation, the system returns to B. Replacing x_{AB} in Eq. (5.4), the differential displacement value would be:

$$\delta x = \delta F / k_L \tag{5.7}$$

Now the small force keeps increasing until the overall load reaches the force limit, while the mass has not yet arrived at the target C. Returning to B, we may now take advantage of the variable stiffness.

2b) switch stiffness from k_H to k_L

The spring stores a specific amount of energy while being stretched in the B position. Now, assume that the stiffness is decreased by δk while a small switching energy of e_{sch} is invested. As a result, a small displacement of δx is achieved because of the constant preload. One can tune the stiffness reduction to reach the desired position. For discrete values in this study, switching energy $\boldsymbol{E_{sch}}$ would change the stiffness. After decreasing the stiffness, if the target is still not reached, additional force F_{BC}^{L} will be required.

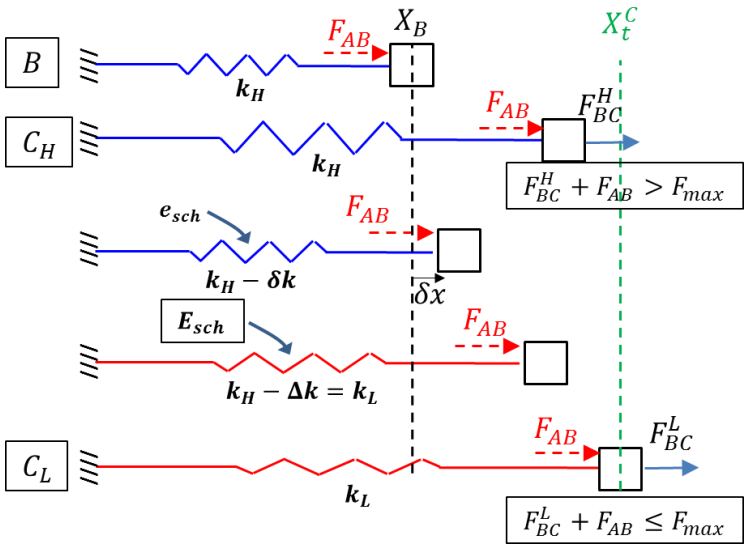

Figure 5-21: Switching from higher to lower stiffness in loaded configuration

2c) switch stiffness from k_L to k_H

Consider the case where the spring switched to lower stiffness in stage $A \rightarrow B$ to meet the position requirement and the mass was moved to B. Remember that we assumed the force is discrete with dF increments. Now, let the target C be between A and B at a position where the mass would surpass with the first decremented force (see Figure 5-22 - C_L).

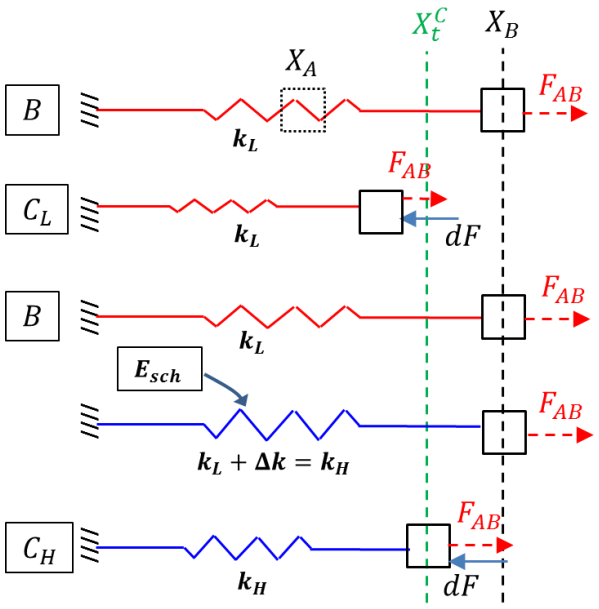

Figure 5-22: Switching from lower to higher stiffness in loaded configuration

An alternative way to reduce the displacement is to stiffen the spring. While at B, we assume that the stiffness increases by small increment of δk using $\boldsymbol{e_{sch}}$ energy**.** With constant preload, the slightly-harder stays at its position, but subsequent force changes will be affected by the new spring constant. . Similarly, by increasing the stiffness to k_H, the first force decrement would move the mass to C.

It is worth noting that the above scenarios were introduced to solely realize the stiffness change in loaded (stretched) position and will be later used to build and explain the FE models.

5.8.2 Spring model numerical example

A numerical example of a three-stage morph is explored. Consider the model with specifications in
Table **5-4**:

Table 5-4: Model specifications used in the example

Description	Parameter	Value	Unit
Target positions			
1st stage position	X^A	0	cm
2nd stage position	X_t^B	6	cm
3rd stage position	X_t^C	17	cm
Physical specifications			
Lower stiffness	k_L	1	N/cm
Higher stiffness	k_H	2	N/cm
Maximum force	F_{max}	20	N

The extended performance index includes position error (J_{err}), external work stored as energy in the spring (J_{wrk}) and stiffness switch energy index (J_{sch}). For each spring switching, a half unit (0.5) value index is assumed. Normalizing weights at each morph step are determined based on maximum values. An Excel spreadsheet was created to handle all the calculations.

The results are listed in Table 5-5 and Table 5-6. The rows are explained as follows: target positions are three stage positions in Table 5-4. The next row shows the required force to move the mass from one stage to the other in high (H) or low (L) spring stiffness. If the force needed was beyond the actuator's limit ($20\,N$), maximum force was assigned and the absolute error between the achieved and desired position was calculated (row 4). Normal errors are determined based on the maximum values in each stage transition. Work (spring energy) terms are spring energy based on the achieved displacement. Similarly, work terms were normalized by their maximum values at the end of each stage. The orange cells represent normal indexes. The stages are shown in consecutive columns. Four columns in the second stage include all possible cases based on the selected springs in the first stage. . In the presence of preload during $B \rightarrow C$, as the stiffness switched, the mass was first allowed to move by the existing load and if required, additional load was exerted. For the $B \rightarrow A$ stage, it was assumed that, the spring returns to A

with zero cost; therefore this stage is not listed. At the end of each stage, index terms were normalized by their maximum. The final index was calculated by accumulating minimum costs.

Table 5-5: Sequential morph evaluated with different indexes

Parameter	$A \rightarrow B$		$B \rightarrow C$			
			$A \rightarrow B$ (H)		$A \rightarrow B$ (L)	
	H	L	H	L	H	L
Target (stage) position	6	6	17	17	17	17
Required force	12	6	8	12	14	11
Achieved position	6	6	10	12	7	11
Absolute error	0	0	1	1	4	0
Normal error $(\alpha_e J_{err})$	0	0	0.25	0.25	1	0
Work (spring energy)	36	18	100	72	49	61
Normal work $(\alpha_w J_{wrk})$	1	0.5	1	0.72	0.49	0.61
Switch cost (J_{sch})	0	0.5	0	0.5	0.5	0
J_{e+s}	0	0.5	0.25	0.75	1.5	0
J_{w+s}	1	1	1	1.22	0.99	0.61
J_{all}	1	1	1.25	1.47	1.99	0.61

*$J_{e+s} = \alpha_e J_{err} + J_{sch}$ | $J_{w+s} = \alpha_w J_{wrk} + J_{sch}$ | $J_{all} = \alpha_e J_{err} + \alpha_w J_{wrk} + J_{sch}$
α_e: error normalizing weight = maximum error at each stage
α_w: work normalizing weight = maximum spring energy at each stage
**H and L represent high and low stiffness springs (k_H and k_L)

Table 5-6: Non-sequential morph evaluated with different indexes

Parameter	$A \rightarrow B$		$A \rightarrow C$			
			$A \rightarrow B$ (H)		$A \rightarrow B$ (L)	
	H**	L	H	L	H	L
Target (stage) position	6	6	17	17	17	17
Force	12	6	20	17	20	17
Achieved position	6	6	10	17	10	17
Absolute error	0	0	7	0	7	0
Normal error $(\alpha_e J_{err})$	0	0	1	0	1	0
Work (spring energy)	36	18	100	144.5	100	144.5
Normal work $(\alpha_w J_{wrk})$	1	0.5	0.69	1	0.69	1
Switch cost (J_{sch})	0	0.5	0	0.5	0.5	0
J_{e+s}	0	0.5	1	0.5	1.5	0
J_{w+s}	1	1	0.69	1.5	1.19	1
J_{all}	1	1	1.69	1.5	2.19	1

*$J_{e+s} = \alpha_e J_{err} + J_{sch}$ | $J_{w+s} = \alpha_w J_{wrk} + J_{sch}$ | $J_{all} = \alpha_e J_{err} + \alpha_w J_{wrk} + J_{sch}$
α_e: error normalizing weight = maximum error at each stage
α_w: work normalizing weight = maximum spring energy at each stage
**H and L represent high and low stiffness springs (k_H and k_L)

Table 5-7 summarizes the different performance measures in two paths for this example. In order to select the final spring sequence, we evaluated the final cumulative index for all the feasible scenarios and chose the springs corresponding to the minimum cost. For example, in sequential morph, if the major concern is external work, the selected performance column would be $J = J_{w+s}$ where it suggests using the softer spring for both stages. The letters *H* and *L* separated by dash (-) show the stiffness sequence for a path when a particular performance index is considered. For example, *H-H-L* in row 2, column 1 means the minimum error cost in a non-sequential path is achieved when the spring takes on *hard* stiffness in stage A-B followed by return stage B-A and then switch to the *soft* state for final stage A-C.

It is noted that the indexes are distinct in each paths. For any selected index, a sequential path results in lower values and is thus the preferred route of morphing. Also, it is notable that the stiffness sequence depends on the selected objective.

Table 5-7: Comparison of different performance measures in two paths (variable force)

Path	Performance index		
	J_{e+s}	J_{w+s}	J_{all}
SEQUENTIAL $A-B-C$	$H-H$	$L-L$	$L-L$
	0.25	**1.61**	**1.61**
NON-SEQUENTIAL $A-B-A-C$	$H-H-L$	$H-H-H$	$L-L-L$
	0.5	**1.69**	**2**
J_{e+s}: error+switch cost J_{w+s}: work+switch cost J_{all}: error+work+switch cost			

5.8.3 Sequential morph in the structure

In this section, multi-step morphing of the curved beam introduced in previous chapters will be investigated. For simplicity, we choose only one actuator at 135°. The force is assumed to be *constant* ($F = 0.5\,F_{max}$) for all the simulations, where F_{max} is the maximum force before the structure yields as was calculated in section 5.5.1. Figure 5-23 illustrates the initial and subsequent target shapes. The target shapes were arbitrarily chosen within the elastic deformation range and were created as B-spline curves using PTC® Creo Parametric and then converted to Cartesian points.

To evaluate the performance at each step, three indexes are studied: 1) weighted shape error ($\alpha_e J_{err}$), where error weight α_e at each step is found with respect to the largest error that is between the maximum loaded soft beam and the target; 2) weighted external work ($\alpha_w J_{wrk}$), where work is imported from FE results and its weight at each step is found from the maximum external work (determined in the soft structure case where largest allowed deformations are produced); and 3) modulus switch energy (J_{sch}), which is assumed to be proportional to the ratio of total softened (or hardened) segment lengths to entire beam length during a morph stage (e.g. 1/4 when a quarter of the beam is softened in first step and 1/8 when half of that soft segment is hardened back in next stage).

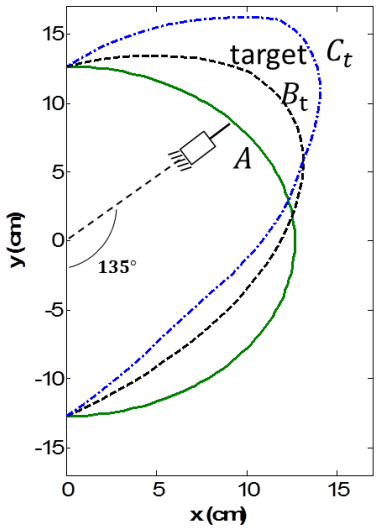

Figure 5-23: Initial (A) and subsequent (B and C) target shapes

So far, our algorithm could successfully handle the morph from unloaded initial to different target shapes. However, for a subsequent morph, as shown using the simplified spring model, the intermediate shape B should be *preloaded* in the model representation. To realize this in the simulation, once the beam is morphed into its optimal shape (B_m), the nodal displacement and stress fields as well as modulus distribution are stored and later used as initial conditions for the next stage (Figure 5-24). It should be noted that the force is constrained since part of the actuator's capacity has been used for prior deformation. The subsequent morph is calculated from this starting point. In this way, force(s) and resulting shape change applied during each morphing stage can be tabulated separately. The morph optimization subroutine used for previous chapters was extended to fulfill this operation.

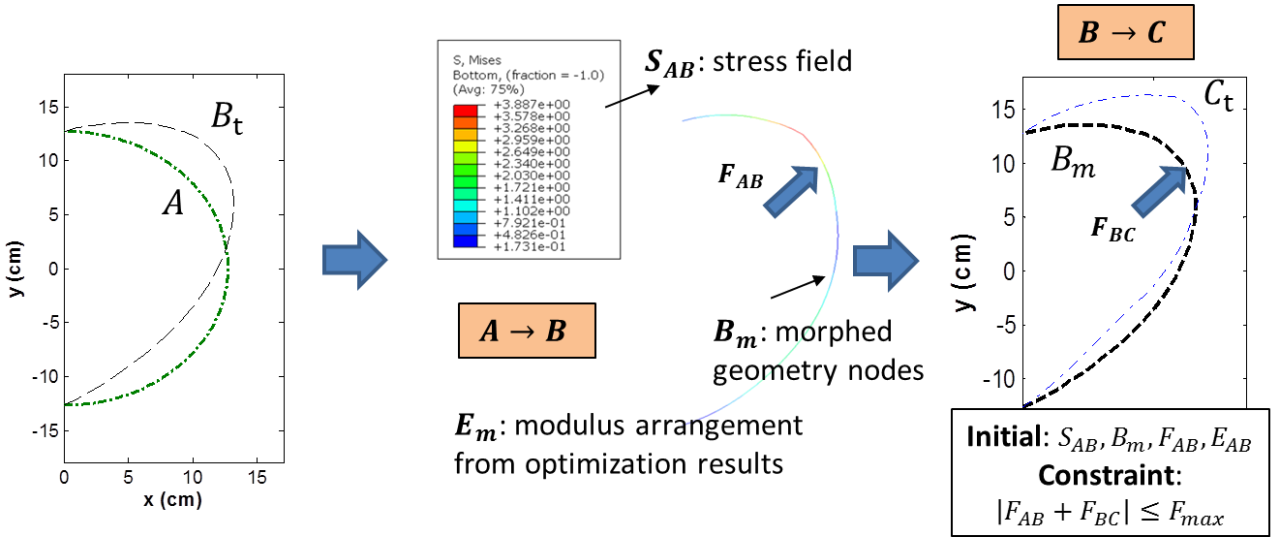

Figure 5-24: Numerical simulation of preloading in intermediate morphed shape

To simulate the unloading phase, since the previous stage (A) had no pre-stress, we used the nodal position of initial shape A with modulus arrangement in shape B to build the unloaded structure. This is an effort to avoid double modulus switching in the next step ($A \rightarrow C$). For higher number of morph stages, in order to unload form one stage to another, it is recommended to use the previously stored morph results for the target stage as initial conditions.

1) Sequential morph

Figure 5-25 shows the sequential morph and corresponding performance indexes (where the optimal morphed case is determined based on the respective performance index). All the arrows represent the constant fixed force. Dashed arrows represent preload from the previous stage. This means that the force never changes values in these cases, and the C shape is obtained only by decreasing the stiffness in certain regions. In all of the plots, initial and target shapes are shown in thin and thick lines. In order to highlight the effect of modulus variation in shape change, the shapes achieved by using just the hard case are also shown in the first column. Four cases are defined and designated by circled numbers below each column. If positional error is used as the

only optimization criterion, accurate shapes in both steps are achieved. When the strain energy is also penalized, because of the displacement constraint, more deviation from the target is observed. In the case of extended performance (error, energy and modulus switch), minimum stiffness alteration is noticed for each shape transition.

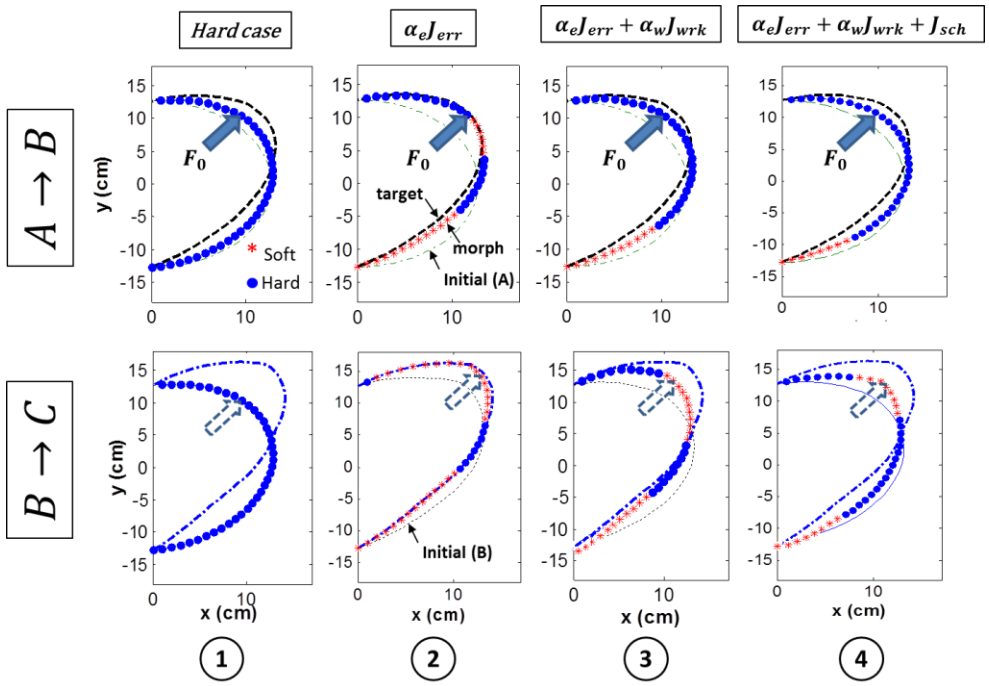

Figure 5-25: Sequential morphing in structure using different performance indexes. All solid arrows show constant force ($F_0 = 0.5F_{max}$) and dashed arrow show preload from *AB* stage

The results of morphing with different performance measures are tabulated in Table 5-8. For each case (defined above), different performance measures in both stages of the path are listed and those used to evaluate the total performance index (J_{tot}) are highlighted in color. For the hard case, all terms were used in the total performance index. As observed in the plots, while the work and modulus switch cost decrease from case 1 to 2 and 3, the position error enlarges. The increasing trend in the cumulative index is due to a) increased number of terms; and b) increased values of errors in subsequent cases.

Table 5-8: Numerical results for sequential morph in the structure

Case	Path	$\alpha_e J_{err}$	$\alpha_w J_{wrk}$	J_{sch}	J^{*}_{tot}	J^{**}_{cum}
1	AB	0.41	0.25	0	0.66	1.66
	BC	1	0	0	1	
2	AB	0.17	0.49	0.42	0.17	0.29
	BC	0.12	0.47	0.23	0.12	
3	AB	0.29	0.35	0.25	0.64	1.23
	BC	0.34	0.25	0.38	0.59	
4	AB	0.33	0.32	0.17	0.82	1.63
	BC	0.37	0.22	0.22	0.81	

$^{*}J_{tot}$: total weighted index (sum of highlighted cells)
$^{**}J_{cum}$: cumulative index of entire morph

2) Non-Sequential morph

Figure 5-26 shows the non-sequential morph and corresponding performance indexes. It is worth reminding that step $B \rightarrow A$ was created by using nodal geometry of shape A and conserving modulus properties of shape B. Notice that for each objective, the modulus distribution is distinct and different from the sequential path.

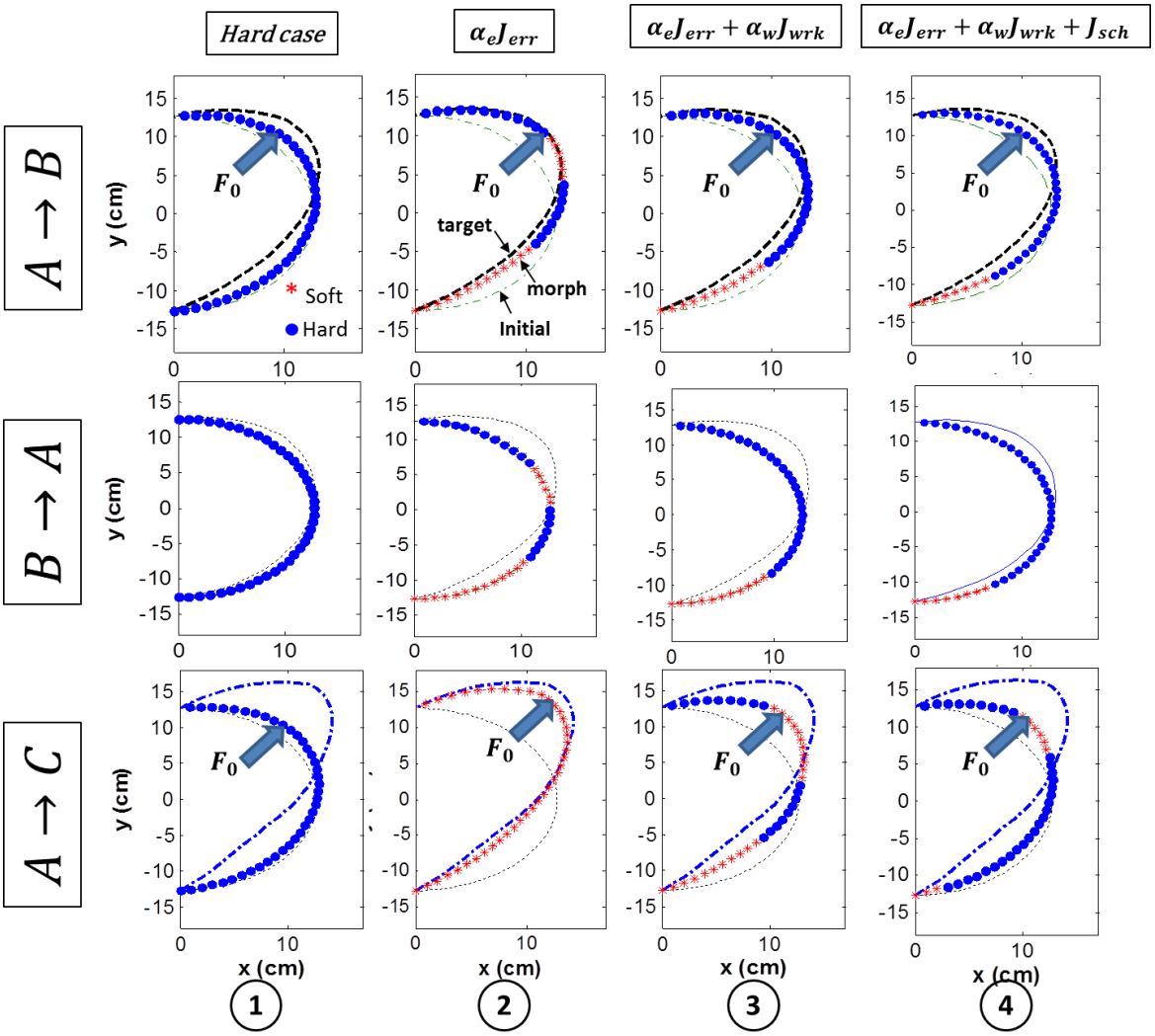

Figure 5-26: Non-sequential morph in structure using different performance indexes all arrows show constant force ($F_0 = 0.5F_{max}$)

Similarly, the results are presented in Table 5-9. Notice the zero index values in path $B \rightarrow A$ are due to the conservation of energy and error assumption during unloading.

Table 5-9: Numerical results for non-sequential morph in the structure

Case	Path	$\alpha_e J_{err}$	$\alpha_w J_{wrk}$	J_{sch}	J^{*}_{tot}	J^{**}_{cum}
1	AB	0.38	0.25	0	0.63	1.74
	BA	0	0	0	0	
	AC	0.86	0.25	0	1.11	
2	AB	0.17	0.49	0.42	0.17	0.37
	BA	0	0	0	0	
	AC	0.20	1.00	0.58	0.20	
3	AB	0.29	0.35	0.25	0.64	1.63
	BA	0	0	0	0	
	AC	0.48	0.51	0.26	0.99	
4	AB	0.33	0.32	0.17	0.82	2.11
	BA	0	0	0	0	
	AC	0.52	0.48	0.29	1.29	

$^{*}J_{tot}$: total weighted index (sum of highlighted cells)
$^{**}J_{cum}$: cumulative index of entire morph

Table 5-10 compares the two paths for this structure and its particular loading condition. With any measure criterion, the cost of reaching subsequent shapes is different for the two paths.

Table 5-10: Comparison of performance indexes in sequential and non-sequential paths

Path	Case 1	Case 2	Case 3	Case 4
Sequential	1.66	0.29	1.23	1.63
Non-sequential	1.74	0.37	1.63	2.11

It is important to point out that if the force were allowed to change, we might have reached a closer shape by simply increasing the force in stage $A \rightarrow B$; however this should be always investigated. An example is shown in Figure 5-27; consider two cases in $B \rightarrow C$ morph with error index: 1) keep the force fixed (F_0) and allow preload and modulus variation to morph the

second stage ; 2) let the force in stage $A \rightarrow B$ change to its limit without allowing for modulus change. For this example, larger shape error in case 2 highlights the need for stiffness variation.

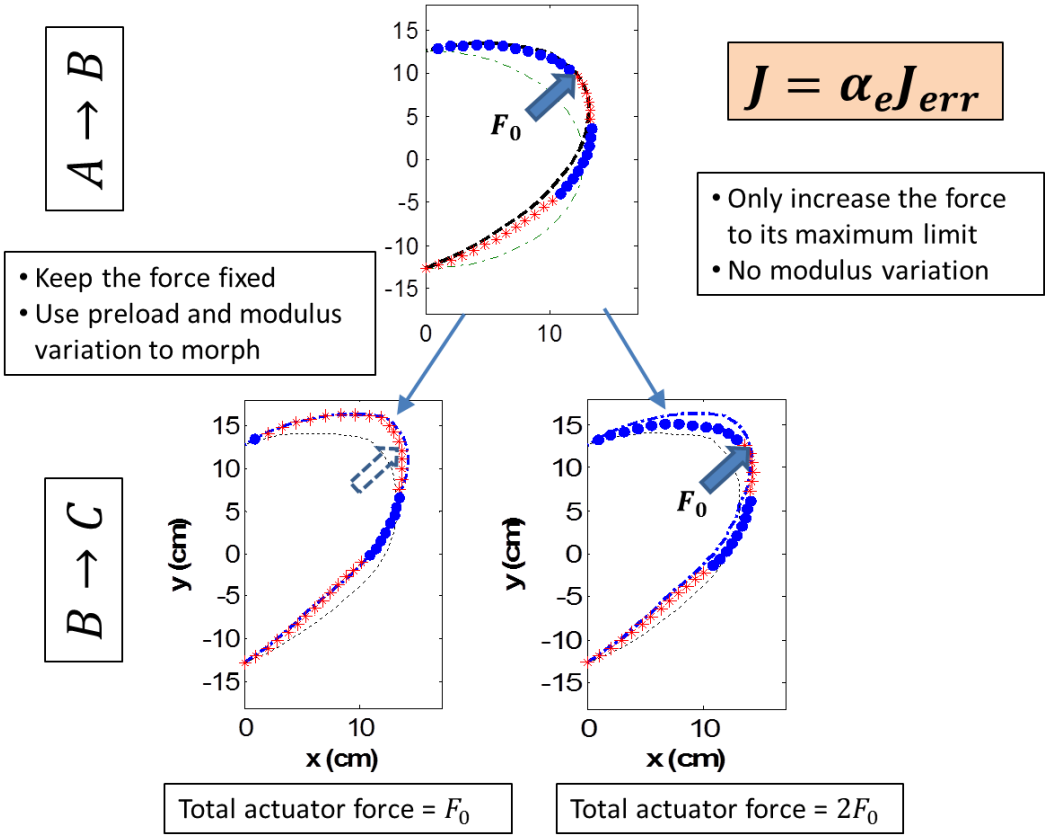

Figure 5-27: Comparing two morph scenarios in the second stage of sequential path

5.8.4 Summary and conclusion

In this section, the sequential morphing problem was explored through numerical examples on a simple spring-mass and on the more complex beam structure. For each stage in the path, normal error and external work were quantified in terms of the structure's stiffness and actuation force. For a more realistic morph, a stiffness switching cost was also taken into account. A single spring example was provided to illustrate how spring changes are implemented in a sequential morph scenario, and how optimal spring morph sequences are calculated. For a more complex

structure morph, the algorithms described in earlier chapters of this dissertation were improved to simulate the preload and unload scenarios used in the single spring, but extended for a continuous-stiffness structure.

For the single-spring case, the spring's optimal morph sequences are different and the sequential path results in smaller index. Moreover, for each index, selected springs over stages of the morph are distinct.

For the structure, a single constant actuation force ($F = 0.5F_{max}$) was used. The performance values over two paths were found to be different and the stiffness distribution pattern in each path is distinct. The sequential morph results in smaller performance values. Since the force is constant over the stages, morphing from one stage to another is achieved by redistribution of more soft segments. In the case of variable force, in order to avoid structural instability for each stage, a maximum strain criterion can be included in the performance evaluation subroutine.

6.0 CONCLUSIONS AND SUGGESTIONS FOR FUTURE WORK

Although the simulations were based on single (fixed and constant) force, our optimization algorithms are flexible and can be modified to handle more complex loading conditions (e.g. variable loads or multiple actuators). The dependence of performance index to the path proves that sequential morphing is not a trivial problem. In this study, we have developed the framework to analyze the sequential morph for any selected structure. Given the boundary conditions, actuators' position, and modulus variation characteristics, our algorithms can numerically simulate the morph in different steps. Using these tools, one can evaluate the cost of reaching subsequent shapes at a chosen path.

This work has laid the foundation for sequential morphing of complex structures. As future works, there are major questions that need to be investigated:

1) To achieve a sequence of shapes, is one path always better than others?

2) If there is a better path, how can one determine it?

3) How would the costs compare in the case of multi-stage (i.e. three or more stages) sequential morph?

APPENDIX A

GENETIC ALGORITHM

Genetic algorithms are different from normal search methods in the following ways:

- GA searches within a population of points, not a single point.
- GA uses probabilistic transition rules, not deterministic transition rules.

GA repeatedly alters a population of individual solutions. This algorithm, at each step, randomly chooses individuals from the current population to be parents who will produce children for the next generation. The population *evolves* toward an optimal solution over successive generations. GA is a robust optimization technique that can be used for a variety of optimization problems not well suited for standard optimization algorithms, e.g. problems with discontinuous, non-convex, highly nonlinear or stochastic objective functions.

There are two main differences between GA and a derivative-based optimization algorithm:

(a) Classical algorithms generate a single point in each iteration and the sequence of points approach an optimal solution; while GA produces a population of points in each step and the best point in one population reaches the optimal solution.

(b) Classical algorithms determine the next point in the sequence by deterministic computations, whereas GA chooses the next population based on computation using random number generators.

Featured GA terminology

- *Fitness function*: this is the function to be optimized, that is referred to as *objective function* in classical optimization algorithms.
- *Individual* (also known as *genome*): any point to which the fitness function is applied. The value of the fitness function for each individual is known as its *score*.
- *Population* and *Generation*: A *population* is an array of individuals. At each step, GA performs some computations on the current population to produce a successive population, which is called a new *generation.*
- *Diversity*: the average distance between individuals of a population is called diversity. A high-diversity population is one with large average distance. Diversity is an important factor in GA since it determines the region of space used for search algorithm.
- *Parents* and *Children*: *parents* are certain individuals, selected by GA, to create individuals in the next generation, known as *children*. Individuals with better *fitness values* are more likely to be chosen as parents.

The GA exploits three primary rules to create the next generation from the current population:

- *Selection*: selects the individuals (known as *parents*), who contribute to the population at the next generation.
- *Crossover*: combine two parents to form children for the next generation (see Figure A-1).
- *Mutation*: applies random changes to individual parents to form next generation's offspring.

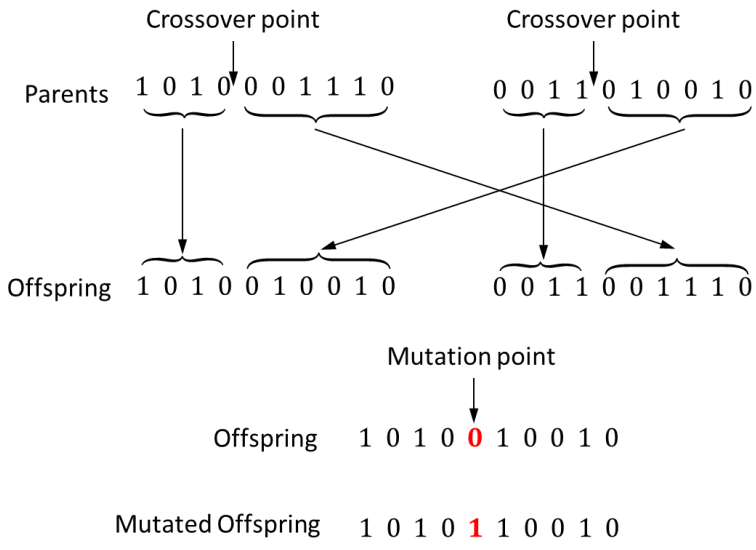

Figure A-1: Crossover and mutation to produce off-springs

GA algorithm outline

The GA algorithm's function can be described based on the following outline (R2010).

1) A random initial population is created.
2) The algorithm uses the current individuals to create the next population by performing the following steps:
    a) Each member of the current population is scored by its fitness value.
    b) Raw fitness values are scaled onto a more usable range.
    c) Parents are selected based on their fitness.
    d) Individuals with the best fitness value are marked as *elite children* and automatically survive to the next generation.
    e) Children are produced from the parents, either by making random changes (resulted from a Gaussian distribution) to a single parent (*mutation*), or by combining a pair of parents (*crossover*).
    f) The next generation is formed by replacing the current population with the children.

3) The algorithm stops once the population converges or one of the stopping criteria is met. The convergence is the progression towards increasing uniformity. An individual is converged when 95% of the population shares the same value. Stopping criteria may include number of generations, time limit, fitness limit or a tolerance on weighted average changes (Jong, 1990). A flowchart of this outline has been presented in Figure A-2.

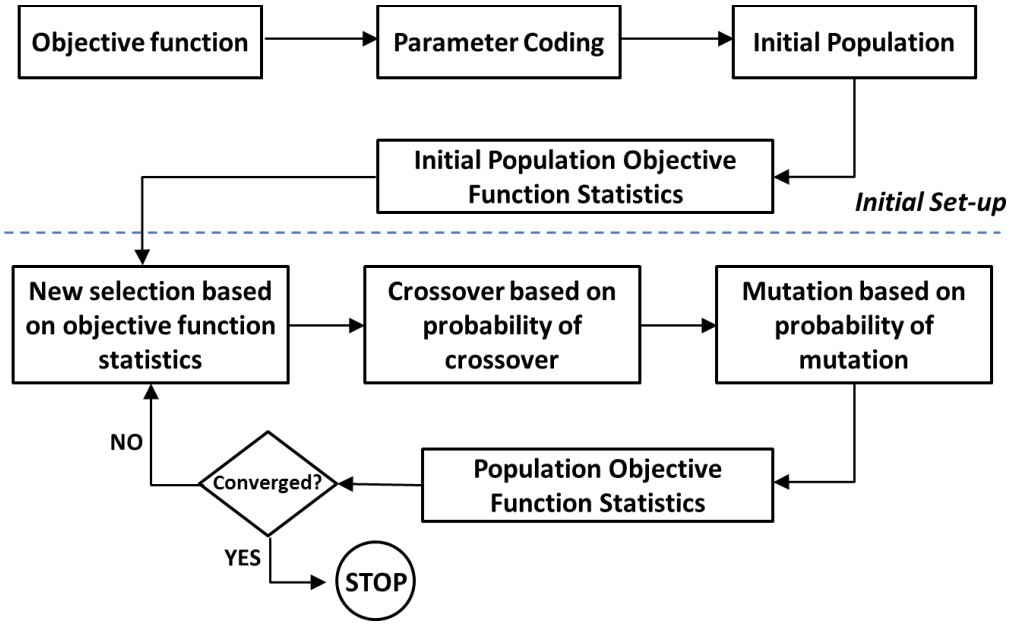

Figure A-2: GA algorithm flowchart

GA Implementation in MATLAB®

MATLAB® offers an optimization toolbox which provides widely used algorithms for standard and large-scale optimization. These algorithms solve constrained and unconstrained continuous and discrete problems. The toolbox has an interactive tool for defining and solving optimization problems and monitoring solution progress. The optimization software includes functions for linear, quadratic and integer programming, nonlinear optimization and multiobjective optimization. The embedded GA solver lets you specify the following options:

Population size: the number of individuals in each generation.

Elite count: number of individuals that are guaranteed to survive in the next generation. *Crossover fraction*: This fraction, along with a random weighted average of the parents, controls the intermediate crossover children: i.e. $Child_1 = Par_1 + rand * frac * (Par_2 - Par_1)$.

Scaling function: this function converts the raw fitness scores to values in a range suitable for the selection function. The most common function is *rank*, which scales the raw scores based on the rank of each individual, rather than its score. The rank of the fittest individual is 1, the next fittest is 2 and so on.

Hybrid function: Depending on the constraint conditions, one can specify another minimization function that runs after the genetic algorithm terminates. The choices are *fminsearch* and *fminunc* (for unconstrained nonlinear minimization) and *fmincon* (for constrained nonlinear minimization).

Stopping criteria: are the criteria that determine what causes the algorithm to terminate. The common criteria are listed as:

- *Generations*: defines the maximum number of iterations.
- *Fitness limit*: the algorithm stops if the best fitness value is less or equal to this value.
- *Time limit*: determines the maximum time (in *seconds*) that GA runs before it stops.

Stall generations: If the weighted average change in the objective function over stall generations is less than *function tolerance*, the algorithm stops.

Figure A-3 is an example GA operation in MATLAB. Best fitness is the minimum function, whereas the mean fitness is the fitness of each genotype (individual) multiplied by its frequency. Stopping criteria is chosen between maximum allowable number of iterations (here 100 generations) and stall generations (80 generations), whichever is met first.

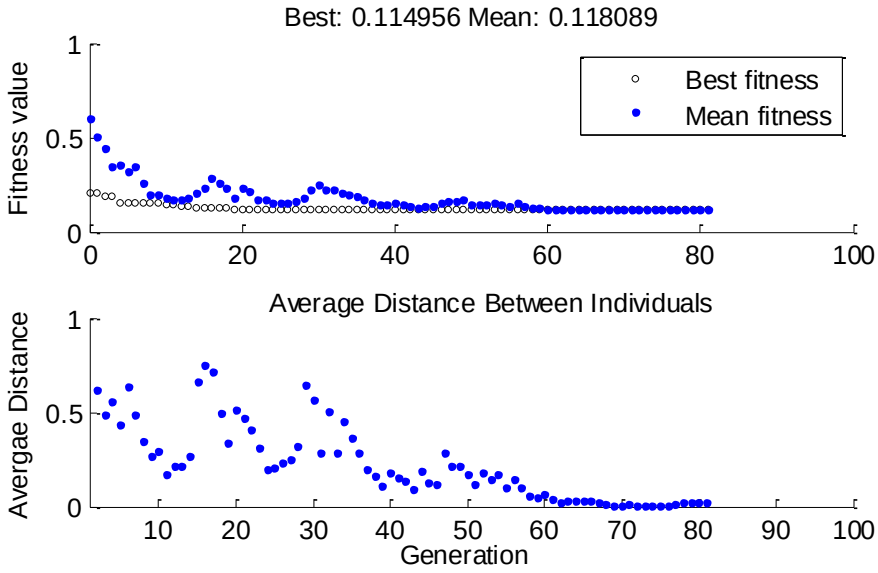

Figure A-3: optimization over consecutive generations

APPENDIX B

INTRODUCING B-SPLINES

The two most common methods of representing curves and surfaces in geometric modeling are implicit equations and parametric functions. The implicit equation of a curve (in the form $f(x, y) = 0$), describes the implicit relationship between the x and y coordinates of the points on the curve. An example is the circle of unit radius centered at the origin that can be represented by the equation $f(x, y) = x^2 + y^2 - 1 = 0$.

In parametric form, each of the coordinates of a point on the curve is separately represented as an explicit function of an independent parameter

$$C(u) = \big(x(u), y(u)\big) \qquad a \leq u \leq b \tag{B.1}$$

Where, $C(u)$ is a vector-valued function of the independent variable u. The interval $[a, b]$ is usually normalized to $[0, 1]$.

It is likely that target shapes can be most readily represented as geometric *B-splines* or curves that are initially created in a computer aided drawing (CAD) program. B-splines were first proposed by (Gordon and Riesenfeld, 1974). A *p*th-degree B-spline curve is defined by

$$C(u) = \sum_{i=0}^{n} N_{i,p}(u)\boldsymbol{P}_i \qquad a \leq u \leq b \tag{B.2}$$

Where u is called a *knot*, $\{\boldsymbol{P}_i\}$ are the *control points* ($n+1$ points), and the $\{N_{i,p}(u)\}$ are the *p*th-degree B-spline basis functions defined on the nonuniform *knot vector U* (composed of $m+1$ knots):

$$U = \{\underbrace{0, \dots, 0}_{p+1}, u_{p+1}, \dots, u_{m-p-1}, \underbrace{1, \dots, 1}_{p+1}\} \tag{B.3}$$

The degree, p, the number of control points, $n+1$, and number of knots, $m+1$, are related by:

$$m = n + p + 1 \tag{B.4}$$

The basis functions $\{N_{i,p}(u)\}$ are defined as:

$$\begin{aligned} N_{i,0}(u) &= \begin{cases} 1 & u_i \le u < u_{i+1} \\ 0 & \text{otherwise} \end{cases} \\ N_{i,p}(u) &= \frac{u - u_i}{u_{i+p} - u_i} N_{i,p-1}(u) + \frac{u_{i+p+1} - u}{u_{i+p+1} - u_{i+1}} N_{i+1,p-1}(u) \end{aligned} \tag{B.5}$$

Notice that for $p > 0$, $N_{i,p}(u)$ is a linear combination of two $(p-1)$-degree basis functions. As an example, for $p = 3, i = 4, U = \{0,0,0,1,2,3,4,4,5,5,5\}$, the recursive definition of basis functions could be described by:

$$N_{4,3}(u) = \frac{u-2}{2} N_{4,2}(u) + \frac{5-u}{2} N_{5,2}(u) \tag{B.6}$$

This function has been shown in Figure B-1.

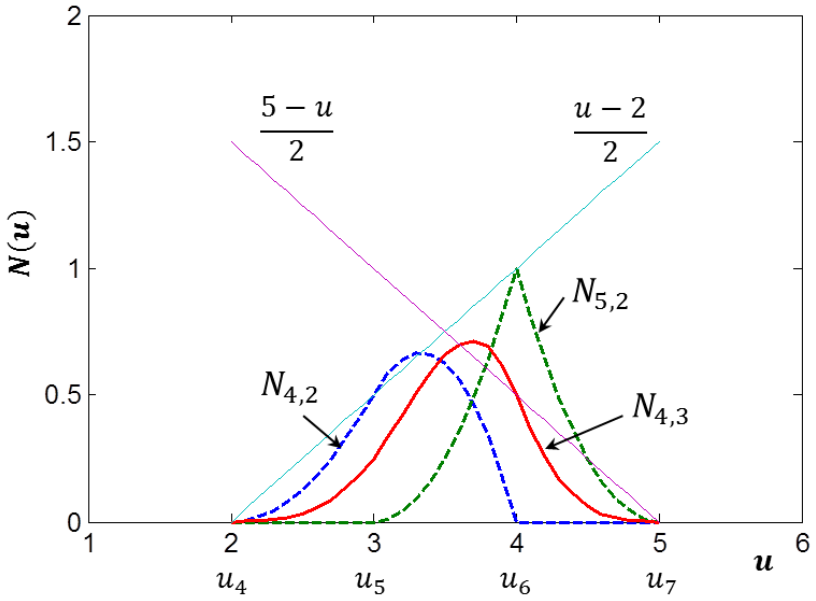

Figure B-1: Recursive definition of cubic B-spline basis functions

The polygon formed by the control points $\{\boldsymbol{P}_i\}$ is known as *control polygon*. The control polygon represents a piecewise linear approximation to the curve that could be improved by knot insertion or degree elevation. The lower the degree, the closer a B-spline curve follows its control polygon, because there are fewer control points that contribute to the computation of $C(u_i)$ for any given u_i. For $p = 1$, every point $C(u_i)$ is a linear interpolation between two control points and the curve is essentially the control polygon. Figure B-2 illustrates a quadratic curve, its control polygon and corresponding basis functions. Sections of the curve designated by dashed windows are resulted from their corresponding basis functions.

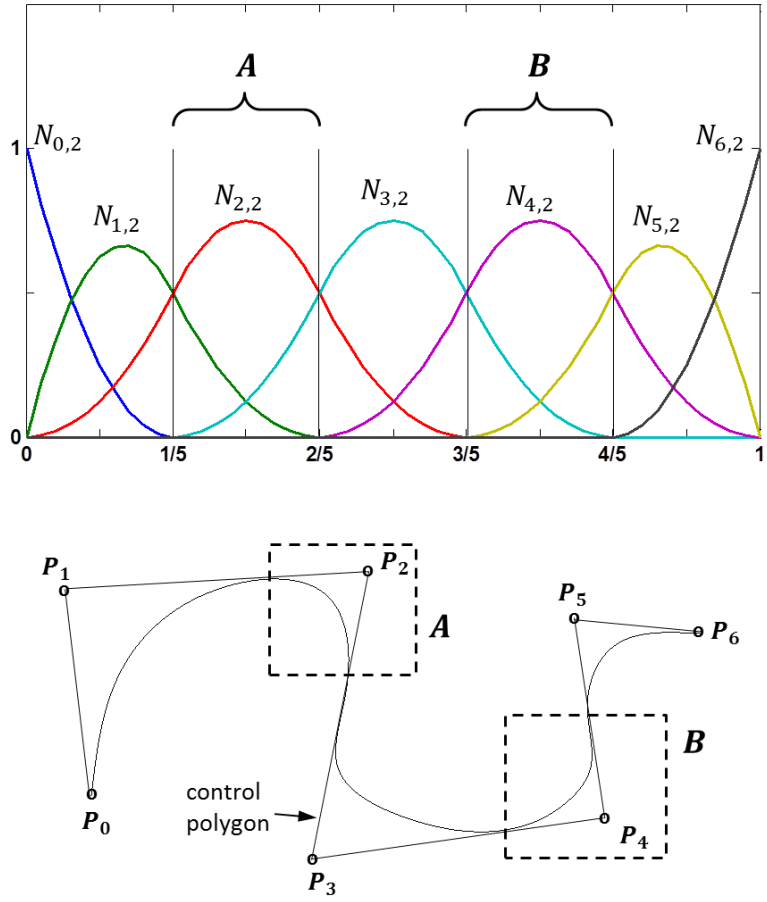

Figure B-2: (top) quadratic basis functions; (b) a quadratic curve using the top basis functions and its control polygon ; $U = \{0, 0, 0, 1/5, 2/5, 3/5, 4/5, , 1, 1, 1\}$

Computation algorithms

From curve properties in CAD, one can only extract the control points (n) and the degree of the basis functions (p). However, in order to analyze and find the morphing parameters, it is essential to convert the B-spline curve into an explicit form with discrete coordinate points, i.e. $C(u) = \big(x(u), y(u)\big)$. Here, computational algorithms to carry out the conversion are developed.

Let U be a knot vector of the form $U = \{u_0, \dots, u_m\}$ in Eq. (B.3). We are interested in the basis functions of degree p. let u be fixed and $u \in [u_i, u_{i+1})$. Algorithms are needed to compute:

- The knot span index, i.

- $N_{i-p,p}(u), \dots, N_{i,p}(u)$ (Eq. B.5)
- A single basis function, $N_{j,p}(u)$, where $0 \leq j \leq m - p - 1$.

To find the knot span index, an integer function is used. This algorithm uses a binary search method to identify the corresponding knot index. A subtle problem in the evaluation of the basis function relates to the special cases $u = u_m$ or $u = 0$. In this case, the span index is set to $n = m - p - 1$.

Having found the span index, in the second algorithm we wish to compute the basis functions. Assuming u is in the i-th span, computation of the nonzero functions results in the following inverted triangular scheme:

$$\begin{array}{ccccc} & & & & N_{i-p,p} \\ & & N_{i-1,1} & & \\ N_{i,0} & & \cdots & & \vdots \\ & & N_{i,1} & & \\ & & & & N_{i,p} \end{array}$$

Coordinate Matching algorithm: The coordinates of the converted spline depend on the location of the control points and thus, their placement along the beam is different from the equally distributed numerical mesh. It is necessary to match these coordinate beforehand. A matching algorithm was developed to perform this task: consider part of a spline curve shown in Figure B-3. Let x_{sp}^{i} and x_{sp}^{i+1} be a consecutive converted pair of spline points located on both sides of the j-th uniform mesh point x_m^j . It is desired to approximate y_m^j in terms of the spline and mesh coordinates.

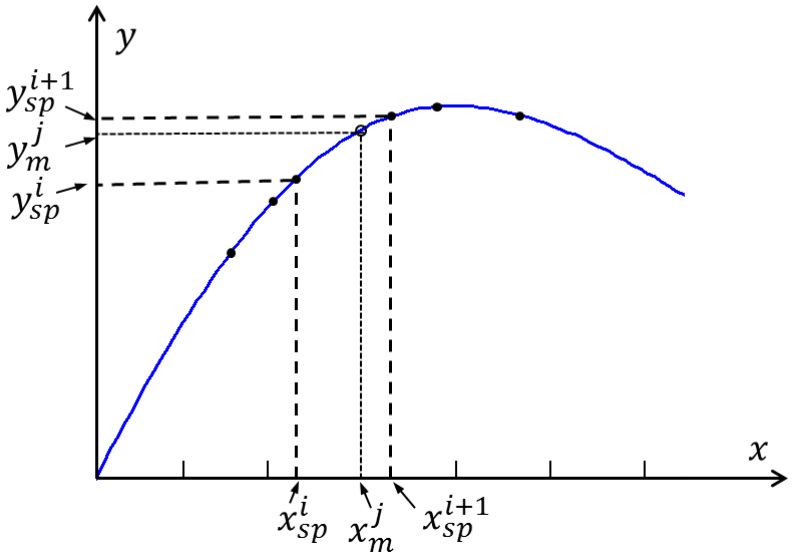

Figure B-3: Matching spline and mesh coordinates

A normalized distance weighting function is defined based on the distance of each spline point to its adjacent mesh point. This implies the closer points to the actual mesh point will gain larger weights.

$$w_R = \frac{(x_m^j - x_{sp}^i)}{(x_{sp}^{i+1} - x_m^j)} \qquad (B.6)$$

$$w_L = 1 - w_R$$

The approximate curve point is attained by assigning the corresponding weights:

$$y_m^j = w_L y_{sp}^i + w_R y_{sp}^{i+1} \qquad (B.7)$$

Numerical example

Figure B-4 shows a cubic B-spline curve drawn in AutoCAD® with its highlighted control polygon. Table B-1 shows the control points' data.

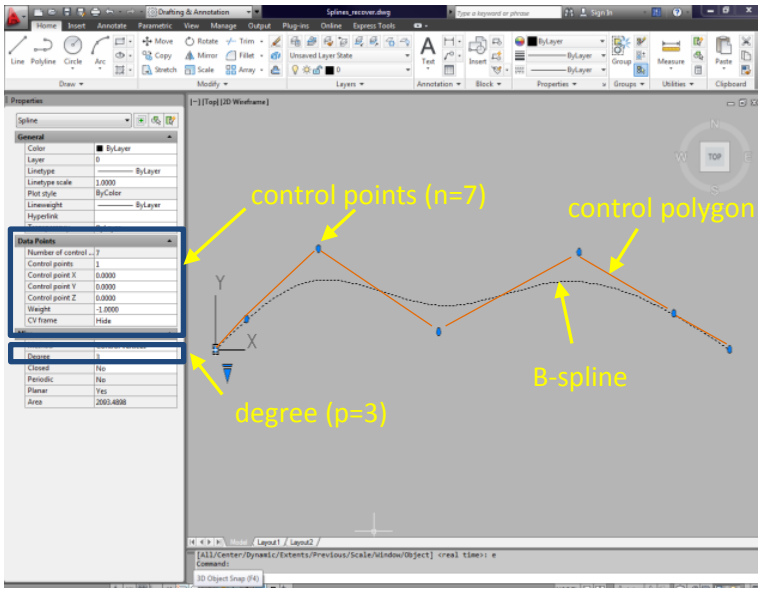

Figure B-4: A cubic B-spline
Control polygon and points are highlighted as properties are inquired

Table B-1: Control points of the cubic B-spline CAD curve

Control Points $\{\boldsymbol{P}_i\}$	X (mm)	Y (mm)
0	0	0
1	12.11	6.44
2	40	21.3
3	86.8	3.73
4	141.5	20.53
5	178.3	7.61
6	200	0

Given the information about the control points and the spline degree, MATLAB® routines are implemented and the B-spline coordinates are regenerated using *plot* tool (Figure B-5).

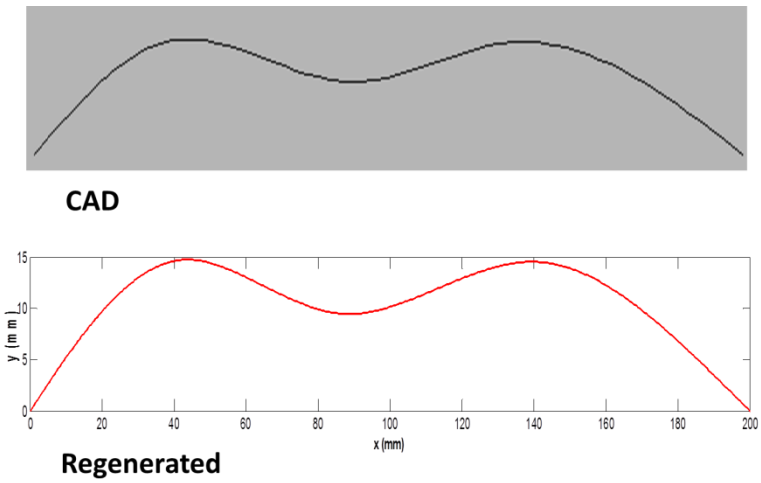

Figure B-5: Regenerated cubic spline using MATLAB routines

BIBLIOGRAPHY

(R2010) MATLAB. MA, USA: The Mathworks Inc.

Agrawal BN and Treanor KE. (1999) Shape control of a beam using piezoelectric actuators. *Smart Materials and Structures* 8: 729.

Ameri N, Livne E, Lowenberg MH, et al. (2008) Modelling Continuously Morphing Aircraft for Flight Control. *Aerospace*: 1-23.

Blondeau J, J. R and D. P. (2003) Design , development and testing of a morphing aspect ratio wing using an inflatable telescopic spar. *44th AIAA/ASME Structures, Structural Dynamics and Materials Conference.* Norfolk, VA.

Boyerinas BM, Clark WW, Weiland LM (2009) Design and Fabrication of a Variable Stiffness Link for Use in an Unmanned Air Vehicle. *ASME Conference Proceedings* 2009: 317-323.

Brughmans M, Goosense S, Toshiki T, et al. (2003) Morphing Technology Applied to Body Modelling. *Journal of the Society of Automotive Engineers of Japan* 57: 14-20.

Calkins FT, Mabe JH and Butler GW. (2006) *Boeing's Variable Geometry Chevron : morphing aerospace structures for jet noise reduction*, Bellingham, WA, ETATS-UNIS: Society of Photo-Optical Instrumentation Engineers.

Calvo-Marzal P, Delaney MP, Auletta JT, et al. (2011) Manipulating Mechanical Properties with Electricity: Electroplastic Elastomer Hydrogels. *ACS Macro Letters* 1: 204-208.

Chandrashekhara K and Varadarajan S. (1997) Adaptive Shape Control of Composite Beams with Piezoelectric Actuators. *Journal of Intelligent Material Systems and Structures* 8: 112-124.

Chaudhry Z and Rogers CA. (1991) Bending and Shape Control of Beams Using SMA Actuators. *Journal of Intelligent Material Systems and Structures* 2: 581-602.

Cho M and Kim S. (2005) Structural morphing using two-way shape memory effect of SMA. *International Journal of Solids and Structures* 42: 1759-1776.

Clark WW. (2000) Vibration Control with State-Switched Piezoelectric Materials. *Journal of Intelligent Material Systems and Structures* 11: 263-271.

Corr LR and Clark WW. (2002) Comparison of low-frequency piezoelectric switching shunt techniques for structural damping. *Smart Materials and Structures* 11: 370.

Cwikiel W, Stridbeck H, Tranberg KG, et al. (1993) Malignant esophageal strictures: treatment with a self-expanding nitinol stent. *Radiology* 187: 661-665.

Donthireddy P and Chandrashekhara K. (1996) Modeling and shape control of composite beams with embedded piezoelectric actuators. *Composite Structures* 35: 237-244.

Falcioni JG. (1992) Shape Memory Alloys. *Mechanical Engineering* 114.

Flangan J, Strutzenberg R, Myers R, et al. (2007) Development and Flight Testing of a Morphing Aircraft, the NextGen MFX-1. *Camera* April: 1-3.

Furuya H and Haftka RT. (1995) Placing actuators on space structures by genetic algorithms and effectiveness indices. *Structural optimization* 9: 69-75.

Gautschi G. (2002) *Piezoelectric sensorics: force, strain, pressure, acceleration and acoustic emission sensors, materials and amplifiers*: Springer.

Gordon WJ and Riesenfeld RF. (1974) B-spline curves and surfaces. *Computer Aided Geometric Design* 0167: 95.

Haftka RT. (1984) *Optimum placement of controls for static deformations of space structures,* Reston, VA, ETATS-UNIS: American Institute of Aeronautics and Astronautics.

Haftka RT and Adelman HM. (1985) Selection of actuator locations for static shape control of large space structures by heuristic integer programing. *Computers & Structures* 20: 575-582.

Jacob JD, Simpson A and Smith S. (2005) Design and Flight Testing of Inflatable Wings with Wing Warping. *Society of Automotive Engineers.*

Jong KD. (1990) Genetic-algorithm-based learning. *Machine learning*. Morgan Kaufmann Publishers Inc., 611-638.

Keihl MM, Bortolin RS, Sanders B, et al. (2005) Mechanical properties of shape memory polymers for morphing aircraft applications. *SPIE 5762.* San Diego, CA: SPIE.

Lazarus KB, Crawley EF and Bohlmann JD. (1991) *Static aeroelastic control using strain actuated adaptive structures,* London, ROYAUME-UNI: Sage Publications.

Lendlein A and Kelch S. (2002) Shape-Memory Polymers. *Angewandte Chemie International Edition* 41: 2034-2057.

Mabe JH, Calkins FT and R.T. R. (2007) *Full-scale Flight Tests of Aircraft Morphing Structures using SMA Actuators,* Bellingham, WA, ETATS-UNIS: Society of Photo-Optical Instrumentation Engineers.

McKnight G and Henry C. (2005) *Variable stiffness materials for reconfigurable surface applications,* Bellingham, WA: Society of Photo-Optical Instrumentation Engineers (SPIE).

Monkman GJ. (2000) Advances in shape memory polymer actuation. *Mechatronics* 10: 489-498.

Monroe JA, Cruz-Perez J, Yegin C, et al. (2012) Magnetic response of porous NiCoMnSn metamagnetic shape memory alloys fabricated using solid-state replication. *Scripta Materialia* 67: 116-119.

Morgan NB. (2004) Medical shape memory alloy applications—the market and its products. *Materials Science and Engineering: A* 378: 16-23.

Neal DA. (2006) Design, Development and Analysis of a Morphing Aircraft Model for Wind Tunnel Experimentation. *Mechanical Engineering.* Virginia Polytechnic Institute and State University.

Otsuka K and Wayman CM. (1999) *Shape Memory Materials*: Cambridge University Press.

Pastor C, Sanders B, Joo JJ, et al. (2006) Kinematically Designed Flexible Skins for Morphing Aircraft. *ASME Conference Proceedings* 2006: 89-95.

Perkins D, Reed JJ and Havens E. (April 2004) Morphing wing structures for loitering air vehicles. *45th AIAA/ASME/ASCE/AHS/ASC Structures, Structural Dynamics and Materials Conference.* Palm Springs, CA.

Rauscher SG. (2008a) Testing and Analysis of Shape-memory Polymers for Morphing Aircraft Skin Application. *Mechanical Engineering.* University of Pittsburgh.

Rauscher SG. (2008b) Testing and Analysis of Shape-memory Polymers for Morphing Aircraft Skin Application. *Mechanical Engineering.* Pittsburgh.

Reed JL, Hemmelgarn CD, Pelley BM, et al. (2005) *Adaptive wing structures,* Bellingham, WA, INTERNATIONAL: Society of Photo-Optical Instrumentation Engineers.

Timoshenko S. (1961) *Theory of elastic stability*: McGraw-Hill.

Vinograd I, Klin B, Brosh T, et al. (1994) A new intratracheal stent made from nitinol, an alloy with "shape memory effect". *The Journal of thoracic and cardiovascular surgery* 107: 1255-1261.